



Recent trends and advances in fundus image analysis: A review

Shahzaib Iqbal ^a, Tariq M. Khan ^{b,*}, Khuram Naveed ^{a,c}, Syed S. Naqvi ^a, Syed Junaid Nawaz ^a

^a Department of Electrical and Computer Engineering, COMSATS University Islamabad (CUI), Islamabad, Pakistan

^b School of Computer Science and Engineering, University of New South Wales, Sydney, NSW, Australia

^c Department of Electrical and Computer Engineering, Aarhus University, Aarhus, Denmark



ARTICLE INFO

Keywords:

Classification
Segmentation
Retinal fundus images
Eye diseases
Hypertensive retinopathy
Diabetic retinopathy

ABSTRACT

Automated retinal image analysis holds prime significance in the accurate diagnosis of various critical eye diseases that include diabetic retinopathy (DR), age-related macular degeneration (AMD), atherosclerosis, and glaucoma. Manual diagnosis of retinal diseases by ophthalmologists takes time, effort, and financial resources, and is prone to error, in comparison to computer-aided diagnosis systems. In this context, robust classification and segmentation of retinal images are primary operations that aid clinicians in the early screening of patients to ensure the prevention and/or treatment of these diseases. This paper conducts an extensive review of the state-of-the-art methods for the detection and segmentation of retinal image features. Existing notable techniques for the detection of retinal features are categorized into essential groups and compared in depth. Additionally, a summary of quantifiable performance measures for various important stages of retinal image analysis, such as image acquisition and preprocessing, is provided. Finally, the widely used in the literature datasets for analyzing retinal images are described and their significance is emphasized.

1. Introduction

The retina is a thin, transparent, and light-sensitive tissue located in the back of the eye that senses light and sends images to the brain. The retina contains millions of light-sensitive cells (rods and cones) and other optic nerves that receive, organize, and send visual information [1]. In the center of the retina is the macula, which provides sharp and focusing central vision. A healthy retina is essential and crucial for good vision. Retinal diseases cause damage to the retina that affects vision and may lead to blindness. Floaters, macular degeneration, diabetic retinopathy, hypertensive retinopathy, multiple sclerosis, retinal detachment, and retinitis pigmentosa are all examples of common retinal conditions [2]. Ophthalmologists need a high degree of attention and precision for an accurate diagnosis. A slight mistake during diagnosis may affect/corrupt the patient's sight and even cause blindness. Under massive workload, Diabetic Retinopathy (DR) ophthalmologists may miss out on some important details in the retinal image. Nevertheless, the retinal vessels are very thin and therefore are hard to see. It is even more difficult to see an obstruction in vessels.

In recent years, technological advancements have enabled the development of a wide range of diagnostic equipment, devices, and methods [3,4]. Sometimes doctors require visual analysis to diagnose certain diseases. This may be successful in some instances, but it is not always effective due to factors such as inexperience, fatigue, the variety of shapes and textures, and poor image quality. As a result,

computer-aided diagnosis (CAD) has emerged as an important tool for the detection and examination of various diseases. In the recent past, these techniques have been primarily based on deep learning or machine learning methods.

CAD facilitates ophthalmologists by helping in diagnosis and determines congestions occurring inside vessels. Fundus photography is used to detect retinal changes, inspect anomalies associated with diseases and monitor their progression [5,6]. This provides ophthalmologists with more information about the progression of eye illness and allowing early and accurate diagnosis of the eye. Diabetes is a disease that affects your body's ability to supply or use insulin. Uncontrolled diabetes sometimes affects the eyes or other parts of the body. DR is an eye disease that is a complication of diabetes. In DR, the formation of retinal blood vessels changes because of diabetes. There are two types of changes in retinal blood vessels [7]. In the first type, the blood vessel walls become narrow, and occlusion occurs between them. The narrowing of blood vessels causes changes in the retina. In the second type, the blood vessels become feeble and start leaking. The narrowing occurs on the cause of hypoxia or ischemia. Due to a decreased blood supply, tissues of the retina will receive less oxygen, leading to hypoxia or ischemia. Due to the lack of oxygen in internal tissue, it extracts a chemical substance called vasoformative. This substance leads to the growth of new blood vessels to prevent from loss of oxygen, which is

* Corresponding author.

E-mail address: tariq045@gmail.com (T.M. Khan).

dangerous. The new blood vessels are fragile, feeble, and are in form of bundles so they bleed. The bleeding creates clothes on the retina, which causes vision loss.

Digital retinal images are examined primarily for the diagnosis of different retinal diseases that are among the leading causes of blindness worldwide. Timely diagnosis of these diseases is crucial where the aid of computer-based tools can potentially play a vital role. Recent advancements in computational methods and frameworks (e.g., distributed computing, edge computing, quantum computing (QC), etc.) and data-driven intelligence provisions (e.g., Machine Learning (ML), Deep Learning (DL), etc.) have sparked hope for the development of a fully autonomous and robust disease detection system.

1.1. Why automated retinal image analysis?

Various vision-threatening retinal diseases include Diabetic Retinopathy (DR), Age-Related Macular Degeneration (AMD), glaucoma, retinal tear, retinal detachment, epiretinal membrane, macular hole, and retinitis pigmentosa. DR alters the structure of the blood vessels [8–12]. Hence, the study and analysis of blood vessel structure are vital for the diagnosis of retinal diseases [13,14]. DR is an ocular disease that is defined as a defect in the retinal vasculature that adversely affects the vision of the patients. In the developed countries, AMD is the largest cause of permanent loss of vision, and is the third leading cause worldwide. AMD, or age-related macular degeneration, is a condition that causes the sharp central vision to deteriorate over time. Glaucoma is the second largest eye disease that gradually affects the optic nerve and can potentially lead to partial or complete vision loss if it is not timely diagnosed and treated. Most retinal diseases do not exhibit any clear symptoms in the initial stages, which makes their accurate diagnosis a challenging task and requires the conduction of continuous intensive screening programs.

Ophthalmologists manually observe and detect any changes in morphological features in retinal images to detect such diseases. Such manual evaluation is not only prone to inaccurate judgments but also is time-consuming and thus difficult to adopt at a large scale (e.g., the entire population of a country) [15]. Fortunately, digital imaging coupled with the evolution of image processing techniques has emerged as a strong supporting tool for ophthalmology. Retinal fundus images can be used with computer-assisted diagnosis and staging tools to detect changes in the structure of blood vessels caused by these conditions. Automated retinal image analysis using computer-assisted tools is a significant step towards helping doctors make correct diagnoses of eye diseases at an earlier stage. Moreover, computer-aided tools may directly assist a large number of individuals in avoiding risks to their visual health. These tools, despite their limitations, have the potential to greatly ease pressure on public healthcare facilities. Therefore, Artificial Intelligence (AI)-driven medical image analysis and disease diagnosis methods have gained immense popularity in recent years.

1.2. Classical techniques for retinal image analysis

Many traditional techniques are used to analyze retinal images, which is important for detecting retinal diseases. In this regard, the steps consist of the detection, enhancement, measurement, and segmentation of retinal image features. To this end, morphology-based segmentation approaches are very famous which involve multiscale feature extraction [16], multiscale line detection [17], orientation-aware detection [18], wavelets transforms, Gabor filtering [19–21], contrast-sensitive schemes (local contrast normalization and a second-order detector) [22], morphological reconstruction and operations [19,23] for edge location refinement [24] are also used for segmentation. Other classical techniques for retinal image analysis involve Frangi's filter [25], Gumbel probability distribution function [26], locally adaptive derivative (LAD) [27], Hessian features [28,29], fractional derivatives [21], vessel's location map [30], and ensemble block

matching 3D filter [31]. There is also coarse-to-fine algorithm [32], a hybrid segmentation approach [33], and active contour model (ACM)-based approach that includes "Ribbon of Twins" active contour model approach [34].

1.3. Machine/deep learning for retinal image analysis

The increase in computational power has enabled machines to learn and interpret structures within data. Consequently, machine learning has emerged as a key area to develop AI-based methods to help humans resolve problems that are beyond their extent of scalability and intellectual capabilities. ML is a subbranch of AI that enables machines to learn, operate, and augment their procedures by gaining knowledge and experience from the data [35]. Such learning paradigms can be classified as supervised, unsupervised, and reinforcement learning based on the data structure and training objectives. A comprehensive review of recent trends and advances in ML paradigms for automated retinal image analysis is provided in [36].

The advent of DL approaches incites a more intensive system formation for drawing and exploiting the correlational features/structure in the provided data. For example, DL can be apprehended as a Deep Neural Network (DNN) which refers to an Artificial Neural Network (ANN) composed of multiple (deep) intricate transmissive hidden layers. In the past 5 years, the ability of discriminative (e.g., deep convolutional ANN) and generative DL methods as standalone or in combination with other methods has received high recognition for tasks such as automated segmentation, classification, and diagnosis. Alyoubi et al. [37] examined and analyzed the recent state-of-the-art methods for the detection and classification of DR color fundus images using deep learning techniques. An overview of the deep learning applications for ophthalmic diagnostics with retinal fundus images was presented by [38]. The authors described different datasets for retinal images that can be used for profound learning purposes. Stolte et al. [39] presented an exhaustive description of each step of DR diagnosis. The authors started the survey with an introduction to the disease and currently available technologies and resources and then discussed the frameworks used for DR detection and classification by different researchers. In [40], the recent approaches to machine learning used in the segmentation of retinal vessels and retinal layer methods and fluid segmentation are reviewed. Two main imagery methods were considered, namely imagery of color funds and tomography of optical coherence. Machine-learning approaches used for measuring the eye and for visual field data for detecting glaucoma are also reviewed. In [41], a thorough survey of recent advances in DL methods for automated retinal image analysis is presented, where particularly retinal blood vessel segmentation is reviewed.

Effective segmentation of retinal blood vessels in retinal images is globally recognized as crucial in the diagnosis of retinal and other diseases. In [42], a comparative review of advanced supervised and unsupervised ML/DL paradigms for retinal blood vessel segmentation is presented. All the aspects including fundus photography, open retinal image databases, important features extraction, and vital pre-and post-processing steps for segmentation operation are comprehensively discussed. In [43], a brief review of different pre-processing algorithms for enhancement of retinal images is presented. Despite the demonstrated success of ML/DL methods, the availability of an ample amount of data and strong processing capabilities is essential for critical applications such as automated disease diagnosis. In this regard, one of the primary goals of this paper is to describe the data and computational requirements for driving the scope of machine learning-driven approaches in developing robust retinal image analysis techniques.

1.4. Computing paradigm for ML/DL

The common difficulties associated with the efficient deployment of ML algorithms include:

1. The need for employing various ML algorithms before establishing the best choice;
2. If an ML model is trained with data that do not match the data it will encounter when deployed, the model's performance may be lower than expected [44].
3. Lack of a framework to set a large number of available model parameters, which leads to numerous tedious iterations before meeting the most suitable choice of setting [45];
4. Over-fitting of the results due to flexibility in the ML framework requiring cross-validation of results over multiple iterations on the data subsets [44];
5. A substantial amount of memory and processing capabilities required for the execution of algorithms [45].

The execution of prevalent ML algorithms on conventional processors containing limited cores involves large processing delays [46–48]. Exponential speed-up in computations can be potentially achieved through parallelization of the architecture and programming framework. In [49], a contemporary survey of parallel processing approaches to ML is conducted. The success in advancing the parallel processing and distributed learning methods together has recently renewed the research interests in data-driven approaches to complement the conventional mathematical modeling- and theory-based approaches.

A significant advancement in learning algorithms to exploit the leverage of a tremendous amount of available parallel processors, e.g., multiple cores available in graphical processing units (GPUs), has also been witnessed recently. In [50], the scope of GPUs to extend high-performance processing capabilities for medical image processing applications is reviewed. In [51], various fundamental image processing algorithms that are capable to be executed in a parallel fashion on multi-core CPUs and GPUs are evaluated in TensorFlow. The GPU-based implementation of TensorFlow outperforms multi-core CPUs with several time speed-ups. Furthermore, the advanced Tensor Processing Units (TPUs) have also shown an enormous potential to boost the processing speed and energy consumption for the execution of ML/DL algorithms. This progression has profoundly supported applications of DL methods in various engineering disciplines.

Besides these advancements in classical computing methods, the realization of tremendous parallel processing potential offered by Quantum Computing (QC) and related quantum technologies have strong potential in realizing the ambitions of fully intelligent and automated disease diagnosis systems. In [52], a comprehensive comparative review of classical computing and QC paradigms is conducted where applications of QC across various disciplines of engineering are highlighted. The disciplines of QC and ML have together advanced into an inspiring new framework of Quantum Machine Learning (QML). This emerging framework of QML combines the advantages offered by QC in terms of processing speed-ups and generating counter-intuitive statistical patterns and those offered by ML in terms of recognizing statistical patterns in the data and assisting QC in resolving the uncertainties of their states [53,54]. The research community has recently started exploring the application of this exciting emerging framework of QML across various signal processing applications such as medical image processing, wireless communications, natural language processing. Cloud computing for online retinal image analysis has a recognized potential [55].

The recent evolution towards decentralization of computing facilities across computer communication networks, i.e., evolution from cloud-computing towards edge-computing, has also facilitated the deployment of heavy ML/DL applications for mobile network users with

significantly reduced latency [56]. For example, the mobile edge computing (MEC) paradigm recently introduced in 5G communication networks has leveraged the network edge (e.g., Wi-Fi router) with heavy storage and processing capabilities [53]. This is anticipated to lead towards the offloading of computational tasks from user devices (e.g., mobile phones, computers, consumer electronics) to heavy-duty edge-computing facilities. Along with various other exciting anticipated use-cases, healthcare applications by exploiting the data acquired by mobile phone sensors is also an appealing application. The sensed/measured mobile phone data can be offloaded to the edge-computing facilities to execute heavy ML/DL-based disease diagnosis algorithms. Such user-side local applications of mobile phones can significantly reduce the load from public medical-care facilities. In this regard, exploration of low-latency automated retinal image analysis through edge-computing platforms for mobile users can be a potential future research direction.

One of the main objectives of this paper is to highlight recent advances and trends in computing platforms for employing ML/DL paradigms to facilitate automated retinal image analysis advancements.

1.5. Contributions and organization

There are various articles in the literature that review different aspects of retinal image analysis. Unlike the existing review articles, this article presents a holistic view of the entire retinal image processing theory including state-of-the-art of in retinopathy diagnosis, computer-aided tools, ML/DL methods, computing platforms, and other important aspects. This paper discusses the recent trends and advances in retinal image analysis and conducts a comprehensive review of retinal image segmentation and detection methods. A total of 27 publicly available datasets for the color retinal images have been reviewed in this article. Table 2 shows the associated retinal image features that are used for the segmentation from each dataset. A total of 161 articles have been comprehensively covered for retinal image feature detection and segmentation, from which 63 algorithms are discussed under unsupervised techniques and 98 algorithms are discussed under supervised techniques. The main contributions of this work are:

- We present an extensive review of retinal image acquisition and noise models to facilitate design of image pre-processing approaches in future studies.
- We systematically review and present an in-depth discussion on various eye diseases and corresponding retinal image features.
- We introduce the role of retinal images as diagnostic and prognostic biomarkers for chronic diseases.
- We provide an in-depth review of the most commonly used publicly available retinal image databases.
- We present a comprehensive review of the current state-of-the-art detection and segmentation techniques for retinal features, along with their progress in terms of methodological improvements and contributions.
- Systematic comparative analysis of notable existing retinal image analysis schemes is presented in addition to relevant discussions and clear conclusions regarding their applicability in various settings.
- Finally, we discuss research gaps in existing feature segmentation models and point to future directions by proposing an image-based system model for ophthalmic healthcare and monitoring.

The remainder of this paper's organization is as follows: Section 2 provides an overview of critical retinal imaging features that indicate the presence of one or more eye disorders. In Section 3, retinal imaging biomarkers for the diagnosis and prognosis of chronic disease were discussed. Section 4 provides insight into fundus image acquisition as well as the associated noise and artifacts. Subsequently, Section 5 provides a brief overview of existing pre-processing approaches used to handle low contrast, noise, and artifacts. Section 6 provides an overview of the available datasets and performance metrics, while Section 7 discusses

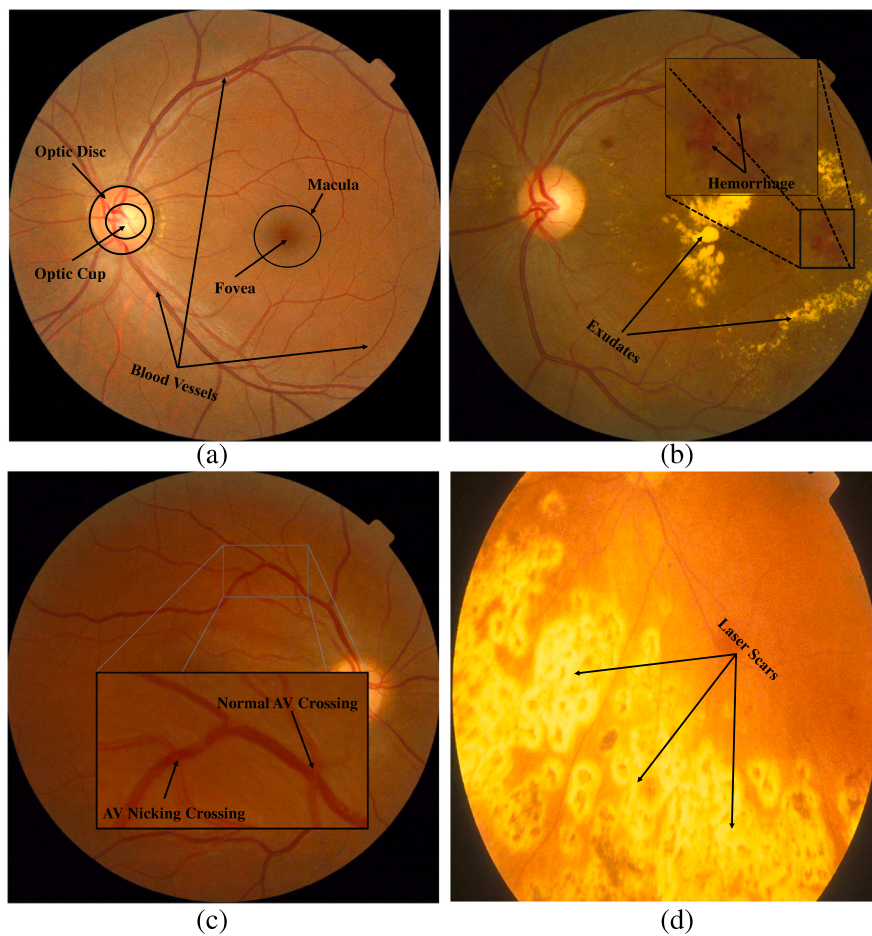


Fig. 1. Retina Features: (a) Blood Vessels, Optic Disk and Optic Cup and Macula (b) Exudates and Hemorrhages (c) Arteriovenous (AV) Nicking (d) Laser Scars.

feature extraction/segmentation for detecting retinal disorders. In Section 8, Network Parameters, Training, and Testing Time are discussed. Finally, Section 9 concludes the article by discussing future trends in retinal eye disease systems.

2. Retinal image features and eye diseases

This section defines the primary retinal features and discusses their significance in the automated retinal image analysis. Retina image analysis flow diagram is shown in Fig. 2. The analysis begins with the fundus cameras used for image acquisition followed by the image acquisition strategies. Once the images are acquired, the reprocessing is done followed by features segmentation and diseases classification. All the techniques of each block of Fig. 2 are thoroughly reviewed and discussed in the later sections.

2.1. Definition of key retinal features

An illustration of retina macular and peripapillary features is provided in Fig. 1. The following paragraphs discuss all the important retinal features.

2.1.1. Retinal blood vessels

Blood vessels are usually considered similar to each other as arteries and veins, as shown in Fig. 1(a). Blood vessel information helps to identify multiple disorders, such as diabetic retinopathy, and is often considered a landmark for eye surgery. Blood is carried by vessels to and from different parts of the eye [57].

2.1.2. Optic disk

The optic disk, a central yellowish part of the retina as illustrated in Fig. 1(a), is the point of entry into the retinal outgoing vessels. The optic disk has a circular shape that varies from person to person. Because it lacks photoreceptors, color-acquiring rods, and cones, the optic disk is known as the blind spot. It consists of a large number of neurons. A typical optical disk is orange to pink in color, whereas a pale optical disk has a disease condition [57].

2.1.3. Optic cup

Fig. 1(a) shows an optic cup, which is a variable-sized bright center depression on the optic disk. Along with the optic disk, the optic cup is used to diagnose glaucoma. By obstructing the optic disk, advancement of the optic cup causes glaucoma to progress. In a healthy retina, the optic cup is one-third the size of the optic disk and is smaller than the optic disk [57].

2.1.4. Exudates

Exudates are retina features widely used to diagnose diabetic retinopathy. Blood leaking from retinal blood vessels is the cause of forming exudates [58]. The fluid contains a lot of protein, white blood cells, and cellular debris, and it appears as bright yellowish patches in the retina. The retina of an eye with exudates is shown in Fig. 1(b).

2.1.5. Hemorrhages

Acute blood loss from a broken blood vessel creates hemorrhages, which appear as red dots in retinal images. Mild bleeding, such as when the skin's superficial vessels are damaged, resulting in petechiae and ecchymosis. It could also play a role, leading to a more ambiguous

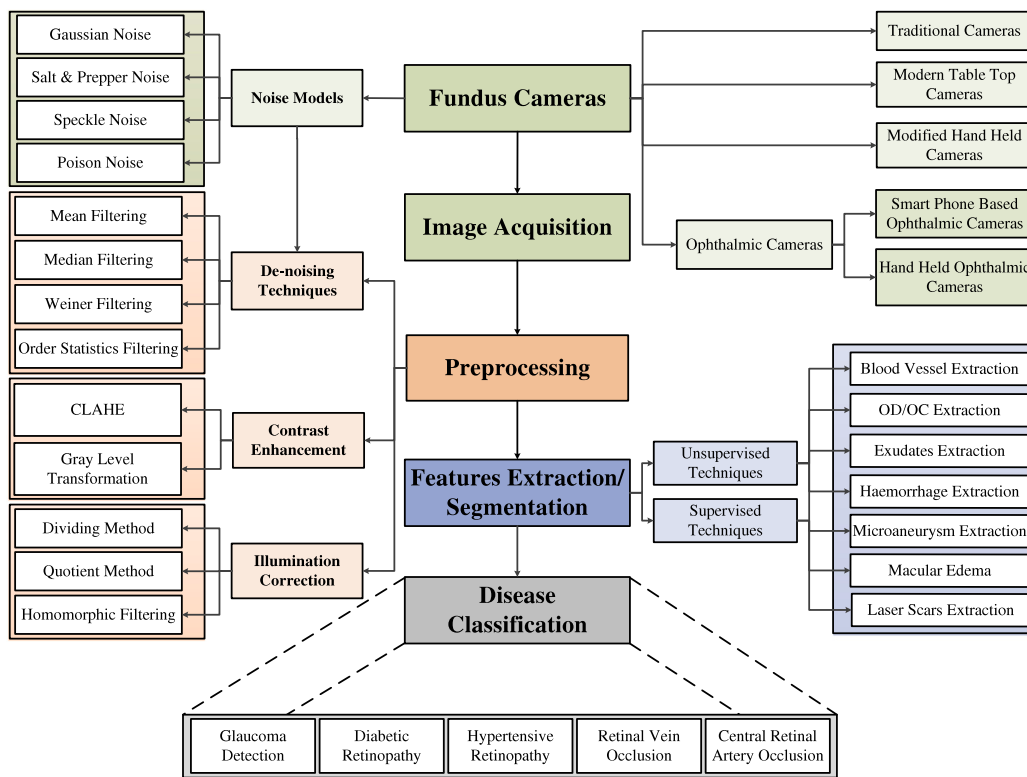


Fig. 2. Retina image analysis flow diagram depicting all steps involved, from fundus cameras to disease classification. Furthermore, this diagram shows the various techniques that are involved in each step.

symptom constellation, such as vital sign fluctuations and a changed mental state. The fundus images containing hemorrhages is shown in Fig. 1(b).

2.1.6. Macular edema

As shown in Fig. 1(a), Macular edema is a darkly pigmented region present in the center of the retina image. With an average diameter of 5.5 mm, it is yellowish color and is assumed to absorb ultraviolet rays and excess dark blue. Macular edema also serves as a sun block that is subdivided into fovea and umbo, specialized in various kinds of visions such as lateral, middle, etc. [57].

2.1.7. Laser scars

Laser scars occur characteristically in the macula as lesions of 50 to 200 μm in diameter or peripheral lesions of 300–600 μm . They are yellowish-white with centrally variable black pigment and round or oval in shape. The focal laser is known as a laser within the macula. Scatter lasers are classified as larger lasers, most of which are located outside the macula. They were graded as present if the laser scars were in the photograph but not in the macular or peripapillary fields. The retinal image of an eye with laser scars is shown in Fig. 1(d).

2.1.8. Arteriovenous (AV) nicking

Retina AV nicking is the condition in which the vein is squeezed by a stiff artery at its crossover point due to an increase in blood pressure [59,60]. AV nicking is seen as the decrease in the venular caliber on both sides of an artery-vein crossing in retinal photographs shown in Fig. 1(c).

In the literature, there are numerous research and surveys on retinal image processing. Patton et al. [61] examined the concept, use, and promise of retinal image analysis. In the study [62], a thorough overview is provided on retinal imaging modalities and techniques for image analysis. Fraz et al. [63] provided a comprehensive analysis

of 2- D fundus image techniques and methods for vessel segmentation and elongated structures. Faust et al. [64] presented a survey on DR detection techniques that include a variety of algorithms for retinal pathology detection. Winder et al. [65] presented a survey on image processing techniques used for the preprocessing, detection of the optic disk (OD), fovea, and detection pathology of DR. Yogesan et al. [66] addressed the advances made by retinal image analysis in automated screening of age-related macular degeneration (AMD). The recent progress achieved in the creation of DR evaluation automation was discussed by Zaki et al. [67]. A most recent study of image processing techniques used for exudate detection and segmentation in retinal images was proposed by Fraz et al. [68]. Joshi and Karule [69] presented a review of numerous early studies used for automatic detection of exudates in order to provide decision support to reducing an ophthalmologist's workload. Mookiah et al. [70], Mansour [71] assessed DR diagnosis based on the methodologies used, which included mathematical morphology, tracking of retinal lesions, threshold and matched filtering models, clustering models, matched filtering models, deformable models, and hybrid approaches. Almotiri et al. [72] presented an overview of retinal vascular segmentation techniques. Almazroa et al. [73] and Thakur and Juneja [74] investigated several approaches for the segmentation of optical disk and glaucoma diagnosis. Image preprocessing, basic and aberrant retinal characteristics segmentation and methods of DR detection were also highlighted in another the study [75].

2.2. Common eye diseases

Retinal vascular diseases and disorders are influenced by physiological artery wall hardening as people age, as well as pre-existing vascular disorders like high atherosclerosis and blood pressure. Retinal vein occlusion (RVO), hypertensive retinopathy, diabetic retinopathy, and central retinal artery occlusion (CRAO) are the most common retinal vascular diseases, as shown in Fig. 2.

2.2.1. Hypertensive retinopathy

When the vessels of the retina are damaged, hypertensive retinopathy develops, eventually leading to blindness. To promote early detection of hypertensive retinopathy, a variety of classification schemes have been established [76]. It initially affects the retinal blood vessels at all tributary levels. Sclerosis (thickening and hardening of the artery) is a procedure that can change the artery's tributary angles as well as the artery's elongated path. Furthermore, the artery and vein junction share a ventricular sheath. Sclerotic modifications to the artery in this enclosed region might further compress weaker venous arteries, causing further angular path changes in the veins [77]. Such angular alterations can be investigated and explored to see whether they have any relevance in the evaluation of disease progression.

2.2.2. Retinal vein occlusion

RVO disorder is generally linked to a large number of underlying systemic disorders, including blood pressure, diabolical disease, dyslipidemia and systemic vasculopathy. A number of blood vessels can be used for RVO. It includes centralized retinal veins, such as hemicentral retinal vein and small-scale veins like BRVO [78]. The occlusion of retinal veins can be divided into branches and central. In particular, the first or second tributaries of the branch retinal vein can occur at different levels. Imminent retinal vein occlusion may occur before full-blown vein blockage. During this phase, the damaged veins become more dilated, engorged, and tortuous, and the pathological process alters the affected veins' course and tributary angle [79]. These angular shifts can be studied to analyze if they have any significance on disease progression and evaluation.

2.2.3. Glaucoma

Glaucoma is the second largest cause in the developing world for permanent vision loss. This condition damages the optic nerve and ganglion cells directly [80–82]. The optic nerve of the affected eye has an irregular amount of optic nerve cupping. The causes of glaucoma include high blood pressure, obesity, increased eye pressure, and migraines. Glaucoma classified into three types: closed-angle, open-angle, and normal glaucoma. Open-angle glaucoma is the most prevalent type of glaucoma. It appears gradually and is painless, but it has the potential to blind the person if left untreated. Closed-angle glaucoma can develop slowly or rapidly. Perfusion in the retinal region and other organs, normal stress glaucoma is characterized by symptoms with the blood circulation, while the classical hallmark of intraocular pressure is not associated with this form of glaucoma. The diagnosis of glaucoma is based on intraocular stress analysis, the cup to disk ratio, the morphology of retinal vessels, the structure of the optical nerve, and the interior chamber angle [83].

2.2.4. Central Retinal Artery Occlusion

The Central Retinal Artery Occlusion (CRAO) is an eye disorder like an acute stroke of the eye. Unfortunately, these cases have been identified at the stage of viability of the necessary medical attention. The clinical manifestation with the central artery, as the retina is totally deprived of oxygenated blood, is always a pale retina with central, red cherry spots. It means end organ ischemia and is frequently the underlying atherosclerosis [84].

2.2.5. Diabetic retinopathy

Diabetes retinopathy is the world's fifth most prevalent cause of blindness [85]. The duration of diabetes, hyperglycaemia and high blood pressure are strongly associated with DR. Proliferative DR is characterized by vascular leakage and the formation of new retinal blood vessels, which is aided by the production of chemokines like VEGF, as well as macular diabetic edema, which is secreted by the central region of the retina [86]. Laser photocoagulation and steroid injections, anti-VEGF and vitreoretinal are some of the current intraocular treatments for diabetic eye disease [87]. The pathogenesis

of diabetic retinopathy first affects the retinal blood vessels. Due to weak regulations in glycemia, advanced glycemic end products (AGEs) may inevitably damage the pericyte that maintains retinal capillary cellular structures. This tends to result in weaker and leaky capillaries and supports retinal blood vessel micro-hypertension. Dilated, tortuous vessels with a change in course and tributary angles are among the vascular retinal alterations [87].

2.3. Retinal image analysis

Retinal images acquisition, preprocessing, and analysis are the primary steps in the detection and classification of retinal diseases [88, 89]. A taxonomy of retinal image processing and associated diseases is presented in Fig. 2, where the complete process of retina image analysis is illustrated. All the blocks indicated in Fig. 2 are thoroughly discussed in the sequel.

3. Retinal imaging as biomarkers for diagnosis and prognosis of chronic illness

The eye is made up of numerous types of tissue. This one-of-a-kind characteristic makes the eye susceptible to a wide range of diseases and provides insight into numerous body systems. Almost any part of the eye can provide crucial diagnostic information for systemic diseases. The outer surface of the eye (eyelids, conjunctiva, and cornea), the middle of the eye, and the back of the eye may exhibit symptoms of a systemic disease. There is a strong correlation between the condition of the blood vessels (arteries and veins) in the eye and the condition of the blood vessels (arteries and veins) throughout the body. In this section diseases and parameters predictions from retinal images in predicting non-ocular diseases and parameters are briefly discussed. Fig. 4 shows the associated diseases with retinal images.

3.1. Age and gender prediction

There are multiple articles available that used retinal images to predict age or gender [90–98]. Additionally, Rim et al. [94], looked at model performance in external datasets, which revealed low generalizability. Age was accurately predicted for Chinese, Indian, and Malay ethnic groups in subgroup analysis of the Singapore Epidemiology of Eye Diseases (SEED) dataset. Yamashita et al. [95], attempted to determine what traits are identified by algorithms as effective in identifying gender as a follow-up to Poplin et al. [93], which shown that RFP may be used to predict gender. On a number of traits linked to sex, such as the papillomacular angle, tessellation fundus index, retinal vessel angles, and retinal artery trajectory, logistic regression was conducted. In a Qatari dataset, Gerrits et al. [97] conducted a similar analysis of age and gender. They anticipated that their system would inadvertently predict age or gender while functioning on other intended biomarkers. For instance, significant disparities in model performance for relative fat mass and testosterone were reported between males and females. However, gender prediction performance in age-stratified subgroups and vice versa were comparable, indicating that the features employed for age and gender prediction are mainly independent [97]. The optic disk, macula, peripapillary region, and bigger blood arteries inside the posterior pole seem significant for gender and age prediction, according to Munk et al. [92] and Poplin et al. [93] in their examination of activation maps. Non-random sex prediction with RFP appears to be possible only if the fovea and optic disk are visible [92]. To predict gender, Korot et al. [90] experimented with a code-free model (AUC: 0.93). A graphical user interface (GUI) was developed using the Google Cloud automated machine learning (AutoML) platform to enable doctors without coding experience to create ML models for medical images. This implies that a code-free framework might be on par with cutting-edge algorithms created by programmers for related tasks. Although age and gender were two of the first factors to be predicted from RFPs by neural networks since they are unambiguous and readily available as data, we note that employing AI to predict them has poor clinical utility by design.

3.2. Alcohol status and smoking prediction

Current models describe noteworthy prediction performance for smoking and drinking status [93,96,97,99]. The range of the AUC for smoking status was 0.71 to 0.86. Zhang et al. [96] was the only one to predict alcohol status (AUC: 95.00%). The phrase “current alcohol drinkers of 12 times in the past year” was used to describe “alcohol status” [96]. The “ground-truths” for these measures are patient self-reports collected through questionnaires, it should be noted. As a result, model performance would be constrained by information bias and patients’ candor when disclosing their drinking and smoking habits.

3.3. Body composition factors prediction

Body mass index (BMI), body muscle mass, height, weight, relative fat mass, and waist-hip ratio (WHR) are all body composition characteristics predicted from retinal images [93,94,96,97]. Current BMI prediction algorithms typically perform poorly. Additionally, there was weak model generalizability across ethnically diverse samples. Rim et al. [94] discovered that DL algorithms for height, body weight, BMI, and other non-body composition parameters showed low generalizability in the UK Biobank dataset (mainly White ethnicity). These algorithms were trained on a South Korean dataset. It was shown that there was a proportional bias, with expected values in the lower range being overstated and predicted values in the higher range being underestimated. While BMI is a metric of relevance because of its proven connections with overall mortality [100] and cause-specific mortality [101], prediction of other likely body composition factors has been published. The prediction of body muscle mass is interesting because it may be a more accurate indicator for dietary status and cardiometabolic risk than BMI [94]. Future DL algorithms may be useful for screening for sarcopenia if they show increased generalizability and prediction results. Zhang et al. predicted WHR, which has been linked to complications from diabetes and the cardiovascular system, with an AUC of 0.70. [102,103]. The prediction results appear more promising than those for BMI, but they still require more testing.

3.4. Cardiovascular disease and parameters prediction

Cardiovascular parameters predicted from retinal images include systolic and diastolic blood pressure (BP), hypertension, retinal vessel caliber, coronary artery calcium (CAC), and carotid artery atherosclerosis [93,94,96,97,104–107]. Retinal images are regarded to be reliable input images for predicting cardiovascular illness because they directly capture several retinal traits linked with increased cardiovascular risk, such as vessel diameter, tortuosity, and bifurcations [108,109]. CAC is a pre-clinical atherosclerosis marker generated from cardiac CT data [110]. Rim et al., rim2021deep developed a deep learning-based CAC score predicted from RFP (RetiCAC) and utilized it to stratify cardiovascular risk. A novel three-tiered cardiovascular disease risk stratification approach was proposed based on RetiCAC, and it demonstrated performance comparable to cardiac CT scans (the preferred clinical imaging technique at the moment) in terms of predicting future CVD events. Therefore, this study implies that RFP, a non-radiation-based imaging modality for cardiovascular risk stratification in low-resource settings, could be used as a more practical way than cardiac CT. Poplin et al. [93] developed models to forecast the development of significant unfavorable cardiovascular events within the next 5 years.

3.5. Hematological parameters

Anemia, hemoglobin concentration, red blood cell (RBC) count, and hematocrit are all hematological characteristics predicted from retinal images [94,96,111]. Prediction of hematological parameter cut-off points has been done using DL algorithms based on ophthalmic imaging (as a classification task). For instance, Mitani et al. [111] and Zhang et al. [96] both predicted anemia classifications and hematocrit ranges from fundus images with an AUC > 0.75. Attempts to predict continuous parameters such as RBC count [111], hemoglobin [94], and hematocrit [94,111] using fundus images were similarly less successful (RBC count, hemoglobin, and hematocrit). Mitani et al. [111] investigated the significance of several anatomical features in anemia further by blurring and cropping the retinal images during both training and validation. Notably, when the upper and lower hemispheres of the images were gradually masked, performance began to drop only after 80% of the image had been covered. AUC decreased when only 10% of the image was masked using a central horizontal line (covering the disk and macula). The models outperformed chance even after high-resolution information was eliminated with significant Gaussian blurring and image pixels were randomly scrambled, implying that the algorithms may use the general pallor of the retina to forecast anemia.

3.6. Neurodegenerative diseases

The majority of research that predicted neurodegenerative disease in recent literature used OCT-based models. These will be outlined in the sections that follow. Tian et al. [112] employed RFP to predict Alzheimer’s disease, with promising results (Accuracy: 82.00%, Sensitivity: 79.00%, Specificity: 85.00%). Saliency maps revealed that small retinal artery shape was more important than large vessels in the categorization decision, which is consistent with earlier research on the constriction of small cerebral arterioles in the etiology of neurovascular dysfunction in Alzheimer’s disease [113]. Tian et al. [112] went on to discuss the automated, multi-stage ML process that was utilized to build the retinal images based model, indicating the preliminary potential of retinal vasculature analysis using ML for Alzheimer’s Disease screening. It included a SVM classifier, a vessel map generator based on U-net, and an image quality selection and excluder [112].

3.7. Metabolic disease and parameters

Diabetes, diabetic peripheral neuropathy, fasting plasma glucose (FPG), HbA1c, triglycerides, and testosterone are among the metabolic disease states/biomarkers predicted from retinal images [93,96,97,114,115]. Although, retinal images based predicted testosterone levels, Gerrits et al., gerrits2020age discovered that the model also predicted gender indirectly. Model performance reduced when trained purely on male and female subgroups, showing that structural elements of RFP that are crucial for gender prediction are utilized in calculating testosterone. Given the emergence of tele-ophthalmology-based screening tools for diabetic retinopathy, and pre-existing connections of diabetic peripheral neuropathy with retinal vascular characteristics. Benson et al. [114] suggested using retinal images from DR tests performed annually to evaluate diabetic peripheral neuropathy as well. The process involved dividing retinal images into 50×50 patches, extracting information from each patch using a neural network, dimensionality reduction, and merging the patches for use in an SVM classifier. The chance of obscuring tiny, focused structural details across the retina was reduced by splitting RFP images. This method generated encouraging results (Accuracy: 89.00%, Sensitivity: 79.00%, Specificity: 85.00%) [114], but further testing in clinical settings and external validation are needed. Cervera et al. [115] also trained a neural network to identify diabetic neuropathy in RFPs. On the validation set, the AUC to predict DN on the entire cohort was 80.10%, and on the external test set, it was 71.00%. In the subset of patients with DR, the AUC improved to 86.73%.

3.8. Renal diseases and parameters

Renal parameters from retinal images such as chronic kidney disease (CKD), estimated glomerular filtration rate (eGFR), and serum creatinine. The retinal images based model developed by Sabanayagam et al. [116] performed well in internal and external testing. They also built models with CKD risk factors (age, gender, ethnicity, diabetes, and hypertension status) as inputs, as well as a hybrid model with both retinal images and risk factors, revealing that when utilized as inputs for CKD risk assessment, retinal images and risk factor information have equal predictive capacities. Furthermore, the RFP-only model performed similarly to the total cohort in subgroups of patients with diabetes and hypertension, indicating the clinical value of retinal images and DL as an alternative CKD screening method. This was followed by another article by Zhang et al. [117], who developed DL models with AUCs of 85.00%–93.00% to identify CKD and type 2 diabetes solely from fundus images or in combination with clinical metadata (age, sex, height, weight, BMI, and blood pressure). Rim et al. [94] developed a model that predicted creatinine levels with moderate accuracy, when trained and evaluated on a South Korean dataset but was unable to transfer to a European dataset. Kidney function predicted poorly in both the White and non-White groups.

3.9. Hepatobiliary disease and parameters

Existing studies predict total and direct bilirubin levels, liver cancer, cirrhosis, chronic viral hepatitis, non-alcoholic fatty liver disease (NAFLD), cholelithiasis, and hepatic cysts [96,99]. Previously, Rim et al., rim2020prediction attempted but failed to predict alanine aminotransferase (ALT) and aspartate aminotransferase (AST) using retinal images as continuous variables. While Xiao et al. [118] obtained moderate to good predictive performance in a variety of hepatobiliary diseases (AUC ranging from 62.00% for chronic viral hepatitis to 0.84 for liver cancer), the retinal structural alterations caused by hepatobiliary dysfunction are currently unknown. According to Xiao et al. [99], undetectable retinal abnormalities could be caused by hyperammmonemia, hypoalbuminemia, and reduced testosterone inactivation. Retinal vascular channels can change as a result of elevated portal venous pressure brought on by cirrhosis or splenomegaly, and fundus photography can reveal anemia brought on by splenic sequestration.

4. Image acquisition and noise models

Retinal image acquisition is a primary step which plays a crucial role in the treatment and control of eye disorders such as AMD, DR, and premature retinopathy (ROP) — to name a few. A fundus imaging system or retinal camera is a sophisticated low-power microscope which employs a CCD camera designed to capture the interior prospects of the eye, including the retina, optic disk, macula and posterior pole (i.e. the fundus). Subsequently, the image captured with a digital camera is encoded as a color value matrix. In each pair ($i:u(i)$), $u(i)$ represents a triplet of red, green, and blue component values called pixels. Each of the pixel values $u(i)$ are obtained as an output of measured light intensity, normally performed by a CCD matrix coupled with a light focusing device. Minimization of measurement noise during the image acquisition stage is a crucial task. This section provides an overview of some fundamental image acquisition methods and associated noise models in the following subsections.

4.1. Fundus camera

A fundus camera is essentially a low power microscope used to enlarge internal details within the fundus of the eye which are eventually captured through the image sensor (i.e., a camera) [119,120]. It is widely used for clinical diagnosis of the eye. For this purpose, fundus of the patient's eye is accessed through the pupil that is dilated to

obtain full view. The resulting black and white or colored fundus image provides a deep insight into morphological details of the blood vessels in the eye [121,122]. Recent advances in fundus imaging technology permit concurrent view of the fundus and external eye while some allow recording of a colored video clip of the internal details the fundus. Thus enabling a dynamic as well as interactive evaluation of the interior of the eye [119,123].

The progress on fundus imaging began way back in 1886 when jackman and Webster [124] published Retina photographs. The next advancement was Carl Zeiss' first publicly available fundus camera developed in 1926, after which major changes were implemented to the field of view (FoV) [125]. In 1927, as reported by Donaldson et al. [126], Metzger used the side-by-side shifting technique to obtain stereoscopic fundus images. In 1953, Hansell et al. [127] successfully connected the camera with an electrical flash tube, allowing light to pass through the pupil. In 1960, a groundbreaking 148° FoV camera that is Pomerantzeff Equator-Plus fundus camera was introduced by Behrendt et al. [128]. Steven Sasson has invented Eastman Kodak's first digital camera in 1975 [129], as reported by and the successive transition of revolutionized record-keeping of analog to digital. Confocal laser ophthalmoscopy scanning has gained favor in recent years as a method of reducing aberrations caused by poor dilation while simultaneously providing high-contrast, detailed images [130]. Camera systems have improved over the years to include sharper images, nonmydriatic wide-field options, pupil monitoring, and, most recently, mobility. Today's popular manufacturers include Topcon, Kowa, CSO, Zeiss, Nidek, Canon, and CenterVue. Standard fundus cameras deliver images of high quality but they are, however, cumbersome, office-dependent, technician-focused, and expensive. In addition to having access to the retinal imaging instrument, affordability is crucial in screening programs, especially in the most remote places. Recently, significant technological advancements have revolutionized retinal photography. Smartphone and telecommunications advancements are two major advances that have made ophthalmic screening a viable option in remote areas.

4.1.1. Working principle of traditional fundus imaging systems

Indirect monocular ophthalmoscopy is used to design a basic fundus camera system [131]. A common design by Knoll et al. for a traditional tabletop fundus camera was used as a reference design [132]. The fundus camera is made up of optical components like focal and condensing lenses, beam splitters, mirrors, masks, polarizers, and diffusers that focus illumination light entirely through the pupil of the eye, capturing light reflected from the retinal surface and relaying it to imaging optics, which creates a retina image on the detector screen [133].

An insight into a traditional fundus imaging system is provided in Fig. 3 (which is inspired from [119,120,134]) that shows a sophisticated mechanism built around an ensemble of reflective and light focusing lenses followed by CMOS/CCD image sensors. The purpose of this microscope-like-architecture before the imaging system is (a) to make high intensity light incident on the retina through the pupil of the eye for illuminating the otherwise dark regions and (b) to enlarge interior of the retina to an extent that micro-vessel structure within the retina is visible to the camera. Thus facilitating the capture of the morphological details of blood vessels within the retina using the sensitive CMOS/ CCD (photodiode) sensors.

The imaging mechanism kicks off when light is generated by either of the viewing lamp or flash light (depicted using the 'Bulb' symbols attached to the power supply in Fig. 3). That is subsequently filtered and focused on to a mirror for reflecting the light up, shown in the lower left of Fig. 3. Here, again a series of focusing lenses are used to collect the light that is subsequently shaped into a doughnut via a mask in the upper most lens. This doughnut shaped light is subjected to the rounded mirror with central aperture that directs it towards the eye of the patient through the objective lens that is shown at the top left of Fig. 3. As light enters the cornea and back scatters, the light

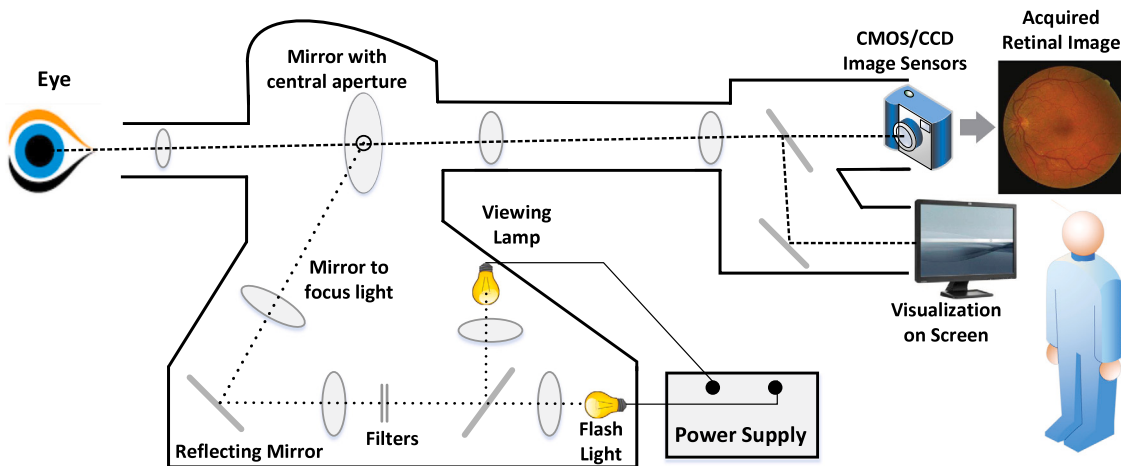


Fig. 3. A depiction of the process adopted in fundus cameras for the imaging of the retina.

Diseases and Parameters Prediction from Retinal Images		
	<ul style="list-style-type: none"> • Age and Gender • Alcohol Status and Smoking • Body Composition Factors • Cardiovascular Diseases • Hematological Parameters • Neurodegenerative Diseases • Metabolic Diseases and Parameters • Renal Diseases and Parameters • Hepatobiliary Diseases and Parameters 	

Fig. 4. The most common systemic diseases that affect the eye.

rays exiting the cornea pass through central mirror and focusing lenses for their eventual collection by an array of imaging (CMOS/ CCD) sensors, see Fig. 3. The imaging sensors convert the light into electrical signals which are stored as pixel values after some post processing that eventually results in an image of the fundus in the background. More clear understanding of the imaging principle, interested readers are advised to go through [119].

Mostly, the alignment of the fundus camera is dynamically adjusted by exposing the black and white pupil of the patient. However, in some cases, split pupil is presented to accurately measure the working distance of the camera. Afterwards, a powerful lens is brought into place (that typically causes a clunk) to mitigate optical power of the crystalline lens and cornea of the eye. That results in an inverted white and black view through the dilated pupil. In this regard, color images are obtained using more sensitive imaging sensors for sensing low levels of light in the absence of light filters [123]. Advanced systems of these devices offer additional features such as algorithms and automated analytical methods. Autofluorescence camera systems, angiography, fundus fluorescein, and green angiography with indocyanine all use filters [135]. Relevant limitations affecting the use of conventional table-top fundus cameras prompted the requirement for a miniature fundus camera system. First, they are a big system with a variety of mechanical and optical components, and aligning each part with the others is a crucial parameter for high-quality images. Second, the operation of sophisticated systems demands highly qualified individuals. Third, the instrument's weight and complexity limit its application to high-end healthcare settings, making it impossible to reach rural areas. Fourth, the cost of cameras has risen due to the increased number of optical components and add-on functions in modern devices, making them

prohibitively expensive to install in rural areas where a big percentage of the population suffers from visual morbidity.

4.1.2. Modern table-top fundus cameras

Advancement in the development of optical sources and detectors had already resulted in a lower cost manufacturing of optical assemblies. Miniature table-top fundus camera system designs have emerged in line with these developments which provide retinal images comparable to those of traditional fundus cameras. Icam [136], 3nethra [137], Digital Retinography System [138], EasyScan [139], TRC-NW400 [140], ZEISS CIRRUS 6000 [141], Non-Mydriatic Fundus Camera nonmyd WX3D [142], Canon The MULTIFACETED CX-1 [143] and California Ultra-Wide field Retinal Imaging [144] are some of the commercially available modern table-top fundus cameras. Most models have add-on features which contribute to the camera's extra size and weight. Patients have to sit upright to take photographs. It is essentially an office-based procedure, and therefore warrant a clinic visit. The total cost of most table-top models is high, and implementation may be restricted due to financial constraints in primary health-care. Such factors limit their use to units in high-end healthcare specialties.

4.1.3. Off the shelf point-and-shoot hand held fundus cameras

The research groups have integrated commercially available digital cameras with low-cost lenses to capture images of the retina. These prototype designs are small and light, and they can capture high-quality retina images [133]. The light sources for the illumination are LEDs and a xenon flashbulb. The camera-based CMOS sensor provides a 50° retinal FoV with its autofocus and exposure capabilities. Although commercial point-and-shoot cameras offer a simple, lightweight, and

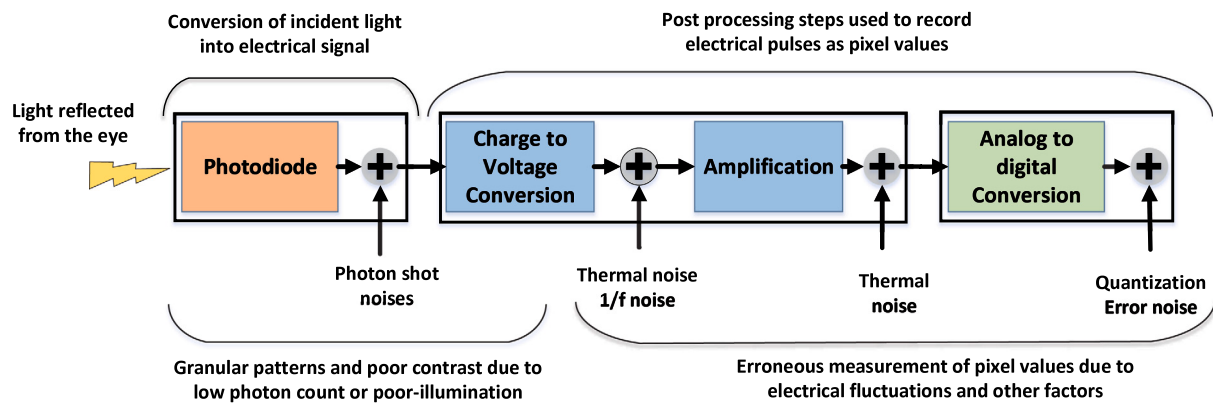


Fig. 5. An illustration of imaging stages involved in acquisition of pixel value using CMOS/CCD sensor and associated noise(s).

portable option, they lack fixed objectives for correct focus. Furthermore, artifacts in images are caused by corneal refractions and common optics, limiting the clinical application of these prototypes.

4.1.4. Integrated adaptor-detector-based hand-held ophthalmic cameras

High-resolution detectors were used to incorporate illumination optics to ensure accurate, high-definition image capture in integrated adaptor-detector-based hand-held ophthalmic cameras. The basic design of the integrated hand-held camera was based on an adaptor-detector. Panoptic Ophthalmoscope [145], Volk Pictor [146], VersaCam [147], Horus Scope portable fundus camera [148], Optomed Aurora [149], Genesis-D [150] and Riester Ri-Screen Multi-functional Digital Camera System [132] are the commercially available integrated adaptor-detector-based hand-held ophthalmic cameras. The manual alignment with the optical axis of the illumination beam is a critical condition for photographs of good quality and is time consuming.

4.1.5. Smart phone-based ophthalmic cameras

Smartphones have opened way for many applications with faster processors, smaller batteries, a larger memory storage and advanced operating systems. Research over the use of smart phones for medicine is on the rise, but there are limited data on their usefulness, efficacy and impact as medical tools. Advances in technology enable smart phone-based attachments and integrated lens adaptors to transform the smart phone into a fundus cameras [151–154]. The commercially available current smart phone-based ophthalmic fundus cameras are iExaminer [153], Ocular Cell-Scope [151], and Compact Eye Test Kit [152]. iPhone 5 or later versions of light sources must be tested for compliance with safety standards [122]. Beam alignment is a challenge when using smartphone-based imaging systems. The built-in flash of the iPhone has a relatively high intensity which restricts the pupil. As a consequence, image capturing is difficult and requires pupil dilation or the use of special software to adjust the strength and exposed time of the flash for optimal illumination. These lens adaptors currently use the iPhone's built-in flash as a coaxial light source itself, but attempts are being made to build lens adaptors that use coaxial light sources such as external LED's with varying intensity levels [135,151,152].

4.2. Noise models

Noise in the retinal images generally refers to distorted and blurred pixels which seem to intensify within the insufficiently illuminated areas. Since, illumination is typically good at the center of the image, low image quality regions are located near the edge of the retinal image. The regions with proper illumination are also corrupted by systematic additive noise that is apparently less severe and is partially dealt with during the post processing. Hence, the unwanted noise(s) within the regions of poor image quality are the major cause of concern during the detection of features. Moreover, the image degradation caused by

external interference may also yield spatial noise [155]. Consequently, these unwanted artifacts should be identified and discarded before feature detection.

Imperfections in the fundus camera optics, human eye aberrations and unsuitable camera adjustment, focusing, or flash lighting during the test are a main sources of noise in the retinal images [156]. An illustration of various stages involved in image acquisition is given in Fig. 5 that presents an account of unwanted noises introduced due to CMOS or CCD sensors (inspired from [157–159]). The working principle of CMOS or CCD imaging sensors is based on conversion of the incident light into an electrical signal that is subsequently recorded as a pixel value. The orange block in Fig. 5 depicts a photodiode that introduces various types of shot noises which not only distort the actual value of the pixel but also adversely impact the contrast of the image. The primary cause for the shot noise is the lack of proper illumination on the scene which results in low count of photons reflected from a dark region of the eye. This type of degradation is the main cause of concern in retinal images as it significantly degrades the quality of the retinal images and results in dark regions and poor contrast [156,159].

Secondly, fluctuations in electrical signals during amplification and other post processing steps lead to errors in capturing the actual pixel values resulting in deterioration of the actual information. That is depicted using the blue blocks in Fig. 5. Major cause for the electrical fluctuations is heating phenomenon within the electronic components that introduces thermal noise which happens to be the most dominant noise due to electronic devices. Albeit various other noise(s) are also observed, e.g., 1/f noise or flicker noise, quantization error noise, etc. These noises are mostly additive in nature except in some cases where sharp fluctuations lead to unwanted binary patterns of bright and dark pixels. The quantization error depicted using green block in Fig. 5 is also modeled as undesired additive noise [156,158,160]. Finally, scattering phenomena within the microscope part of the fundus camera (see Fig. 3) may lead to the introduction of multiplicative noise within the fundus image. The distortion caused to each pixel by this multiplicative noise is termed as 'speckle' that is also observed in ultrasound images due similar scattering phenomenon. Its impact is much worst than systematic additive noise since it scales down the actual pixel values and results in an overall darkening effect in the image [161–163]. These noise(s) may be further classified into temporal and spatial categories. Examples of temporal noise include photon shot noise, reset noise, noise from the output amplifier and shot noise of dark current. Spatial sources of noise include dark current non-uniformity (DCNU) and photo response non-uniformity (PRNU). Modern cameras are somewhat capable of dealing with these undesired effects to some extent but the large part of alleviating this issue is performed post imaging using image processing techniques [158,159].

Restoration or enhancement of retinal fundus images is a complex problem owing to the presence of noises of varying nature. In general, denoising techniques are based on predefined noise models which are

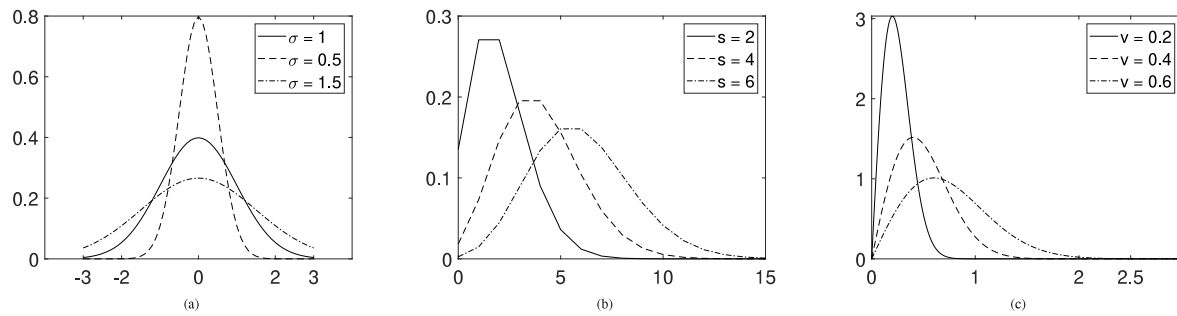


Fig. 6. Noise Models: (a) Gaussian distribution for a range of noise variance σ , (b) Rayleigh distribution plots for a range of noise parameter s , (c) Poisson noise distribution plots with different signal strengths v .

developed based on experimental evaluation and statistical analysis the noises originating from different phenomena. Henceforth, we first discuss the models used for various types of noises followed by a discussion techniques used to remove these noises

4.2.1. Additive white Gaussian noise

Disturbances due to electrical fluctuations are dominated by thermal noise that results from an inevitable heating phenomena within the electrical devices [158]. Since, thermal noise is known to follow Gaussian distribution, the mixture of noises due to electrical components, which also includes flicker noise, quantization error etc., is widely modeled as an additive white Gaussian noise (AWGN) [164–166]. Here, the term white is coined to stress on the presence of all frequencies within the AWGN. In case, an additive Gaussian noise contains a certain band of frequencies only, it is termed as colored Gaussian noise. Traditionally, images captured in good lighting conditions are assumed to be predominantly effected by AWGN which arises due to electrical components. Therefore, a noisy pixel x corrupted by AWGN is modeled as follows:

$$x = s + \eta, \quad (1)$$

where s denotes the true pixel value and η denotes an instance of AWGN that is modeled using a Gaussian distribution given as follows.

$$G(\eta) = \frac{1}{\sigma\sqrt{2\pi}} e^{-\frac{(\eta-\mu)^2}{2\sigma^2}}, \quad (2)$$

where σ denotes variance of noise and μ denotes the mean. Since AWGN is assumed to be zero mean, i.e., $\mu = 0$, in practical cases, the variance parameter σ is of particular relevance that relates to the noise strength in the input signal. In Fig. 6(a) we have plotted various instances of Gaussian distribution for varying σ . Naturally, σ increases the spread of the noise distribution, i.e., higher amount of variations among the recorded noise observations. That makes it increasingly difficult to tackle such noise.

Moreover, noise in each pixel is modeled independently owing to a wide spread assumption that AWGN samples are independent to each other [164,167–169]. This assumption is made due to the fact that consideration of spatial correlations within AWGN samples makes the statistical analysis and study a complex job that is some times intractable. Owing to this practical limitations noise in every pixel is modeled independently.

4.2.2. Poisson noise

CMOS or CCD sensors are essentially light detecting diodes used to convert the incident light into electrical signals which are subsequently amplified, filtered and post processed before recording those as pixel values. In low light conditions or poor illumination, these photodiodes are starved of photons, i.e., low count of photons is received at the diode. That leads to shot noise which not only distorts the signal values but also leads to low contrast in the image. Unlike the systematic additive noise, shot noise is difficult to deal with as its dependent on

the intensity (or magnitude) of true signal. Hence, the signal corrupted by shot noise is modeled using Poisson distribution [159,170]. In case, AWGN is also present in the image along with the shot noise, this mixture noise is modeled using the Poisson-Gaussian distribution [159]. A pixel value y corrupted by signal dependent shot noise is modeled as follows

$$y = s + \phi(s), \quad (3)$$

where $\phi(s)$ is the Poisson noise that is dependent on the true signal value s . Here the pixel y is modeled using Poisson distribution $P(y|s)$ given as follows

$$P(y|s) = \frac{s^y e^{-s}}{y!}, \quad (4)$$

where ! denotes the factorial operation. It is evident from Eq. (4) that true signal strength s has direct impact on the stretch of noise dynamics which is why tackling the case of signal dependent Poisson noise is a challenging job. To demonstrate how strength input signal s translates into the adversity of this signal dependent noise, we have plotted various instance of Poisson distribution in Fig. 6(b). Clearly, increasing the input signal strength expands the range of noise PDF which means, in low light conditions, shot noise adversely impacts the regions of higher signal activity.

In case, the systematic AWGN η is also part of the image then the acquired pixel is modeled as follows

$$y = s + \phi(s) + \eta. \quad (5)$$

Hence, the resulting pixel y is modeled using a mixture of Poisson and Gaussian distribution, commonly referred to as Poisson-Gaussian distribution [171].

4.2.3. Salt and pepper noise

Salt and pepper noise is caused by sharp or sudden fluctuations of electrical signals that may be caused by camera sensor failure, a digital image or a transmission-sync error, or memory cells failure etc [169]. That results in a pattern of dark pixels (i.e., zero value) and bright pixels (i.e., maximum pixel value) across the image. It is also referred to as Impulse noise or binary noise that is assumed to be flat-tail distributed. Generally, the probability of corrupted pixels is less than 0.1% that are alternatively set to the minimum or maximum value, giving the image an appearance like “salt and pepper” [172]. The pixels not effected by this phenomenon stay unchanged while those affected either have pepper noise (i.e., 0) or salt noise (i.e., 255 for an 8-bit image).

4.2.4. Multiplicative speckle noise

Speckle noise is generally observed in imaging systems where electromagnetic signal or light rays are thrown on the scene and back scattered signal/ rays are collected to construct an image. In these type of imaging systems scattering phenomena leads to a granular effect termed speckle noise. In fact, speckle is a form of the recorded signal but owing to the deterioration that it causes it is treated as a noise.

Since, this speckle phenomena is caused by loss in reflective light back to sensor, it is modeled as a multiplicative noise given as follows

$$z = s \cdot \psi, \quad (6)$$

where z is the pixel value corrupted by multiplicative speckle noise ψ . Experimental studies reveal that speckle follows Rayleigh distribution that is given below.

$$R(\psi) = \frac{\psi}{v^2} e^{-\frac{\psi^2}{2v^2}}, \quad (7)$$

where v is the scaling parameter of the Rayleigh distribution [31,173]. A depiction of how PDF of speckle noise changes with change in v is shown in Fig. 6(c) whereby it is evident that higher v increases the strength of Rayleigh distributed (speckle) noise.

5. Retinal image pre-processing

Normally, the fundus image contrast is high in the middle and decreases with respect to the pixel distance away from the center. Pre-processing reduces this effect and by normalizing the mean intensity of an image to get more uniform image. There are many reasons for the non-uniform illumination of fundus images such as the narrow lens in the fully dilated eye, variability in light reflection and diffusion, noise, poor contrast, variations in retinal pigmentation and variations in cameras, limitations of the instrument as a ring-shaped model illumination pattern and imagery related to variance in illumination axis of the eye with respect to optical axes. In terms of luminosity and contrast, the main factor for in-homogeneity lies in the same image or between images. Retina image pre-processing flow is shown in Fig. 2.

5.1. De-noising techniques

A large variety of approaches for image denoising have been presented in recent years. These approaches can essentially be classified into two categories: Classical Gaussian-filtering techniques; Edge-preserving techniques.

5.1.1. Classical Gaussian-filtering techniques

The edge information as a major feature of an image may be lost using traditional Gaussian-filtering approaches [174–178] and edge-preserving approaches [179–181], which preserve prominent edges during denoising process. In the examination of medical images, Gaussian-filtering-based techniques are often used. However, because a Gaussian filter's weights are only based on spatial distance, such approaches can lose the salient edges and produce blurring, making it harder to distinguish features in retinal images.

5.1.2. Edge-preserving methods

The Edge-preserving methods are used for overcoming the prominent edges loss. For example, the weighted minimum square filter [181] and based on image gradient measurement, the anisotropic diffusion filter [180] tries to smooth images while retaining edges. The non-local means filter determines filtered results based on the similarity of intensities and order of pixels in their neighborhoods [182–184]. Bilateral filter (BLF) is characterized for its capability of preserving edges, which combines a spatial kernel and a range kernel and for which the output of every pixel depends on the differences in intensity and spatial distance [179]. BLF is perhaps the most extensively used one among the image denoising approaches that preserve the edges. Firstly, BLF uses a simple weighted average calculation. Secondly, BLF is a local and non-iterative approach, requiring lower computational costs as compared to other iterative methods [180,181] and global methods of edge-preserving [185]. Third, when reducing noise, BLF has been shown to preserve the sharp edges of the image. The BLF has been used for a variety of tasks, including enhancement of image [186], artistic rendering [187], editing of image [188], feature recognition [189], optical flow estimation [190,191], medical image denoising [192,193], and retinal layer segmentation of 3-D OCT [194].

5.2. Contrast enhancement

Contrast enhancement techniques classify contrast within an image [195] as the perceived brightness or color differences. Soomro et al. [196] proposed a new vessel enhancement method based on a morphological operation, the stationary wavelet transform-based on threshold and CLAHE. Experimental results are based on three retina images and FFA images databases. The experimental results show significantly better results than the FFA photos. The contrast enhancement factor of the retina and FFA images was calculated to assess performance. The results reveal that the proposed method of image enhancement outperforms both non-invasive and invasive methods of image enhancement. Average contrast enhancement factor of 5.63 for retina images and 5.57 for FFA images is achieved. Contrast enhancement approaches can typically be categorized into different groups, such as Histogram-based, Transformation-based, Masking-based, and Filter-based [197,198]. A brief comparison of the different histogram-based contrast enhancement methods such as Histogram Equalization (HE), Adaptive Histogram Equalization (AHE), CLAHE, Rayleigh CLAHE, Non-Uniform Sampling, Vessel Enhancement Using Multi-dictionary and Sparse Coding (VE-MSC) are presented in Table 1 and explained as follows:

5.2.1. Histogram equalization

AHE is one of the low computation, contrast enhancement methods. This method enhances the image appearance by uniformly distributing the pixel intensity values (i.e. a flat histogram) but in order to obtain a perfect image, it is essential to have equal pixel numbers in all gray levels. Therefore, in all gray levels it becomes necessary not only to have a uniform distribution, but also to have equal number of pixel [226,227]. It is one of the simplest and easiest methods for enhancing the contrast of images. HE is therefore not a suitable technique for retinal images due to its high intensity noise and the absence of certain levels of brightness even after the enhancement process is performed. It yields strong results in ordinary images such as portraits of humans or natural images [228,229]. HE provides the slight improvement on the retinal image component i.e. blood vessel.

5.2.2. Adaptive histogram equalization

AHE is based on HE. This method develops each sub-image histogram for redistributing the images' brightness value [228]. Although AHE works on the entire image but it offers less improvement. Unlike HE, AHE improves the local contrast of blood vessels in a retinal image. Therefore AHE shares more information than HE [226].

5.2.3. Contrast limited adaptive histogram equalization

CLAHE [230] is developed from the AHE method. AHE showed amplifying noise in some of the homogeneous regions for the enhancement of retinal vessels, so CLAHE was proposed to eliminate this problem. CLAHE splits the input image into three channels RGB. CLAHE is only conducted in the G channel because this channel provides essential structural knowledge about the blood vessels. It thus obtains an improved G channel. Finally R, enhanced G, B channels are combined together to create an enhanced retinal image [231]. It is not easy to remove vessels automatically from retinal images due to blurred borders of retinal vessels with low contrast and strong noise arising from the resultant image. In R channel, there is more noise in the image from the visual observation than input image. In B channel, image quality tends to be low compared with the original. Structural image information in the G channel provides more contrast than the original.

5.2.4. Rayleigh contrast limited adaptive histogram equalization

The intensity channel of the image was enhanced by the Rayleigh transformation in Rayleigh CLAHE [228]. In CLAHE, the contrast of the image is improved but the chromatic information is not preserved. A good contrast of blood vessels is maintained in Rayleigh CLAHE and also preserves chromatic information in retinal image. Thus the overall appearance of the image improves.

Table 1

Comparison of the contrast enhancement methods.

S no.	Contrast enhancement method	Key features	Conclusions
1	Histogram equalization	Retina image color enhancement	Advantages: Simple and low computations. Disadvantages: High noise. Brightness levels absence. Local contrast improvement. Brings out more details. Noise amplification.
2	Adaptive histogram equalization	Image enhancement, noise and brightness	Advantages: Local contrast improvement. Disadvantages: Brings out more details. Noise amplification.
3	Contrast limited adaptive histogram equalization	Retina image color contrast enhancement	Advantages: Produce more contrast in G channel than R and B channel of color image. Disadvantages: Chromatic information of the color image is not preserved.
4	Rayleigh contrast limited adaptive histogram equalization	Diabetic Retinopathy in retina images	Advantages: Chromatic information of the color image is preserved. Disadvantages: Overall appearance is improved. Suffer from non-uniform illumination. Normalized correction factor in color planes i.e R, G, B planes.
5	Non-uniform sampling	Retina image color enhancement	Advantages: Non-uniform illumination correction. Disadvantages: Shift in color content is minimal. No new artifacts.
6	Vessel enhancement using multi-dictionary and sparse coding	Blood vessel enhancement and multi-dictionary sparse coding	Advantages: Vascular structure details are missing. Disadvantages: Improves the contrast effectively. More vascular structure details. Other enhancement problems are extended.

5.2.5. Gray level transformation

Enhancement of retinal image by gray level transformation provides better contrast and a more detailed image. The transformation function of gray level transformation has been given (8).

$$s = T(r), \quad (8)$$

where r is the input image pixel and s is the output image pixel. T is the transformation function that maps each value of r to each value of s . There are three basic gray level transformation that can be used for contrast enhancement i.e. linear, logarithmic and power-law graylevel transformation. For global polynomial contrast enhancement, Walter et al. [232] developed a polynomial gray level transformation operator and applied it locally to the G channel of retinal images.

5.2.6. Non uniform sampling

This approach is based upon blood vessels structures and imaging conditions of an image. Non-uniform illumination is present in majority of retinal images. Non-uniform sampling methodology employs estimation of the degradation components to find the correction factor. When applied on all three (R, G, and B) planes, the normalized correction factor successfully improved the contrast for non-uniform illumination. It thus improves the overall contrast and gives the color content a nominal shift. There were no new artifacts introduced [233].

5.2.7. Vessel enhancement using multi-dictionary and sparse coding

In this procedure, two dictionaries are created: one is the Representation Dictionary (RD), and the other is the Enhanced Dictionary (ED). Patches in RD and ED are picked using information images to optimize the multi-dictionary. The gray level image is represented by RD, and ED represents the label image in order to obtain the sparse coefficients by using a sparse coding method. The patches are extracted from G channel only. This approach boosts the image's contrast while also enhancing the vascular retinal anatomy. Therefore, it provides more information on retinal images [197].

5.3. Illumination correction

In this section different methods are described for non-uniform illumination and shade correction. Common methods for non-uniform illumination and shade correction has been categorized into filtering-based methods [234,235], segmentation-based methods [236], surface fitting-based methods [237] etc. Filtering-based methods assume that shading

components of distorted image can be approximated using a low-pass filter. Surface fitting approach assumes that a shading model can be fitted to estimate the intensity variations in the background [238]. A second-order polynomial is generally used as the model's function for the least-squares fitting. The segmentation-based approach repeatedly performs field fitting and image segmentation [236]. Histogram equalization [239], gamut mapping and gamma correction [240], and Retinex approach [241,242] are some of the more widely used illumination correction methods. Each of these methods has their advantages and disadvantages [243]. This study focuses on filtering-based methods that are usually considered to be basic, but effective [244]. Niemann et al. [245], proposed a fast and simple way for obtaining a low-pass correction coefficient in retinal images using the large-kernel median filter. Narasimha-Iyer et al. [246] suggested a technique of illumination correction that combines the benefits of filtering and surface fitting. The method also makes use of and exploits information specific to the retina. Foracchia et al. [247], proposed a system for automatic retinal image luminosity and uniformity of contrast. The approach calculates the luminosity and contrast fluctuation in the image's backdrop. With multiplicative image generation, Leahy et al. [248], developed a model of illumination correction and Laplace interpolation of retinal images. The sparsity property of image gradient distribution was employed by Zheng et al. [249], to adjust the illumination of fundus images. In retinal image analysis, the majority of illumination correction approaches use only the G-channel of color image. Only a few methods perform illumination correction on color image. Grisan et al. [243], proposed a model-based technique to perform illumination correction of the fundus images. The approach uses color space for hue, saturation, and value (HSV) to separate the luminance and chromatic details. Then, it connects an illumination model on the appropriate sub-region of the saturation and value channels. The approach adapted in Kolar et al. [244] depends on the illumination surface by using B-spline approximation for illumination correction. Varnousfaderani et al. [250] employed LUV color space transformation and a reference image for illumination correction.

6. Retinal image databases and performance measures

In this section we provide an overview of the datasets and performance measures widely used for the research on retina image analysis. Table 2 presents the publicly/privately available datasets, normal and diseased images, image resolution, tasks, ground truth information and the availability for each dataset.

Table 2
Datasets for retina image analysis.

S no	Database	Resolution	No of images			Task	Ground truth information	Availability
			Normal	Disease	Total			
1	DRIVE [199]	32	8	40	584 × 565	Vessel extraction		Online
2	STARE [200]			402	605 × 700	Vessel extraction, Optic Nerve, 13 retinal diseases		Online
3	HRF [201]	30	15	45	3504 × 2336	Vessel extraction, Optic Disk, Optical cup	Segmentation masks of field of view (FoV), blood vessels and OD classification labels of normal, DR and glaucomatous	Online
4	CHASE-DB1 [202]			28	1280 × 960	Vessel extraction		Online
5	Glaucoma_DB [203]	52	48	100	1504 × 1000	Optical disk, Optical cup, Cup-to-disk ratio (CDR)		Online
6	RIM-ONE [204]	92	39	131		Optical disk, Optical cup	Manual segmentation masks of OD Classification labels of normal and glaucomatous	Online
7	DRISHTI-GS [205]	31	70	101	2896 × 1944	Optical disk/Optical cup segmentation	Manual segmentation masks of optic nerve head for 50 training images classification labels of normal and glaucomatous	Online
8	ImageRet [206]	115	104	219	1500 × 1152	Vessel extraction		Online
9	MESSIDOR [207]			1200	1440 × 960, 2240 × 1488, 2304 × 1536	DR grading, Risk of DME		Online
10	SCES [208]	1630	46	1676		Optical disk, Optical cup, Cup-to-disk ratio (CDR)	Classification labels of normal and glaucomatous	Private
11	ORIGA [209]	482	168	650	720 × 576	Optical disk, Optical cup, Cup-to-disk ratio (CDR)	Segmentation masks of OD and OC Classification labels of normal and glaucomatous	Online
12	REFUGE [210]	1080	120	1200	2124 × 2056	Glaucoma detection	Pixel-wise annotations of OD and OC Localization masks of Fovea classification labels of normal and glaucomatous	Online
13	E-Ophtha [211]	266	195	461	1440 × 960, 2544 × 1696	Exudates detection, MA small HM detection		Online
14	HEI-MD [212]							
15	IDRID [213]							
16	Kaggle [214]			80,000		No DR, Mild DR, Moderate DR, Severe DR, PDR		Online
17	VICAVR [215]			58	768 × 584	Artery/Vein ratio		Online
18	REVIEW [216]			16	1360 × 1024, 2160 × 1440, 3300 × 2600, 3584 × 2438	Vessel extraction		Online
19	ROC Micro-Aneurysm [217]			100	768 × 576, 1058 × 1061, 1389 × 1383	Micro-aneurysm Detection		Online
20	ARIA [218]	16	151	167	767 × 576	OD, Fovea Location, Vessel extraction		Online
21	LMD [219]	218	34	252	768 × 584, 1920 × 1920	Laser mark segmentation		Online
22	ARED [220]							
23	DRIONS-DB [221]			110	600 × 400	Optical disk/Optical cup segmentation		Online
24	SEED [222]	192	43	235	3504 × 2336	Optical disk/Optical cup segmentation		Online
25	ACRIMA [223]	309	396	705		Optical disk/Optical cup segmentation	Classification labels of normal and glaucomatous	Online
26	SiMES [224]	482	168	650		Optical disk/Optical cup segmentation	Classification labels of normal and glaucomatous	Private
27	SiNDI [225]	5670	113	5783		Optical disk/Optical cup segmentation	Classification labels of normal and glaucomatous	Private

6.1. Retinal image databases

A number of fundus databases that are developed by different scientific communities to encourage researchers are publicly available. The diversification of fundus databases depends on a wide range of factors, including the use of the Fundus camera in the acquisition of images, image sizes, resolution, bit depth in per pixels, compression format, View Field (FOV), light illumination, total number of images in the particular database, ground truth results for comparison, disease information per subjects (details of diagnoses code) and whether raw data or any enhancement algorithms applied before public access.

Table 3 shows the different publicly available databases that are used in different features analysis.

6.1.1. DRIVE

DRIVE [199] consists of 40 color fundus images with a 45° FOV and an 8 bits per channel resolution of 565 × 584 pixels (seven of which include disease). The dataset consists of a training and a test set of 20 images. For the test set there are two different manual annotations, and on the training set there is only an annotation per image available.

Table 3
Publicly available databases used in different features.

Database	Retina image features						
	Blood vessel	OD/OC	Exudates	Hemorrhages	Macular edema	Laser scars	AV nicking
DRIVE [199]	✓	✓	✓				✓
STARE [200]	✓		✓	✓	✓		
HRF [201]	✓	✓					
CHASE-DB [202]	✓						
Glaucoma_DB [203]		✓					
RIM-ONE [204]		✓					
DRISHTI-GS [205]		✓					
ImageRet [206]	✓		✓	✓	✓		
MESSIDOR [207]	✓	✓	✓	✓	✓		
SCES [208]		✓					
ORIGA [209]		✓					
REFUGE [210]		✓					
E-Ophtha [211]			✓				
HEI-MD [212]			✓		✓		
IDRID [213]	✓	✓		✓	✓		
Kaggle [214]				✓			
VICAVR [215]							✓
REVIEW [216]	✓						
ROC Micro-Aneurysm [217]				✓			
ARIA [218]	✓	✓			✓		
LMD [219]							✓
ARED [220]					✓		
DRIONS-DB [221]		✓					
SEED [222]	✓	✓			✓		
ACRIMA [223]		✓					
SiMES [224]		✓					
SiNDI [225]		✓					

6.1.2. STARE

The National Institutes of Health (NIH) U.S. have funded a structured retina analysis (STARE) [200] program. It contains retina images showing 13 human eye-related diseases. It contains the list for each image of disease codes and names. The pixel level annotation is available for blood vessels and the optic nerve. All images were divided by two observers manually. On average, 32,200 pixels were labeled as vessel by the first person and 46,100 pixels were labeled as vessel by the second person. Due to retinal diseases presence this dataset offers a difficult OD detection problem.

6.1.3. HRF

The HRF [201] dataset includes 15 healthy patient images, 15 diabetic retinopathy and 15 glaucoma patient images. Images with 60° FOV and 3304 × 2336 pixel resolution have been captured. A group of experts is available for segmentation of the ground truth per image.

6.1.4. CHASE

CHASE has been gathered from kids of various ethnic backgrounds and children aged 9 to 10 years in England's Children's Heart and Health Study (CHASE) [202]. It comprises the ground truth for the blood vessels gathered with the Top Con TRV-50 35° FOV camera and consists of 28 retinal fundus photos from 14 youngsters. This dataset's photos have a non-uniform background illumination, low contrast, and larger arteries with a bright central band known as the central vessel reflex.

6.1.5. RIM-ONE

The Retinal Image Database of Optic Nerve Assessment (RIM-ONE) [204] was created for glaucoma diagnosis and consists of 169 optic nerve head areas manually clipped from complete retinal fundus images recorded by the body of a Canon EOS 5D Mark II camera with a non-mydiatic Nidek AFC-210 lens. Those images have been annotated by 5 experts: 1 optometrist and 4 ophthalmologists.

6.1.6. ORIGA

The online retinal fundus image database (ORIGA) [209] is an online collection of fundus images and ground truths that researchers can use to discuss the results of retinal image analysis and diagnosis. From 2004 to 2007, it was collected at the Singapore Eye Research Institute.

6.1.7. DRISHTI-GS

DRISHTI-GS [205] is a collection of 101 fundus photos taken at India's Aravind eye hospital of healthy and glaucoma patients with a nearly 25° FOV. The dataset is divided into two parts: training and testing, with 50 and 51 photos in each. Four ophthalmologists with 3, 5, 9, and 20 years of clinical experience each annotated all of the photos. The OD and OC boundaries were manually segmented, and CDR was used as ground truths.

6.1.8. Glaucoma DB

Glaucoma DB [203] consisting of 100 labeled images annotated with clinical CDR (CCDR) by ophthalmologists, using it as a benchmark for the measured CDR values. Dataset consists of 52 healthy and 48 glaucoma images captured using a 1504 × 1000 resolution Top Con TRC 50EX camera.

6.1.9. ImageRet

In 2008 ImageRet [206] project was launched by the FinnWell Diabetic Retinopathy Technology (DR). The ImageRet include 219 retina images, divided into two datasets i.e. DIARETDB0 and DIARETDB1, respectively. DIARETDB0 set contains 130 images (110 Normal, 20 DR affected) whereas the DIARETDB1 contains 89 images in which 5 normal images and 84 affected images. These retina images were captured at a FoV of 50° with fundus camera and 1500 × 1152 resolution in PNG format.

6.1.10. MESSIDOR

MESSIDOR [207] is the French ministry of research and Defense's project to perform comparative studies on the various segmentation technique for retinal images [251]. It is the largest dataset that contains 1200 retinal images, captured using non-mydiatic Topcon TRC NW6

with 8 bit per color channel resolution including 2304×1536 , 2240×1488 and 1440×936 pixels. 400 retinal images of this dataset were obtained without pupil dilation and the remaining were obtained with the dilation. The experts suggested two diagnoses for each image in the dataset i.e., the possibility of macular edema and retinopathy.

6.1.11. SCES

One senior professional grader and one retinal expert evaluated data from 1060 Chinese participants in the Singapore Chinese eye study (SCES) [208]. The purpose of this study was to classify anterior chamber depth determinants (ACD) and establish their relative importance in Chinese people.

6.1.12. REFUGE

Retinal Fundus Glaucoma Challenge (REFUGE) part was made available as the REFUGE dataset [210]. The training data consists of 400 images centered at the rear pole with both optic disk and macula, captured using Zeiss Visucam 500 camera with a resolution of 2124×2056 .

6.1.13. E-ophtha

E-ophtha [211] was launched by French research agency as a funded project. It provides the locations for MAs and EXs, which two ophthalmologists have identified. The first ophthalmologist highlighted the locations which the second ophthalmologist verified and examined. The database is divided into two datasets: an e-ophtha MA and an eophtha EX. There are 47 photographs in the EX collection, 12,278 EXs, and 35 healthy images. Several healthy images, such as reflections and optical remnants, include structures that can be easily modified using EX detection techniques. The e-ophtha MA, on the other hand, has 148 images, 1306 MAs, and 233 healthy images.

6.1.14. Kaggle

EyePACS clinics offered Kaggle [214], which contains a significant collection of high-resolution retinal photographs taken under diverse situations. The image level annotation was sent to Expert ophthalmologists, and each image was given a DR grade on a scale of 0 to 4 as follows: 0 indicates no risk, 1 indicates mild, 2 indicates moderate, 3 indicates severe, and 4 indicates PDR.

6.1.15. VICAVR

The VICAVR [215] contains 58 retinal images. The dataset was used to measure the ratio of artery/vein. The retinal images were obtained from a non-mydiatic NW-100 TopCon camera with centered optic disk and resolution of 768×584 pixels. It includes vessel descriptions as well as the kind of vessel (A/V ratio) recorded at various radii from the optic disk. Three experts observed the details of ground truth.

6.1.16. REVIEW

retinal vessel images for width estimation (REVIEW) [216] is the reference database for retinal vessels, that consist of 16 mydriatic images with 193 vessel segments. It was created in 2008 by the University of Lincoln, UK. Three experts used a special drawing tool to mark the edges of the vessels. It was mainly divided into four groups, i.e. central reflex light images, high-resolution images, kick-point images and vascular disease images with 2, 8, 2, and 4 images respectively.

6.1.17. ROC micro-aneurysm

Retinopathy Online Challenge (ROC) for micro-aneurysm detection [217] took place in 2009 at the University of Iowa. For ROC a dataset with 100 images built that was divided into two groups, i.e. testing and training sets each of 50 images. In the training set, there is the gold standard used for representing the locations of micro-aneurysm. The images are captured through TopCon NW100 and Canon CR5-45NM fundus camera in a 45° FoV, with the resolution of 1058×1061 , 1389×1383 and 768×576 in JPEG format.

6.1.18. ARIA

The University of Liverpool's cooperation with the Royal Liverpool University Hospital Trust, UK, captured the ARIA [218] dataset in 2006. It also contains three more g subsets of images: 59 diabetes images, 61 control group images, and 92 age-related muscle degeneration images. The images were captured with a Zeiss FF450 fundus camera with a 50° FOV, 8 bit per color plane, and a resolution of 768×576 pixels, and saved in TIFF format. The ground truth descriptions of the location of the vessel, the fovea, and the optic disk were marked by two observers.

6.1.19. ARED

NEI created the Age-related Study on Eye Disease (AREDS) [220]. This is a multicenter, retrospective study with 595 patients aged 55 to 80 years old, intending to evaluate the clinical course of both AMD and cataracts. Participants could have any sickness or condition that would develop over time. Based on fundus images rated by ophthalmologic evaluations, a central read center, and best-corrected visual acuity, participants were assigned to one of five AMD categories.

6.1.20. DRIONS-DB

Digital retinal images were collected for the optic nerve segmentation database (DRIONS-DB) [221] by a university hospital in Spain. It was designed to segment the optic nerve head and the diseases that go with it. It was recognized by two separate medical specialists. The head of the optic nerve was used to create the images, which were then saved in slide format.

6.1.21. SEED

The Singapore epidemiology of eye diseases (SEED) dataset included 235 retina fundus images focusing on the study of major eye diseases such as DR, AMD, glaucoma, refractive errors, and cataracts [222]. OD and OC regions were marked as ground truth for segmentation by a trained grader in each image.

6.1.22. IDRiD

The Indian Diabetic Retinopathy Image Dataset (IDRiD) [213] is the first representative database of the Indian population. Furthermore, it is the only dataset that includes both normal retinal and diabetic retinopathy lesions structures at the pixel level. The data is split into three sections. There are 81 color fundus images in the segmentation section, which were divided into a train and test set and saved in JPG format. The dataset for optical disks, hemorrhages, exudates (hard and soft) and microaneurysms, was segmented into train and test sets and saved in TIF format for ground truth images. It contains 516 photographs in the illness grading section, which are divided into a train set of 413 photographs and a test set of 103 photographs and encoded in JPG format. Ground truth photos with DR and DME labels are separated into train and test sets and saved in CSV format. The localization section contains 516 photographs, divided into a training set of 413 photographs and a testing set of 103 photographs, all in JPG format. Ground truth images are separated into training and testing sets and saved in CSV format for the center location of the optic disk and fovea.

6.1.23. HEI-MED

The Macular Edema Dataset (HEI-MED) [212] is a collection of retinal fundus images used to train and evaluate image processing algorithms for detecting exudates and diabetic macular edema. The collection contains 169 Jpeg images compressed to the highest quality, with all photographs of sufficient quality, no duplicate patients, and a decent mix of nationalities and illness stratifications represented.

6.1.24. Laser Mark Dataset (LMD)

LMD [219] is a database which permits comparative studies of laser mark segmentation in retinal images. The LMD is divided into two different image groups: one where the images were acquired during a DR Screening LMD-DRS and the other where the images were captured in a clinical environment LMD-BAPT. The LMD-DRS contains 203 retinal images manually identified by experts as having laser scars from an ongoing DR screening program. All the images are non-mydiatic and have a FOV of $45 \times 45^\circ$ and they were obtained in 2014. 26 images are obtained using Nidek AFC-330 Retinal Camera and 1920×1920 pixel resolution. The remaining 177 images were obtained using Canon CR6-45NM Retinal Camera and have a 768×584 pixel resolution. The LMD-BAPT comprises 34 laser marked and 15 without laser marked images. This dataset is composed of 9 patients with retinal images. Each patient contains images of the retinal fundus from before and after the treatment of photo-coagulation. In their filenames the images with the letter "A" are labeled as "Laser" and in their filenames the images with the letter "B" are labeled as "No Laser".

6.1.25. ACRIMA

There are 705 fundus images in the ACRIMA database (396 glaucomatous and 309 normal images) [223]. They were gathered as part of the ACRIMA project with the consent of glaucomatous and normal patients, and in compliance with the ethical principles put out in the 1964 Declaration of Helsinki. All of the patients were chosen by experts based on their criteria and clinical results throughout the assessment. The eyes were dilated and centered in the optic disk for the bulk of the fundus photos in this collection. Some of them were deleted due to distortions, noise, and low contrast. These photos with a field of view of 35° were captured using the Topcon TRC retinal camera and the IMAGEnet® capture system. All photos from the ACRIMA database were annotated by two glaucoma experts with a combined 8 years of expertise. No further clinical information was considered while categorizing the photos. The first version of the ACRIMA database could only be used for classification tasks. The optic disk and the optic cup cannot be segmented.

6.1.26. Simes

The Singapore Malay Eye Study (SiMES) [224] aims to provide population-based data on the prevalence and risk factors of visual impairment and significant sight-threatening eye diseases in a Singaporean adult Malay population. The SiMES also allows for comparisons with other Asian studies, especially data from the TPS, which focused at a similar-aged Chinese population in Singapore.

6.1.27. Sind

The Singapore Indian Eye Study (SiNDI) [225] was a cross-sectional, population-based study that enrolled 3400 Indians aged 40 to 83 in Singapore. Ocular components such as an anterior chamber depth (ACD), an axial length (AL), and a corneal radius were measured using partial coherence interferometry (CR). It was determined what the spherical equivalent of refraction was (SE). Indians in Singapore had an AL that was comparable to Malays in Singapore, but it was longer than Indians in India. The strongest determinants of AL were time spent reading, height, and educational level. In all age classes, AL was the best predictor of SE.

7. Feature extraction/segmentation

Various methods and techniques are available for retinal image analysis based on different features, e.g. blood vessels, optical disk/optical cups, exudates, haemorrhages, macular edema, laser scars, and arteriovenous (AV) nicking. Such techniques are further divided into two methods that include supervised methods and the unsupervised methods. Flow diagram of the retina image analysis section is shown in Fig. 7.

7.1. Blood vessels

The segmentation of retinal blood vessels can be done using a variety of techniques and procedures. Unsupervised methods and supervised methods are the two types of procedures that are commonly used. A thorough examination of different unsupervised and supervised blood vessel segmentation approaches is presented. In Tables 4 and 5, the performance metrics of the supervised and unsupervised methods for their evaluation criteria, database, and year of publication are given, respectively. Fig. 8 illustrate the chronological summary of the recent blood vessels segmentation methods.

7.1.1. Unsupervised methods

The unsupervised approach uses no prior knowledge, such as ground truth images, to find blood vessel's hidden patterns in a retinal image and recognize the pixel as a vessel. This is also used to cluster data. This section categorizes the unsupervised methods into three groups: Filtering-based Techniques, Multi-scale Line Detector-based Techniques, and Other Techniques.

A. Filtering-based techniques. For the detection of blood vessels in retinal images, a 2-D matching filter has been proposed. The vessels were enhanced using CLAHE [252]. The filter LoG (Gaussian Laplacian) was avoided to reduce misclassification of the non-vasculature. The blood vessels were segmented using LoG and MF inherent property. The proposed method was tested on the databases HRF, DRIVE, and STARE. The method has the advantages of simple implementation, less processing time, efficiency, and effective extraction of blood vessels regardless of the retina's pathological condition. Dharmawan et al. [255] proposed a new 2D matching filter with an improved Chebyshev Type-I function for retinal blood vessel segmentation. The Gaussian probability substitutes the standard MF in the innovative strategy. The CLAHE was utilized to increase the vessel contrast. The background was normalized by substituting the background pixel for the lesion pixel. For the detection of photos with low noise vessels, postprocessing techniques were used. The findings were tested using the DRIVE and the STARE databases. Gao et al. [256] used the U-net, a fully convolutional neural network, and a gaussian matched filter to create a hybrid technique for segmentation prediction of blood vessels. The narrow vessels were strengthened with a matching gaussian filter, and the U-net was used for end-to-end automatic retinal blood vessel segmentation. On the DRIVE dataset, the proposed technique achieves an accuracy of 96.36%. Elson et al. [257] employed a Multi-Scale Matched Filter (MSMF) approach for automatic vessel extraction. Blood vessels were extracted using an MSMF derived from Social Group Optimization (SGO). The proposed technique was evaluated using the STARE and the DRIVE datasets, which are widely used. For increased accuracy, the MSMF optimum filter settings were reached. The MSMF, which is based on SGO, has yielded considerable results in vessel extraction. The commonly used datasets the STARE and DRIVE were used for the evaluation of the proposed method. The MSMF optimum filter values were achieved for improved accuracy. The SGO-based MSMF has revealed significant outcomes in vessel extraction. Aguirre-Ramos et al. [21], have created a new technique for recognizing blood vessels in retinal images. After removing noise from the RGB image's G-channel with a Low-Pass Radius Filter, a 30-element Gabor filter and a Gaussian fractional derivative are used to drastically improve the outlines and the structure of the blood vessels. A threshold and a set of morphology-based decision criteria are then used to separate the blood vessels and limit the number of false positive pixels. The proposed method may also be used to detect and retrieve the original optic disk image. In the context of an unsupervised Frangi filter-based retinal vascular segmentation technique, Khawaja et al. [161], proposed using the state-of-the-art Probabilistic Patch-Based (PPB) denoiser. When dealing with amplified noise, the PPB denoiser aids in maintaining vessel structure. Individual segmentation and linear binarized output recombination are

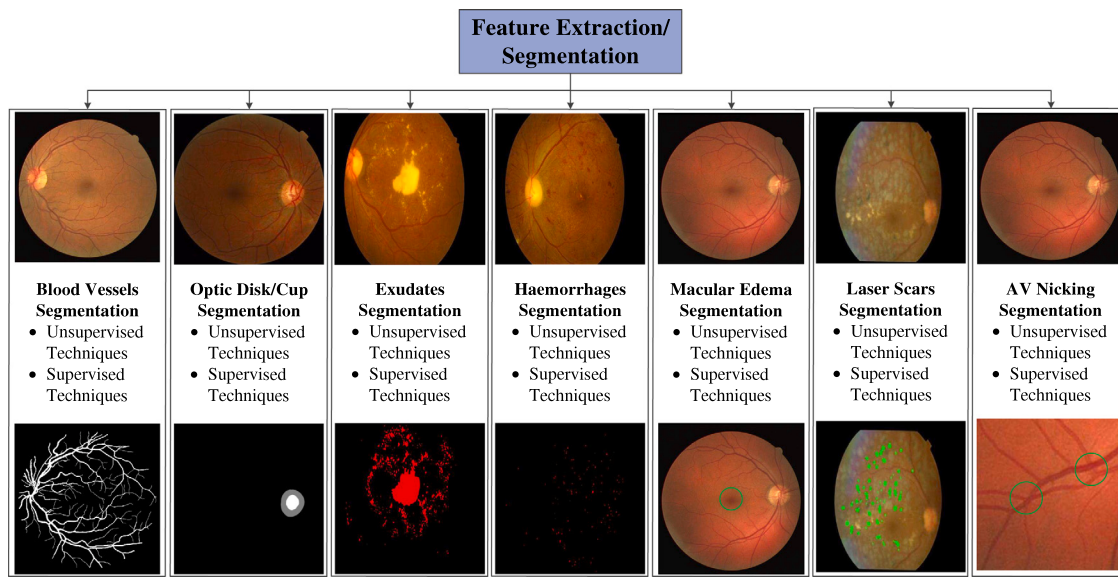


Fig. 7. Flow of Retina Features Segmentation Section.

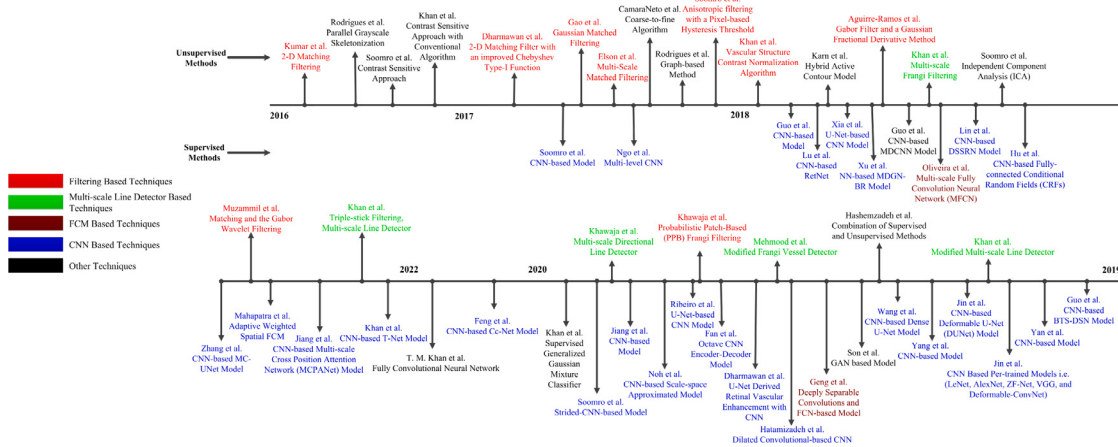


Fig. 8. Chronological summary of the recent blood vessels segmentation methods.

performed after the modified Frangi filter is evaluated independently for small and large vessels. In this method, authors have demonstrated that Frangi Filter's performance has been greatly improved. The suggested approach's performance is assessed using two well-known open-access datasets, namely the DRIVE and the STARE. The proposed technique outperforms both the Generalized Linear Model modes of preprocessing (GLM) and the Contrast Limited Adaptive Histogram Equalization (CLAHE). The outputs of CLAHE on the DRIVE and the STARE datasets are ($\text{Acc} = 95.61\%$, $\text{Sn} = 80.27\%$) and ($\text{Acc} = 95.61\%$, $\text{Sn} = 79.80\%$), respectively. For GLM it is shown to be ($\text{Acc} = 96.03\%$, $\text{Sn} = 79.07\%$) and ($\text{Acc} = 95.83\%$, $\text{Sn} = 78.60\%$) respectively over the DRIVE and The STARE datasets. Muzammil et al. [269] presented an unsupervised approach for segmenting vessels from retinal images. The proposed method consists of several steps. To begin, the G-channel is recovered from the colored retinal image and pre-processed using Contrast Limited Histogram Equalization and Fuzzy Histogram-based Equalization for contrast augmentation. Top-hat morphological operations are employed to expel geometrical objects (macula, optic disk) and noise. The matching filter and the Gabor wavelet filter are applied to the resulting enhanced image, and the outputs from both are combined to extract vessel pixels. The resulting image, which now includes a visible blood artery, is binarized using the human visual system (HVS). Post-processing produces a final image of a segmented

blood vessel. The proposed method achieved an average sensitivity, specificity and accuracy of 72.71%, 97.98% and 95.73% on DRIVE database and 71.64%, 97.60%, and 95.60% on STARE database, respectively. Based on an upgraded Frangi filter and adaptive weighted spatial FCM, Mahapatra et al. [270] proposed a new framework for retinal vascular segmentation. The proposed method is based on getting the optimal parameters for the vesselness function using MELPSO. Because the vessels are linked components, incorporating spatial information during the clustering process increases segmentation performance even further.

B. Multi-scale line detector-based techniques. The multiscale methods are based on the information of the retinal blood vessel's variable width at various scales. The width of vessels decreases as they move away from the optic disk and increases as they move closer to it. Therefore, it is necessary to represent the vessels with a cross-section profile of Gaussian shape that is locally linear and piecewise connected. Khan et al. [262], presented a technique that consists of special parallel processes for extracting blood vessels and de-noising retinal images. The dissimilarity between the blood vessels and the context is improved using an adaptive histogram equalization technique. Morphological top-hat filters are used to remove the macula and optic disk, among other things. To reduce local noise, the difference between the top-hat filtered image and the high-boost filtered image is assessed. Frangi

Table 4

Performance Measures of Unsupervised Methods for Blood Vessel extraction: Year wise best results on different datasets are highlighted with different colors i.e.(Red color for DRIVE, Green color for STARE, Blue color for HRF, and Violet color for CHASE_DB).

Year	Author	Method	Dataset	Performance measures in (%)			
				Accuracy	Sensitivity	Specificity	AUC
2016	Kumar et al. [252]	2-D matching filtering	DRIVE	96.26	70.06	98.71	N.A
			STARE	96.37	76.75	97.99	N.A
			HRF	94.50	75.74	N.A	N.A
	Rodrigues et al. [253]	Parallel grayscale skeletonization	DRIVE	95.65	73.23	97.83	N.A
			STARE	95.68	66.99	97.97	N.A
	Soomro et al. [254]	Contrast sensitive approach	DRIVE	94.61	N.A	N.A	97.18
2017	Khan et al. [22]	Contrast sensitive approach with conventional algorithm	STARE	94.20	N.A	N.A	96.01
			DRIVE	95.01	73.73	96.70	N.A
			STARE	95.02	73.59	97.08	N.A
	Dharmawan et al. [255]	2-D matching filter with an improved Chebyshev Type-I function	DRIVE	95.40	75.60	97.30	N.A
	Gao et al. [256]	Gaussian matched filtering	STARE	95.30	73.10	97.20	N.A
	Elson et al. [257]	Multi-Scale matched filtering	DRIVE	96.36	78.02	98.76	97.72
2017	CamaraNeto et al. [32]	Coarse-to-fine Algorithm	DRIVE	96.57	72.21	97.75	N.A
	Rodrigues et al. [258]	Graph-based Method	DRIVE	87.87	79.42	96.31	N.A
			STARE	86.16	76.95	95.37	N.A
			DRIVE	94.65	71.65	98.01	N.A
			HRF	94.72	72.23	96.36	N.A
	Soomro et al. [259]	Anisotropic filtering with a Pixel-based Hysteresis Threshold	DRIVE	94.53	75.23	97.63	N.A
2018	Khan et al. [260]	Vascular structure contrast normalization algorithm	STARE	96.36	78.42	98.17	N.A
			DRIVE	94.40	75.40	96.40	N.A
			STARE	94.80	75.20	95.60	N.A
	Karn et al. [261]	Hybrid active contour model	DRIVE	97.00	78.00	98.00	88.00
			STARE	96.00	80.00	96.00	88.00
			CHASE_DB1	97.00	78.00	97.00	N.A
2018	Aguirre-Ramos et al. [21]	Gabor filter and a Gaussian fractional derivative method	VAMPIRE	96.00	79.00	97.00	88.00
			DRIVE	95.03	78.54	N.A	N.A
	Khan et al. [262]	Multi-scale Frangi filtering	STARE	92.31	71.16	94.54	N.A
			HRF	88.14	72.36	90.31	N.A
			DRIVE	95.80	73.00	97.93	N.A
	Soomro et al. [263]	Independent Component Analysis (ICA)	STARE	95.13	79.02	96.45	N.A
2019	Khan et al. [264]	Modified multi-scale line detector	HRF	95.23	74.52	95.84	N.A
			DRIVE	95.53	75.20	96.76	N.A
			STARE	96.70	78.60	98.20	N.A
	Hashemzadeh et al. [265]	Combination of supervised and unsupervised methods	DRIVE	95.06	76.96	96.51	N.A
			STARE	95.13	75.21	98.12	N.A
			CHASE_DB1	95.31	78.30	98.00	97.52
2019	Mehmood et al. [266]	Modified Frangi vessel detector	STARE	96.91	80.87	98.92	98.53
			CHASE_DB1	96.23	77.37	98.40	97.89
			DRIVE	95.30	73.70	97.60	N.A
			STARE	95.70	74.10	98.20	N.A
	Khawaja et al. [161]	Probabilistic Patch-Based (PPB) Frangi filtering	CHASE	95.61	80.27	97.33	N.A
			DRIVE	96.03	79.07	97.90	N.A
2022			GLM	95.61	79.80	97.32	N.A
			STARE	95.83	78.60	97.25	N.A
			DRIVE	95.53	80.43	97.30	N.A
	Khawaja et al. [267]	Multi-scale directional line detector	CHASE_DB1	95.28	79.74	96.97	N.A
			STARE	95.45	80.11	96.94	N.A
	Khan et al. [268]	Triple-stick filtering, Multi-scale line detector	DRIVE	96.10	81.25	97.73	N.A
	Muzammil et al. [269]	Matching and the Gabor wavelet filtering	STARE	95.86	80.78	97.21	N.A
			CHASE_DB1	95.78	80.12	97.30	N.A
			DRIVE	95.73	72.71	97.98	N.A
			STARE	95.60	71.64	97.60	N.A

filter is applied to enhance blood vessels with different widths at multiscale. Segmentation is achieved separately using modified Otsu thresholding on the high-boost filtered image and enhanced image by Frangi. A Vessel Location Map (VLM) is generated by the use of raster for vector transformation in the post processing stage. Post processing steps are used to remove incorrectly classified pixels of the vessels in a novel way. To get the final segmented image, a pixel-by-pixel AND operation is used between the Frangi and the VLM output images. Khan et al. [264], modified the multi-scale line detector to improve its sensitivity. To begin, the proposed method uses a variable window size with a line detector mask to detect tiny vessels. Second, external orientations are input into the multi-scale line detectors to align them with the direction of vessel flow. Thirdly, it recommends the best weights for weighted linear combinations of individual line-detector responses. Fourth, to find the connected vessel tree, a hysteresis threshold is used instead of using one global threshold. The

combined impact of these modifications is a major improvement in the ability of traditional multi-scale line detector system to eliminate noise, while locating more of the thin vessels. The proposed method achieves accuracy, sensitivity and specificity of 95.06%, 76.96% and 96.51% on DRIVE and 95.13%, 75.21% and 98.12% on STARE dataset respectively. Mehmood et al. [266] proposed a method for dividing the retinal image into three sub-parts: optical disk region, vessel region and non-vessel region (black section outside vessels). On these three regions in the HSV domain color image enhancement is then performed. The color image is then transformed to gray using a technique based on multi-scale line detection. A modified Frangi Vessel Detector is used for vessel detection. This filter generates an almost uniform response in any vascular structure and specifically boosts the boundary between the vascular structures and the background. This filter obtained the best result in quantitative metrics performance segmentation, signal-to-noise vessel enhancement ratio and response

Table 5

Performance Measures of Supervised Methods for Blood Vessel extraction: Year wise best results on different datasets are highlighted with different colors i.e., red color for DRIVE, green color for STARE, blue color for HRF, and violet color for CHASE_DB).

Year	Author	Method	Dataset	Performance measures in (%)			
				Accuracy	Sensitivity	Specificity	AUC
2017	Soomro et al. [260]	CNN-based model	DRIVE	94.70	74.60	91.70	83.10
	Ngo et al. [271]	Multi-level CNN	STARE	94.80	74.80	92.20	83.50
2018	Guo et al. [272]	CNN-based model	DRIVE	91.78	N.A	N.A	96.74
	Lu et al. [273]	CNN-based RetNet	DRIVE	95.59	78.12	98.14	97.90
	Xia et al. [274]	U-Net-based CNN Model	DRIVE	96.85	79.79	98.57	N.A
	Xu et al. [275]	NN-based MDGN-BR model	DRIVE	N.A	N.A	N.A	97.93
	Guo et al. [276]	CNN-based MDCNN model	HRF	N.A	N.A	N.A	97.70
	Lin et al. [277]	CNN-based DSSRN model	DRIVE	96.13	N.A	N.A	97.37
2019	Oliveira et al. [278]	Multi-scale Fully Convolution Neural Network (MFCN)	STARE	95.39	N.A	N.A	95.39
	Hu et al. [279]	CNN-based Fully-connected Conditional Random Fields (CRFs)	DRIVE	95.36	76.32	N.A	N.A
	Guo et al. [280]	CNN-based BTS-DSN model	STARE	96.03	74.23	N.A	N.A
	Yan et al. [281]	CNN-based model	CHASE_DB1	95.87	78.15	N.A	N.A
	Jin et al. [282]	CNN Based Per-trained Models i.e. (LeNet, AlexNet, ZF-Net, VGG, and Deformable-ConvNet)	DRIVE	95.76	N.A	N.A	98.21
	Jin et al. [283]	CNN-based Deformable U-Net (DUNet) model	STARE	96.90	N.A	N.A	99.05
2020	Yang et al. [284]	CNN-based model	CHASE_DB1	96.53	N.A	N.A	98.55
	Son et al. [285]	Generative Adversarial Network (GAN) based model	DRIVE	95.33	77.72	97.93	97.59
	Wang et al. [286]	CNN-based Dense U-Net model	STARE	96.32	75.43	98.14	97.51
	Geng et al. [287]	Deeply Separable Convolutions and FCN-based model	DRIVE	N.A	N.A	N.A	98.32
	Dharmawan et al. [288]	U-Net Derived Retinal Vascular Enhancement with CNN	STARE	95.66	N.A	N.A	98.02
	Hatamizadeh et al. [289]	Dilated Convolutional-based CNN	HRF	96.41	N.A	N.A	98.31
2021	Fan et al. [290]	Octave CNN Encoder-Decoder model	DRIVE	96.28	N.A	N.A	97.64
	Ribeiro et al. [291]	U-Net-based CNN Model	STARE	95.90	N.A	N.A	98.44
	Noh et al. [292]	CNN-based Scale-space Approximated model	CHASE_DB1	95.61	76.41	98.06	97.76
	Soomro et al. [293]	Strided-CNN-based model	DRIVE	96.10	N.A	N.A	98.02
	Jiang et al. [294]	CNN-based model	STARE	96.10	N.A	N.A	98.32
	Khan et al. [295]	Supervised Generalized Gaussian Mixture Classifier	CHASE_DB1	95.20	N.A	N.A	98.30
2022	Feng et al. [296]	CNN-based Cc-Net model	DRIVE	95.11	79.86	97.36	97.40
	T. M. Khan et al. [297]	Fully Convolutional Neural Network	STARE	95.38	79.14	97.22	97.04
	Khan et al. [45]	CNN-based T-Net Model	CHASE_DB1	95.30	N.A	N.A	98.31
	Jiang et al. [298]	CNN-based Multi-scale Cross Position Attention Network (MCPANet) model	DRIVE	95.69	81.97	98.19	N.A
	Mahapatra et al. [270]	Adaptive Weighted Spatial FCM	STARE	96.86	81.64	98.70	98.92
	Zhang et al. [299]	CNN-based MC-UNet model	CHASE_DB1	97.50	83.00	98.48	N.A

uniformity in vascular structures as compared to other filters. Experimental results show that modified Frangi method performance is much better than actual Frangi. The proposed method achieves sensitivity, specificity and accuracy of 73.7%, 97.6% and 95.3% on DRIVE and 74.1%, 98.2% and 95.7% on STARE dataset respectively. Khawaja et al. [267], suggested a multi-scale line detector directed vessel segmentation technique, with an emphasis on the tiniest, most difficult-to-segment vessels. Designing a directional line detector and employing it on images with just features directed along the detector direction considerably improves the technique's detection accuracy. The final step includes a directional binarization technique that aids in the achievement of greater performance improvements in terms of key indicators. The proposed method achieves a sensitivity of 80.43%, 80.11%, and 79.74% for the DRIVE, STARE, and CHASEDB1 datasets, respectively. Khan et al. [300] discussed how to improve the sensitivity of existing vascular segmentation algorithms by using contrast sensitive measurements. Low-contrast vessels are extracted using a vascular structure contrast normalization procedure, which is then used to bring them up to par with their high-contrast equivalent. The second measure is to capture vessels with a scale-normalized detector. Third, a method of flood-filled reconstruction is used to achieve binary output. The procedure requires seeding with suitably positioned seeds generated by the curvature of isophots, a contrast-sensitive detector. A binary fusion process of two different binary outputs due to two illumination variations correction mechanisms was applied in the earlier processing stages as the final sensitivity improvement measure. As a result, the capacity to reduce noise when identifying vessels with low contrast has improved. The proposed method achieves accuracy, sensitivity and specificity of 94.40%, 75.40% and 96.40% on DRIVE and 94.80%, 75.20% and 95.60% on STARE dataset respectively.

C. Other techniques. The characteristics of topological and morphological blood vessel extractor for automatic segmentation of vessel had discussed in [253]. Mathematical morphological operators used the parallel grayscale skeletonization method to obtain good segmentation results. The topological and morphological extractors were used for the extraction of blood vessel tree pixels and to discover the spatial properties of the blood vessel and its connectivity. The proposed technique accurately obtained the retinal blood vessel tree pixels by smoothing the boundaries of the vessel and removing spurious objects. The classifier was tested using the DRIVE and STARE dataset. Soomro et al. [254] discussed several contrast sensitive approaches and integrated them with traditional algorithms, thereby improving the sensitivity of a given technique for retinal vessel extraction. The proposed method delivers good performance with accurate vessel extraction. The proposed unsupervised method achieves an accuracy of 94.61%, 94.20% and AUC of 97.18%, 96.01% on DRIVE and STARE datasets, respectively. Khan et al. [22] also discussed several contrast-sensitive approaches that once used along with conventional algorithm results in improved sensitivity. These add-on modules have an average accuracy, sensitivity, and specificity of 95.01%, 73.66%, and 96.89%, respectively, when tested on publicly available databases like DRIVE and STARE.

CamaraNeto et al. [32] used a coarse-to-fine technique to develop an unsupervised algorithm for recognizing blood vessels in fundus images. For background homogeneity and noise reduction, the suggested technique uses a gaussian smoothing, a top-hat morphological operator, and the blood vessel contrast enhancement. To approximate the vessel map to an adaptive local thresholding approach, a spatial dependency and probability statistics are applied. The coarse segmentation is then adjusted to-pixel mislabeling and better estimate the retinal artery tree using morphological reconstruction and curvature analysis. Soomro et al. [301] used imaging techniques and pattern recognition strategies to survey the study of the current retinal fundus image. The authors investigated and examined existing automatic methods of DR (pixel-to-pixel) detection. The study found that a fully automatic DR grading

system is needed, which delivers correct findings for retinal image features such as diseases and blood vessels, after analyzing computer-aided methodologies for diabetic retinopathy diagnosis using retinal fundus images. The fully automatic method of detecting blood vessels are necessary for this purpose. In current approaches it is observed that the output of the existing algorithms declined because the tiny vessels with low contrast are not easily detected. The segmentation approach of retinal blood vessels for assessing DR or other eye disorders is not supposed to replace the disease diagnosis experts, but it reduces the workload of the retinal image processing, analyzes the disease progress rapidly, and suggests early care. There are numerous difficulties with retinal images, including non-uniform backdrop and background, noise, low contrast, fluctuating contrast, central light reflex, and diseases that make detecting small veins difficult. In this study, a new method based on wavelet transforms and mathematical morphology is presented by Rodrigues et al. [258] to detect optic disk, and explore the tubular characteristics of blood vessels to segment retinal arteries and veins. Both the optical disk and the vascular structure are milestones for image registration and are important for the analysis of retinal images. Author's used a genetic algorithm and its sequence of generations and crossovers instead of a manual try and error approach to find the best parameter for detecting blood vessels as precisely as possible. However, the technique of exploring the vessels tubular characteristics reaches its limits when the vessels are represented by winding lines of 1 pixel, often not continuous. To overcome this constraint, the author's implemented a graph-based method using Dijkstra's shortest path algorithm to map the segments by using a distribution statistical method to determine whether or not the segment marked is part of the vascular structure. Soomro et al. suggested a new segmentation approach to solve the problem of low sensitivity, including modules such as color-to-gray component analysis conversion, the scale normalization factors for improved detection in the tiny blood vessel, anisotropic filtering with an appropriate stop-principle and a pixel-based hysteresis threshold [259]. The impact of such supplementary measures was tested on publicly available databases such as DRIVE and STARE. In the DRIVE database, the sensitivity is increased from 73% to 75% while retaining 96.5% accuracy. Karn et al. [261], show how to segment the retinal blood vessel in diverse fundus images using a hybrid active contour model and a novel preprocessing technique. The contour-driven black top-hat transformation and phase-based binarization method were used to maintain the vessels' edge and corner details. The snake- and balloon-based gradient vector flow (GVF) methods are coupled in the proposed research to obtain better accuracy over various existing active contour models. In actual active contour models, the snake could not reach the closed curve, resulting in the loss of small blood vessels. To solve this challenge, a Finf (balloon) inflation term is paired with a GVF-based snake to achieve certain internal energy of the snake for successful blood vessel segmentation. For the quick and accurate segmentation of retina blood vessels, Soomro et al. [263] proposed an automated retinal vascular segmentation approach. Many retina diseases can be studied with such a technique. Many retina diseases can be studied with such a technique. The efficiency of the segmentation process is effected by the presence of changing low contrasts in a retinal fundus image. Independent Component Analysis (ICA) is a technique for removing noise that is divided into two frameworks: ICA1 and ICA2. On retinal color fundus images, both topologies were validated, and the author chose the one that delivers higher contrast values. The ICA2 architecture performed significantly better for the retinal fundus than the ICA1 architecture because it corrected for the low contrast value more effectively. The proposed method achieves an accuracy, sensitivity and specificity of 95.53%, 75.20% and 96.76% on DRIVE and 96.70%, 78.60% and 98.20% on STARE dataset respectively. Hashemzadeh et al. [265], developed a retinal blood vessel extraction method that combined supervised and unsupervised machine learning approaches with an acceptable collection of image features. In addition to the typical features employed in vessel extraction, three main features are

used, each of which has a considerable impact on vessel extraction accuracy. The proposed combination of many types of individually accurate features produces a rich local dataset with a superior vessel and non-vessel pixel discrimination. The proposed model initially extracts the thick and transparent vessels without supervision, then the thin vessels with supervision. The purpose of integrating supervised and unsupervised approaches is to address challenges such as significant intra-class variance in image characteristics computed from different pixels on the vessel.

7.1.2. Supervised methods

Supervised methods use extracted feature vectors, or labeled training data, to train a classifier to automatically identify retinal blood vessel. Based on the training dataset, such an algorithm must learn a set of vessel extraction criteria. In supervised methods, the labeled training dataset is critical because ophthalmologists obtain information regarding vessel segmentation directly from manually segmented images. As a result, in a single database test, the performance of supervised methods often outperforms that of unsupervised approaches.

A. FCM-based techniques. Oliveira et al. [278] proposed a novel retinal vessel segmentation approach that depends on the multiscale Fully Convolution Neural Network (FCN) with Stationary Wavelet Transform (SWT). The approach is designed to accommodate the varying width and orientation of the retinal vessel structure. In addition, through the SWT decomposition, new channels were added to the FCN. A rotation is used for discovering the information acquired during the training process for enhancement of the vessel segmentation for both the prediction and data augmentation. On the STARE, the DRIVE, and the CHASE DB1 datasets, the suggested approach achieved an average accuracy of 96.94%, 95.76%, 96.53%, and AUC of 99.05%, 98.21%, and 98.55%, respectively. The proposed strategy is feasible for intense workouts, inter-rater variability, and faster GPU deployment. Geng et al. [287], proposed a method for segmentation of retinal vessels based on the deeply separable convolution and FCN with channel weighting. The approach consists of three phases: the pre-processing of images, the segmentation of images, and the formation of a model. First, the color fundus image is extracted in the G-channel and the contrast is improved by using CLAHE and gamma correction. Second, to expand network training data, the enhanced image is separated into patches. Finally, instead of the traditional method of convolution, the proposed depth-sensitive separate convolution approach is used to maximize network width. The proposed method achieves an accuracy of 96.30%/96.20%, and an AUC of 98.31%/98.30%, on the DRIVE and the STARE databases, respectively. T. M. Khan et al. [297], proposed a fully convolutional neural network variant-based supervised deep learning approach. Current fully convolutional neural network-based entrants have the disadvantage of involving several configurable hyper-parameters and a longer end-to-end training duration due to their decoder structure. To improve the resolution of the feature map, the suggested method uses a skip-connections strategy that involves transferring indices obtained via max-pooling from the encoder stage to the decoder. This drastically reduces the number of configurable hyper-parameters needed, as well as the training and testing stages' computing cost. Furthermore, the suggested strategy eliminates both post-processing and pre-processing procedures. The retinal vascular segmentation approach is modeled as a semantic pixel-wise segmentation problem in the proposed method, bridging the semantic and medical image segmentation gap. The addition of an external skip-connection for conveying the remaining low-level semantic edge information to accurately recognize small vessels in retinal fundus images is a fundamental contribution of the proposed approach. On three publicly accessible significant fundus image datasets, the proposed scheme's performance is tested using the frequently accepted assessment criteria of the precision, sensitivity, accuracy, and Receiver Operating Characteristics curves. The proposed approach achieves a sensitivity, a specificity, an accuracy, and a ROC

performance of 82.52%, 84.40%, and 83.97%, 97.87%, 98.10%, and 97.92%, 96.49%, 97.22%, and 96.59%, and 97.80%, 98.30%, and 98.10%, respectively, based on the images in the DRIVE, CHASE DB1, and STARE datasets.

B. CNN-based encoder-decoder techniques. Fan et al. [302] verified the use of the auto de-noising encoder (DAE). The vessel segmentation was done using the deep neural network. The multi-level technique was established by using the back-propagation algorithm and DAEs. Proposed approach was tested on three datasets STARE, DRIVE, and CHASE DB1 and achieved accuracy 96.10%, 96.10%, 67.60%, sensitivity 72.30%, 78.10%, 97.00% and specificity 98.00%, 97.90%, 97.00%, respectively. Tuba et al. [303] proposed a block-based overlapping method with the classification of the support vector machine. In this method, chromaticity and discrete cosine transform (DCT) coefficients were used for the segmentation of the blood vessels. This overlapping block-based method was tested on the DRIVE database. The proposed algorithm achieves specificity, sensitivity, and accuracy of 67.49%, 97.73%, and 95.48%, respectively. This algorithm has the advantage of classifying large retinal vessels accurately, but is poor in classifying thinner vessels accurately. Feng et al. [304] presented a patch-based method for the segmentation of the retinal blood vessels by the fully convolutional neural network. The proposed method was used to increase the speed of the fully CNN architecture with a skip connection for CNN and the local entropy sampling. The proposed method achieved 98.39%, 87.36%, 87.36%, 97.92%, and 78.11% scores of specificity, accuracy, precision, AUC, and sensitivity, respectively on the DRIVE dataset. Soomro et al. [260], proposed a CNN-based tiny blood vessels detection method from a low contrast image. The network was pre-processed and post-processed to remove additional noise to increase sensitivity. In order to test the proposed method, DRIVE and STARE datasets were used for the evaluation of sensitivity and precision, and achieved 75.00%, 94.70% respectively. Song and Lee [305], presented a model based on a CNN with a pixel path. There were different convolution and up-sample layers in this process. A function vector has been developed and used to predict vessels pixels. The performance of the presented approach was evaluated on the DRIVE dataset and achieved a sensitivity, specificity, and precision of 75.00%, 97.90%, and 95.00%, respectively. This technique provides an advantage of measurement accuracy but does not include the entire information on spatial vessels. Ngo et al. [271], presented the multi-level neural network approach for the blood vessels segmentation. The blood vessels have been precisely assessed by the technique of maximal resizing. In this approach, the spatial dropout and dropout were merged on deep neural network for the better segmentation. The proposed method was evaluated on the DRIVE dataset and achieves 95.33% of the accuracy and an AUC of 97.52%. However, the proposed method cannot detect tiny vessels. Singh and Dasgupta [306] formulated the vessels segmenting tasks by integrating the characteristics of totally CNN and organized predictions. The proposed approach represented a multi-label inference problem which helped to identify neighboring pixel's dependencies used in vessel segmentation. The approach was evaluated on the DRIVE dataset with a 0.0001 learning rate, whereas the RMSprop approach was adjusted at 0.7. The proposed approach achieves 84.98%, 98.01%, 95.33%, 97.44%, and 76.91% scores of precision, specificity, accuracy, AUC, and sensitivity respectively.

Thangaraj et al. [307], proposed a novel neural network for the segmentation of retina vessels. 13-D feature vector is constructed which uses Hu moment invariants for better performance, the responses of the Gabor filter, the local pattern, the Frangi vessel measurement, and the GLCM gray-level co-occurrence matrix. The performance of the proposed model was evaluated on three publicly available databases and achieves an accuracy, sensitivity, specificity and AUC of 96.06%, 80.14%, 97.53% and 88.84% on DRIVE, 9435%, 83.39%, 95.36% and 89.38% on STARE and 94.68%, 62.88%, 97.28% and 79.71% on CHASE_DB1, respectively. Guo et al. [272], presented a CNN-based

method for the segmentation task of the retinal blood vessel. Two layers were used in the CNN method; one for pooling and convolution and one for loss and dropout. The proposed approach has achieved an accuracy of 91.80% and an AUC of 96.70% on the DRIVE database for the segmentation tasks of retinal vessels. Lu et al. [273] proposed a CNN-based decoder-encoder architecture (RetNet) for vessel segmentation. The encoder was used for the extraction of hierarchical features, and the decoder was used for restructuring the input in full size. Both skip connections were used for more extraction of contextual and semantical information and improve RetNet's localization and the classification without pre-post processing steps. The architecture is evaluated on publicly available dataset DRIVE and has achieved 98.14%, 78.12%, 95.59%, and 97.90% of specificity, sensitivity, accuracy, and AUC, respectively. For retinal vessel segmentation, a coarse-to-fine approach that depends on CNN (CTF-Net) was proposed by Xia et al. [274]. The proposed framework has a cascaded architecture, which is composed of many networks based on the U-Net adaptation. Some changes were made to make the proposed model distinguishable from U-Net, i.e. the removal of max-pooling operation, the reduction of successive convolutions and middle layers feature maps. The ensemble strategy combined the input image with basic network outputs for sequential improvement of model propagation. The proposed framework is evaluated on the DRIVE dataset and has achieved 96.85%, 79.79%, and 98.57% of accuracy, sensitivity, and specificity, respectively.

Guo et al. [276] have presented a multiple retinal deep CNN (MD-CNN) designed and trained with low contrast retinal images. The incremental learning approach was used in MD-CNN for improving the performance of the networks. For the final classification results, the plurality voting system is used. The proposed technique is validated on the DRIVE and the STARE datasets, achieving an AUC and accuracy scores of 97.37%/95.39% and 96.13%/95.39% respectively. For the segmentation of the retinal vessels, a deep supervision and smoothness regularization network (DSSRN) is proposed by Lin et al. [277]. The approach is developed with an edge detector by using the VGG network along with the global regularization of smoothness from conditional random fields (CRFs). The proposed approach achieves accuracy at state-of-the-art levels, but an overall sensitivity is low in comparison to other traditional approaches. The proposed approach is evaluated on three publicly available datasets that achieve an accuracy of 96.03%, 95.36%, 95.87%, and sensitivity of 74.23%, 76.32%, 78.15% on STARE, the DRIVE, and CHASE DB1, respectively. Hu et al. [279] presented a CNN and fully-connected Conditional Random Fields (CRFs) based retinal vessels segmentation. The segmentation procedure is divided into two parts: first, create a probability map using a multiscale CNN with an improved loss function and a multiscale network that combines the feature maps of each layer to extract more information about the retinal vessels; and second, create a probability map using a multiscale CNN with an improved loss function and a multiscale network that combines the feature maps of each layer to extract more information about the retinal vessels. In the second stage, CRFs are used to achieve the final binary segmentation. On the DRIVE and the STARE datasets, the suggested technique obtains 77.72% /75.43%, 97.93% /98.14%, 95.33% /96.32%, 97.59% /97.51% of sensitivity, a specificity, an accuracy, and an AUC, respectively. Guo et al. [280], proposed utilizing a deeply supervised neural network with Bottom-Top Short Connections to segment blood arteries (BTS-DSN). The approach uses short connections to transmit semantic information throughout the side output levels. Short connections are used to carry semantic information throughout the side output levels in this method. The proposed method transfers semantic data using two types of short links, top, and bottom, to maximize outcomes and reduce noise in both directions.

Experimentation is carried out using ResNet-101 and the VGGNet model. The model achieves 82.12%/78.91%, 98.59%/98.06%, 98.43% / 98.04%, and 84.21%/82.49% of sensitivity, AUC, specificity, and F1-score on the STARE and the DRIVE, respectively. The proposed

model however is limited to the precise one to several pixels wide segmentation of the micro vessel. Yan et al. [281], presented a novel approach for segmenting the thick and thin blood vessels. To avoid the mismatch problem and improve segmentation accuracy, all thick and thin vessels are separated independently. The vessel's fusion is used to refine findings and show whether a pixel belongs to the vessel or not. Three publicly available databases, DRIVE, STARE, and CHASE_DB are used to assess the suggested hybrid technique which has achieved the sensitivity, AUC, accuracy, and specificity of 77.35%, 97.50%, 95.38%, and 98.20% on STARE, 76.31%, 97.50%, 95.38% and 98.20% on DRIVE and 76.41%, 97.76%, 96.07% and 98.06% on CHASE_DB respectively. The automatic CNN-based segmentation model for the segmentation of the retinal blood vessels was developed by Jin et al. [282]. To begin, image preprocessing methods such as G-channel extraction, CLAHE, and gamma correction are used to improve retinal image quality. Then, a series of layers is added for low-contrast and different images in order to construct one-size patches of all models within the proposed network. Finally, for retinal vascular segmentation, the five pre-trained models LeNet, AlexNet, ZF-Net, VGG, and Deformable-ConvNet were modified. The highest AUC of 98.44% (AlexNet) and 97.64% (ZFNet) is achieved on the DRIVE and the STARE, respectively.

Jin et al. [283] used the CNN-based deformable U-Net (DUNet) model for segmentation of the retinal vascular, which relies on the vessels' different features. Up-sampling operators improve the output resolution and capture contextual data by combining high and low-level features to enable exact localization in DUNet. Vessel features are improved by the specific image preprocessing steps. A single-channel RGB photo was taken because it preserves more contrast from the vessel background; the vessel's details and the background are enhanced with CLAHE; gamma correction is a technique for improving image quality. The vessels are extracted using a technology that regulates the receptive field on different shapes and scales. The proposed method is evaluated on four publicly available datasets STARE, HRF, DRIVE, CHASE DB1 and has obtained an accuracy of 96.51% on the HRF and AUC of 98.32% on the STARE database. The improved CNN deep model for the retinal vessel segmentation was presented by Yang et al. [284]. Three processes are employed to improve data augmentation: rotating and mirroring images at various angles to boost training datasets, image preparation such as CLAHE to reduce noise and improve image quality, and retinal blood vessel segmentation using a deeper CNN in conjunction with the U-Net. The proposed technique was validated on the DRIVE dataset and achieves an average AUC, sensitivity, specificity, and accuracy of 88.50%, 97.30%, 79.70%, and 95.10% respectively. Based on a patch-based learning technique, Wang et al. [286] introduced the Dense U-Net for retinal vascular segmentation. Model training collects training patches at random, uses U-Net as a training network, and augments the dataset with random transformations, whereas testing divides images into patches, predicts test patches using the training model, and uses sequence patch methods to construct segments. The suggested technique was tested on two datasets, the DRIVE and the STARE, and attained accuracy, specificity, sensitivity, and AUC values of 95.11% /95.38%, 97.36% /97.22%, 79.86% /79.14%, and 97.40% /97.04%, respectively. During the binarization process, the splitting of fine retinal vessels takes place in the method presented, improved through the use of post-processing steps. Dharmawan et al. [288], proposed a hybrid vessel segmentation approach that combines U-Net-derived retinal vascular enhancement with CNN. Multiscale orientation modified filtered function of the Dolph-Chebyshev type-I (MDCF-I) is the method for the enhancement of retinal vessels. Evaluation of the proposed method was performed on three publicly available datasets the DRIVE, the STARE, and the HRF, and achieves notable results on the DRIVE with 83.14% of sensitivity, 97.26% of specificity, and 97.86% of the AUC. The method proposed is useful to treat vessels with a low contrast, the detection of vessels with pathologies and center reflex vessels.

In retinal vessel segmentation, a deep, dilated convolutional network-based on the architecture of the encoder–decoder has been proposed by Hatamizadeh et al. [289]. The dilated spatial pyramid pooling together with different dilation levels restores the missing contents of the encoder and introduces multi-scale contextual information into the decoder. The blood vessel width is determined through segmentation predictions, which feed the entire image to the network rather than a patch-specific technique. The proposed approach achieved sensitivity, specificity, and accuracy of 81.97%/83.00%, 98.19%/98.48%, 96.86%/97.50% on the DRIVE and the CHASE DB1, respectively. Fan et al. [290], proposed the octave CNN encoder–decoder model of the accurate segmentation of the blood vessel. Vanilla convolution is used to extract features, and it is good for many spatial frequency features, unlike traditional deep learning methods. The octave transposed convolution is used to decode the multi-frequency characteristics. In addition, an octave U-Net, featured by FCN, is proposed for the accurate segmentation of the vessel in single forward feed. The Octave U-Net extracts hierarchical features and performs end-to-end training without the use of any pre-processing or post-processing methods. The method was evaluated on publicly available databases DRIVE, STARE, CHASE_DB1, and HRF and achieves an accuracy, AUC, specificity, and sensitivity of 96.61%, 98.18%, 98.27%, and 79.57%, on DRIVE, 97.41%, 98.92%, 98.70% and 81.64% on STARE, 97.14%, 98.51%, 98.53% and 80.20% on CHASE_DB1 and 97.63%, 98.91%, 98.74% and 82.44% on HRF database. Ribeiro et al. [291], execute retinal vascular segmentation using a U-Net model-based on a baseline network architecture, as well as two ensemble training approaches, average stochastic weighting (SWA) and snapshot (SE). The presented method is validated on DRIVE and achieves an accuracy, sensitivity, and specificity of 95.69%, 78.80%, and 98.19%, respectively. Noh et al. [292] performed blood vessels segmentation with scale-space theory embedded neural network architectures. The proposed SSANet network was designed to combine up-sampling, residual lines, and downsampling. The proposed technique was validated on three databases DRIVE, CHASE_DB1, and STARE, and achieves an accuracy, AUC, specificity, and sensitivity of 97.78%, 99.16%, 85.23%, and 98.71% respectively. For thin vessel segmentation and vessel boundary localization, the SSA network offers tremendous potential.

Soomro et al. [293] proposed a strided-CNN technique for tiny vessels segmentation focusing on deep CNN. The encoder–decoder method, which replaces the pooling layers with strided constitutional layers, establishes the model. Principal component analysis (PCA) and morphological operations are used to process the images from the training dataset. In addition, skip connections were applied, which combine encoder and decoder parts to improve the details of tiny vessels. The proposed approach achieves sensitivity, accuracy, specificity, and AUC of 82.20%, 95.10%, 97.90%, 97.60% on the DRIVE, 80.90%, 95.30%, 97.40%, 97.20% on the STARE, 80.20%, 89.10%, 96.80%, 97.40% on the CHASE DB1, 78.60%, 94.80%, 96.40%, 96.50% on HRF. Jiang et al. [294], presented a deep CNN-based method for retinal vessel segmentation. The loss of function in the encoder part is decreased by decreasing the downsampling factor for the segmentation of small vessels. The model's receptive field is amplified, and the grid problem is reduced, thanks to the coupled dilated convolution. To gather deep and better information about retinal vessels, a multiscale information fusion (MSIFs) was applied. The proposed deep CNN-based architecture achieves 97.09%/97.81%, 98.90%/99.04%, 78.39%/82.49%, 98.64%/99.27% of accuracy, specificity, sensitivity, and AUC, respectively on the DRIVE and the STARE dataset. Feng et al. [296], presented a CNN-based cross-connected network (Cc-Net) for retinal vascular segmentation that uses multi-scale information. The CcNet's convolution layers extract the information and predict the pixel classes for these features. To train and test the proposed model, retinal images were extracted from the G-channel. The cross-connection is used to fuse multiscale features between primary and secondary track. The proposed CcNet has obtained an accuracy of 95.28% and a sensitivity

of 76.25% on the DRIVE database. Jiang et al. [298] presented a new retinal vascular segmentation network based on U-Net, named the multi-scale cross-position attention network (MCPANet). Authors proposed a cross-position attention module to link pixel positional relationships and gather global contextual information, allowing the model to segment not just fine capillaries but also clear vessel margins. Simultaneously, several scale pooling operations are used to widen the receptive field and improve feature extraction. It minimizes pixel categorization mistakes even further and makes segmentation easier due to the asymmetry of fundus blood vessel distribution. The proposed approach achieves accuracy of 97.05%, 97.58%, and 97.68%, and Dice of 83.15%, 81.48%, and 85.05%, on DRIVE, CHASE, and STARE datasets, respectively. Khan et al. [45] presented T-Net, a fully convolutional network that is especially well suited for resource restricted and mobile devices that lack the computing capabilities required by much bigger networks. The T-Net design enables dual-stream information transfer both inside and outside of the encoder–decoder pair. The authors have employed group convolutions to widen the network and so learn a greater number of low and intermediate level characteristics. They have also used skip connections to minimize spatial information loss to a minimal. T-Net employs a dice loss for pixel-wise classification, reducing the impact of class imbalance. The proposed T-Net achieves an average sensitivity, specificity, accuracy, AUC and F1 score of 82.62%, 98.62%, 96.97%, 98.67%, and 82.69% on DRIVE dataset. Aurangzeb et al. [308] proposed the Anam-Net model, which can accurately segment retinal vessels while being computationally efficient. Anam-Net is a lightweight convolutional neural network (CNN) model with bottleneck layers in the encoder and decoder stages. The Anam-Net model contains 6.9 times and 10.9 times fewer parameters than the normal U-Net model and the R2U-Net model, respectively. The model attained sensitivity and accuracy of 86.01%, 96.60%, 86.97%, 97.28%, and 85.53%, 97.46% for the DRIVE, STARE, and CHASE-DB datasets, respectively.

C. Other techniques. Xu et al. [275] proposed a segmentation approach that is based on a deeply guided, multiscale, border-refining (MDGN-BR) neural network. In the case of ophthalmic diseases, the approach is used to deal with vessel structure which hinders tiny vessels. The network is set up on an encoder–decoder framework with deep supervision that includes the training of features performed. Skip connections are also used with the help of residual boundary refinement module in scaled-level to fuse features maps with the boundaries of the vessel. The proposed MDGN-BR framework was evaluated on publicly available datasets HRF and DRIVE achieving 97.70% and 97.93% of AUC, respectively. For the retinal vessel segmentation tasks, a Generative Adversarial Network has been used to improve the CNN's capability by Son et al. [285]. GAN was built around a U-Net-style generator with a variety of discriminators. The discriminators distinguish the output from the gold standard, and the generator produces realistic results. On the DRIVE and the STARE databases, the proposed technique obtained an accuracy of 98.10% and 98.73%, respectively. The segmented image's results are as follows: improved by combining anatomical, vascular, and optical techniques understanding of the disk and the usage of noise-reduction removal. Khan et al. [295], examined a scenario that provides a robust aggregate solution by introducing the supervised generalized Gaussian mixture classifier. A logistic function of linear mixtures with class-conditional probability density functions is used to create the classifier. The weighted pictures are modeled as Gaussian mixtures to improve classification performance. A Gaussian mix containing weighted images is used to train the classifier. On microscopic vessels, the proposed approach has a net effect of greater sensitivity. The proposed technique achieves 96.00%, 96.10%, and 96.40% accuracy on DRIVE, STARE, and CHASE DB1. Yun et al. [309] developed MTPA Unet, a new network model for extracting connections between local detailed features and creating complements utilizing long-distance dependence information, and applied it to the retinal

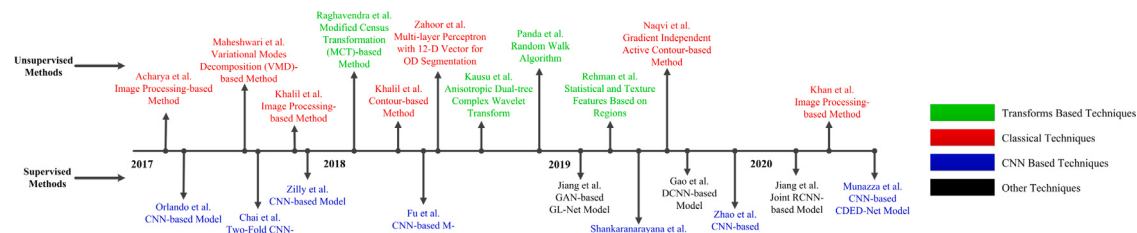


Fig. 9. Chronological summary of the recent optic disk/cup segmentation methods.

vascular segmentation challenge. MTPA Unet employs multi-resolution image input to allow the network to extract information at various levels. The suggested TPA module not only gathers long-distance relationships, but also focuses on vessel pixel location information to aid capillary segmentation. To achieve finer segmentation, the Transformer is serially integrated with the convolutional neural network, and the original MSA module is replaced by the TPA module. Finally, three well-known retinal image datasets, DRIVE, CHASE DB1, and STARE, are used to evaluate and analyze the network model. The accuracy metrics were 97.18%, 97.62%, and 97.73%; the sensitivity metrics were 84.10%, 84.37%, and 89.38%; and the Dice coefficient was 83.18%, 81.64%, and 85.57%. Chen et al. [310] proposes a Patches Convolution Attention-based Transformer UNet (PCAT-UNet), which is a U-shaped network with a Convolution branch based on a Transformer. The skip connection were used to join the deep and shallow features of both sides. Authors can effectively capture the global dependency connection and the intricacies of the underlying feature space by taking advantage of the complimentary benefits of both sides, thereby improving the current difficulties of insufficient extraction of retinal micro vasculature feature information and low sensitivity caused by easily guessing pixels as background. Furthermore, the proposed technique allows for end-to-end training and quick inference. Finally, PCAT-UNet was evaluated using three publicly accessible retinal vascular datasets (DRIVE, STARE, and CHASE DB1). The experimental results demonstrate that the proposed PCAT-UNET technique outperforms alternative designs in terms of AUC, Accuracy, and Sensitivity performance metrics, and achieves good retinal vascular segmentation performance on these three datasets. The following results were obtained: AUC was 98.72%, 99.53%, and 99.92%; Accuracy was 96.22%, 97.96%, and 0.98.12%; and Sensitivity was 85.76%, 87.03%, and 84.93% on each dataset respectively. Le et al. [311] created a new strategy for automatically and iteratively detecting and correcting such noisy segmentation labels during network training. The network-in-historical training's predicted label mappings from various epochs are taken into account, and they are jointly used to self-supervise the predicted labels during training and dynamically correct the supervised labels with noises.

7.2. Optical disk/optical cup

There are a many methods and approaches for optical disk and optical cup segmentation. These method are divided into two categories i.e. un-supervised methods and supervised methods. A detailed review of different unsupervised and supervised optical disk and optical cup methods is presented in this research. Tables 6 and 7 provide the performance metrics of the supervised and unsupervised methods with the evaluation criteria, dataset, and publication year respectively. Fig. 9 illustrate the chronological summary of the recent optic disk/cup segmentation methods.

7.2.1. Unsupervised methods

The unsupervised techniques are further grouped into Transforms-based techniques and classical techniques.

A. Transforms-based techniques. Raghavendra et al. [312], proposed a new technique for the detection of glaucoma using optical and non-parametric GIST descriptor. The method proposes a new optical disk segmentation based on the area followed by radon transformation (RT). A modified census transformation (MCT) compensates the change in the light levels of radon transformed images. The images of the MCT are then subject to the GIST descriptor to extract the energy spectrum of the spatial envelope. The proposed system achieves an accuracy of 97.00%, sensitivity 97.80% and specificity 95.80%. Kausu et al. [313], proposed a new way of identifying glaucoma based upon cup-to-disk ratio and anisotropic dual-tree complex wavelet transformational features. The clustering process of optic disk segmentation was done by Fuzzy C-Means and Otsu thresholding. The proposed method achieved an accuracy of 97.67% and sensitivity of 98.00% using a multilayered perceptron model. Panda et al. [314], proposed an enhanced version of OD segmentation based on random walk algorithm. The algorithm integrates the mean curvature and Gabor texture energy features in order to measure the new composite weight function. Contrary to model deformations, the proposed algorithm remains without the initialization of the curve and with the minimum local energy problem. The performance of the proposed technique is tested on DRIVE, DIARETDB1, DRISHTI-GS and MESSIDOR database. The method achieves sensitivity 91.67% / 92.03% / 95.52% / 91.68%, specificity 99.83% / 99.80% / 99.66% / 99.94% and precision 92.57% / 95.74% / 94.41% / 93.60%, respectively. Rehman et al. [315], presented a multiple optical disk detection and localization method for the use of statistical and texture features based on regions for retinal fundus images. Highly discriminative features were chosen on the basis of the common parameters of knowledge and a comparative study of four benchmark classifiers. The proposed method demonstrate its highly competitive accuracies of 99.30%, 98.80% and 99.30% on the DRIONS, MESSIDOR and ONHSD databases, respectively.

B. Classical techniques. A new approach and computerized diagnostic system are presented by Acharya et al. [316]. To transform color photos to grayscale images, adaptive histogram equalization is used, followed by the filtering banks Leung-Malik (LM), Schmid (S), and MR4 and MR8. Textons are the simple microstructures seen in most photographs. Textons are created by the convolution cycle. These textons will extract local configuration pattern features (LCP). The SFFS approach was used to pick the significant features, and the statistical t-test was applied. Finally, images were classified into normal and glaucoma classes using various classifiers. A high accuracy of classification of 95.80% was achieved. In order to get a robust and efficient method, an integrative glaucoma index (GRI) is also developed. Maheshwari et al. [317], presented a new method of automated glaucoma diagnosis. For image decomposition, the process of variational modes decomposition (VMD) was used iteratively. Different features were extracted from VMD elements, namely Kapoor entropy, Renyi entropy, Yager entropy and fractal dimensions. For the selection of classification, the ReliefF algorithm was used and these features were fed to a classification method for fewer squares support vector machine (LS-SVM). The proposed method achieved classification accuracies of 95%/19% and 94%/79% using three-fold and ten-fold cross-validation strategies, respectively. Khalil et al. [318], proposed a reliable CAD system that

Table 6

Performance Measures of Unsupervised Methods Optical disk and Optical cup segmentation: Year wise best results on different datasets are highlighted with different colors i.e.(Red color for DRIVE, Blue-Violet color for Glaucoma_DB, Thistle color for RIM-ONE, Magenta color for DIARET_DB1, Brown color for MESSIDOR, Chocolate color for ONHSD, Dark Magenta color DRIONS-DB, and Dark-Slate Gray color for Drishti_DB).

Year	Author	Method	Dataset	Performance measures (%)				
				Accuracy	Sensitivity	Specificity	Precision	
2017	Acharya et al. [316]	Image processing-based method	Glaucoma_DB	–	95.70	96.20	93.70	N.A
	Maheshwari et al. [317]	Variational Modes Decomposition (VMD)-based method		–	94.79	93.62	95.88	N.A
	Khalil et al. [318]	Image processing-based method		92.00	96.00	94.00	N.A	
2018	Raghavendra et al. [312]	Modified Census Transformation (MCT)-based method	–	97.00	97.80	95.80	N.A	
	Zahoor et al. [319]	Multi-layer perceptron with 12-D vector for OD segmentation	HRF	96.90	91.52	98.01	N.A	
	Khalil et al. [320]	Contour-based method	RIM-ONE	99.70	84.00	99.87	N.A	
	Kausu et al. [313]	Anisotropic Dual-tree Complex Wavelet Transform	AFIO	94.00	93.00	95.00	N.A	
			–	97.67	98.00	97.10	N.A	
	Panda et al. [314]	Random Walk Algorithm	DRIVE	N.A	91.67	99.83	92.57	
2019	Rehman et al. [315]	Statistical and Texture Features Based on Regions	DRISHTI-GS	N.A	95.52	99.66	94.41	
			DIARETDB1	N.A	92.03	99.80	95.74	
			MESSIDOR	N.A	91.68	99.94	93.60	
	Naqvi et al. [321]	Gradient Independent Active Contour-based Method	DRIONS	99.30	96.90	99.30	N.A	
			MESSIDOR	99.80	93.40	98.70	N.A	
			ONHSD	99.70	92.60	99.10	N.A	
2020	Khan et al. [322]	Image processing-based method	MESSIDOR	98.60	94.86	98.96	N.A	
			DRIONS-DB	96.72	91.30	98.00	N.A	
			ONHSD	98.51	93.64	98.85	N.A	
			DIARET_DB1	99.50	93.37	99.65	N.A	
			MESSIDOR	99.21	92.91	99.53	N.A	
			DRIONS-DB	99.31	94.41	99.56	N.A	
			Drishti-DB	99.60	96.49	99.75	N.A	
			RIM-ONE-DB	99.09	96.11	99.32	N.A	
			ONHSD	98.99	93.41	99.10	N.A	

combines hybrid structural and textural features. A variety of glaucoma conditioned were analyzed to improve the decision making process of system. Hybrid structural feature-set (HSF) and hybrid texture feature-set (HTF) were the two main module of the proposed system. A novel algorithm was also proposed to detect the damaged cup. This feature surpassed the state-of-the-art by achieving 94% of sensitivity. The cup-to-disk ratio approximation method has been implemented to improve overall accuracies for cup and disk segmentation using two separate channels. Exceptional results were obtained with 100% accuracy for glaucoma comparison. Zahoor et al. [319], presented as a correction to their previous paper, which shows only the first step in pipeline segmentation in retina images, i.e. fast and robust OD segmentation. The remaining phases of the glaucoma detection were presented in this corrected article. The segmented OD is prepared to emphasize the NRR and area of OC. For pixel classification-based OC segmentation, a multi-layer perceptron with 12-D vector was used. OD and OC segmentation extract the cup-to-disk ratio and other contextual features. To distinguish Glaucomatous and non-Glaucomatous images, a random subspace ensemble classifier based on decision trees was used. The proposed method was evaluated on two publicly available HRF and RIM-ONE datasets and achieves an accuracy, sensitivity and specificity of 96.90%, 91.52% and 98.01% for HRF and 99.70%, 84.00% and 99.87% for RIM-ONE dataset, respectively.

Khalil et al. [320], introduced a novel technique to improve the accuracy of extraction of ILM layers. It also uses an innovative approach to optimize the ILM layer contour. In addition, there was also a new criterion for evaluating cup edges based on the average RPE-level endpoint value. On a local dataset obtained from the Armed Forces Institute of Ophthalmology (AFIO), the suggested technique obtains a sensitivity of 93.00%, an accuracy of 94.00%, and a specificity of 95%. Naqvi et al. [321], proposed an approach based on OD homogenization and a related contour estimate to solve the issues of OD detection in circumstances where the OD limit is either discontinuous or highly smooth due to the presence of a disease. It was done by approximating the OD boundary with local laplacian vascular filters and employing a gradient-independent active contour for unregulated detection of the OD boundary. The propose method achieves sensitivity, specificity and accuracy of 94.86%, 98.96% and 98.60% on MESSIDOR, 91.30%,

98.00% and 96.72% on DRIONS-DB and 93.64%, 98.85%, 98.51% on ONHSD dataset, respectively. Khan et al. [322], presented a new and rapidly as well as comprehensive approach to OD localization and segmentation. The image was enhanced with de-hazing in the proposed method, and then cropped the OD area. The image was transformed to HSV and then V is used to detect OD. The vessels were extracted by multi-line detector from the G-channel and then removed by a Laplace Transform in the cultivated region. Binarization applies to local adaptive thresholds and region growing methods. In addition, the true OD region was then detected by two regions, eccentricity, and area. In order to fill the region the method of ellipse fitting was used. The propose method achieves accuracy on MESSIER and DRIONS databases 99.00% and 100% respectively.

7.2.2. Supervised methods

The unsupervised techniques are further grouped into CNN-based techniques and other techniques

A. CNN-based techniques. In order to develop a CNN model for automatic glaucoma detection, Orlando et al. [323] adopted two separate OverFeat and VGG-S architectures respectively. In the identification of glaucoma using fundus images, the main aim of the implementation of pre-trained architectures of non-fundus images is to validate current CNN architectures (VGG-S and OverFeat). The obtained fundus images are preprocessed first to improve the image quality and then segmented by ONH. The proposed model achieves AUC values of 76.30% and 71.80%, respectively. Chai et al. [324], developed a two-fold CNN framework to improve global glaucoma identification. The divided optic disk area was given to CNN after the complete image was applied to the CNN model. As a source of data, The CNN models were then concatenated. A fully connected layer accompanied the classification. The created model had a classification accuracy of 81.69%. Rather than introducing the complete fundus image into the classification model CNN, Zilly et al. [325], calculated the CDR from the fundus images and assessed images based on the CDR values. Authors used CNN to find and divide ROI with entropy sampling. A 94.10% of accuracy is achieved with CDR value. Fu et al. [326], presented the M-Net design, which uses a one-stage framework to solve the segmentation of OC and

Table 7

Performance Measures of Supervised Methods for Optic Disk and Optic Cup Extraction: Year wise best results on different datasets are highlighted with different colors i.e.(Thistle color for RIM-ONE, Coral color for ORIGA, and Dark-Slate Gray color for Drishti_DB)

Year	Author	Method	Dataset	Feature	Performance measures in (%)				
					Accuracy	Sensitivity	Specificity	AUC	F1 score
2017	Orlando et al. [323]	CNN-based model	SCES	-	N.A	N.A	N.A	89.80	N.A
	Chai et al. [324]	Two-Fold CNN-based model	DRISHTI-GS1	-	N.A	N.A	N.A	76.30	N.A
	Zilly et al. [325]	CNN-based model	Beijing Tongren Hospital China	-	81.69	N.A	N.A	N.A	N.A
2018	Fu et al. [326]	CNN-based M-Net Model	ORIGA	-	N.A	N.A	N.A	85.08	N.A
2019	Jiang et al. [329]	GAN-based GL-Net model	DRISHTI-GS1	OD	N.A	N.A	N.A	N.A	97.10
	Shankaranarayana et al. [328]	CNN-based model	ORIGA	OC	N.A	N.A	N.A	N.A	90.50
			RIM-ONE	-	N.A	N.A	N.A	84.04	N.A
	Gao et al. [330]	DCNN-based model	DRISHTI-GS	OD	N.A	N.A	N.A	N.A	95.00
	Zhao et al. [331]	CNN-based model	ORIGA	OC	N.A	N.A	N.A	N.A	85.20
2020	Jiang et al. [332]	Joint RCNN-based Model	ORIGA	-	N.A	N.A	N.A	85.40	N.A
	Munazza et al. [333]	CNN-based CDED-Net model	SCES	-	N.A	N.A	N.A	90.10	N.A
			Drishti-GS	OD	99.66	97.54	99.73	96.90	N.A
			OC	99.71	95.67	99.81	95.70	N.A	
			RIM-ONE	OD	99.56	97.34	99.73	98.70	N.A
				OC	99.61	95.17	99.81	90.90	N.A

OD in a multi-label system. This suggested M-Net includes a multi-scale input layer, a U-shaped convolutional network, a side output layer, and a multi-label loss function. A multi-level receptive field pyramid is created by the multi-scale input layer. The U-shape convolutional network is used to learn the rich hierarchical representation as to the body network's fundamental structure, while the side-output layer serves as an early classification layer that generates local prediction maps for various scale layers. Finally, a multi-label loss function was used to create the final segmentation map. The polar transformation, which depicts the original image in the polar coordinate system, is also used to improve segmentation performance. On the ORIGA and SCES datasets, the suggested technique achieves CDR of 85.08%, 89.98%, and AUC of 85.08%, 89.97%, respectively. Wang et al. [327], developed a new patch-dependent Input Space Adversarial Learning Framework (pOSAL), which jointly and robustly combines the OD and OC from a range of fundus image datasets. First, they model as a backbone a lightweight and efficient segmentation grid. In view of OD and OC's unique morphological characteristics, the network is proposed to generate accurate and smooth segmentation. In order to resolve the domain shift issue, our pOSAL architecture then uses unsupervised domain adaptation to enable segmentation in the target field to be close to the source one. Considering that the overall segmentation based adversarial loss is inadequate to get the network to capture segmentation data, pOSAL is built more patch based so that the local segmentation details are subject to fine-grained. Shankaranarayana et al. [328], proposed a deep learning architecture for estimating the depth of a single retinal fundus image. For the monocular retinal depth estimation, the labeled data insufficiency still plagues the authors. The pre-training technique of the deep network is used in order to solve this problem, where a new pre-trained method called pseudo-depth reconstruction is proposed instead of using a de-noisy auto encoder, which serves as a proxy for the retinal depth estimation. Empirically, it is a better proxy task than the de-noising process. The proposed segmentation was tested on ORIGA and RIMONEr3 datasets and achieves an AUC of 84.04% and 93.90%, respectively.

Zhao et al. [331], proposed an automated optic disk (OD) localization glaucoma screening pipeline is suggested in this study to predict the risk of glaucoma. There are three main phases to the proposed pipeline. Firstly, morphological analysis and sliding window methods are used to localize the OD. Second, to break up simultaneous OD and OC, a new neural network in U-shaped was introduced and a fusion loss function was developed. Third, neuroretinal features, and hidden features, including statistical moments, entropy and energy,

are combined for the training of Glaucoma classifiers in the clinical measurements like optic cup-to-disk ratio (CDR). The performance of the proposed approach is tested on the RIGA dataset and achieves an accuracy, sensitivity, specificity, and AUC of 82.80%, 87.60%, 77.90%, and 88.90%, respectively. Wang et al. [334], proposed a deep learning framework to locate the ellipse for optical disks (OD) and optical cup (OC) areas jointly. To recover the morphology of each OC and OD region for the calculation of the cup-to-disk ratio, the parameters of an ellipse were directly estimated instead of a bounding box, as in typical object detection algorithms. To detect ellipses in the OC and OD regions, we use two modules, one of which focuses the OD region on the OC. On the REFUGE dataset, the suggested technique obtains a CDR of 0.047. For the mutual segmentation of optic disk (OD) and optic cup (OC), Munazza et al. [333] proposed a Cup Disk Encoder Decoder Network (CDED-Net). Authors also eradicated the steps of pre-processing and post-processing to reduce the overall system's computational complexity. (OD) and OC segmentation is modeled as a problem of semantic pixel-wise labeling. The CDED-Net was evaluated on two publicly available datasets Drishti-GS and RIM-ONE and achieves an accuracy, sensitivity, specificity and AUC of 99.66%, 97.54%, 99.73%, 96.90% for OD, 99.71%, 95.67%, 99.81%, 95.70% for OC on Drishti-GS dataset and 99.56%, 97.34%, 99.73%, 98.70% for OD 99.61%, 95.17%, 99.81%, 90.90% for OC on RIM-ONE dataset.

B. Other techniques. Jiang et al. [329], proposed GL-Net, a DCNN multi-label model combining generative adversarial networks. GL-Net contains a generator and a discriminator in the two network structures. In the generator we use skip connections to promote the fusion of low-level information about features and high-level features, reducing the difficulties of restoring detailed information during up sampling and reduce the down sampling factor, thus effectively reducing excessive loss of information. The propose method achieves F1 scores of 97.10% and 90.50% for optic disk and optic cup, respectively. Gao et al. [330], proposed a model of locally active statistical appearance and shape information (LSACM-AS) and a modified locally active statistical model with appearance and shape information (MLSACM-AS). A publicly accessible DRISHTI-GS database is used to evaluate the efficacy of proposed models. The propose method achieves F1 scores of 95.00% and 82.20% for optic disk and optic cup, respectively. Jiang et al. [332], proposed a region based end-to-end CNN for optical disk and optical cup segmentation (referred to as a joint RCNN). To increase the performance of the extraction module, atrous convolution is introduced. The Joint RCNN proposes to generate proposals for bounding boxes

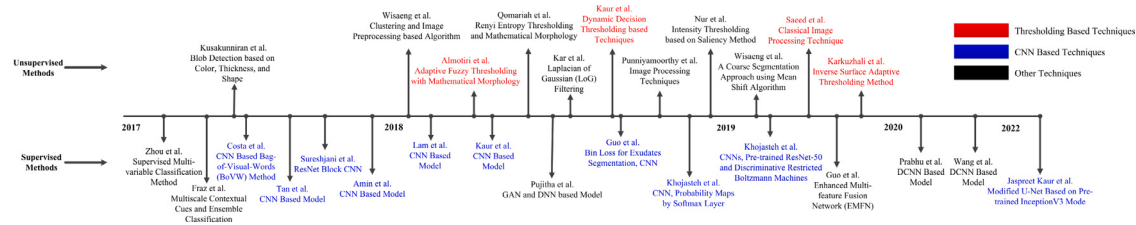


Fig. 10. Chronological summary of the recent exudates segmentation methods.

for optical disk and cup respectively, named as Disk Proposed Network (DPN) and Cup Proposal Network (CPN). Given the knowledge of the optical disk, the disk attention module is proposed to connect DPN and CPN when an appropriate bounding box is selected and then further spread as an optical cup detection basis in proposed network. The vertical cup-to-disk ratio (CDR) for glaucoma detection is measured and used after obtaining the disk and cup regions which are the inscribed ellipse sections of the corresponding observed bounding boxes. The joint RCNN was evaluated on two publicly available datasets ORIGA and SCES and achieves AUC of 85.40 and 90.10%, respectively.

7.3. Exudates

There are various approaches and techniques for exudates segmentation. These approaches are divided into two types, i.e. un-supervised methods and supervised approaches. In this section, a detailed review of different unsupervised and supervised exudates approaches is presented. Tables 8 and 9 provide the performance metrics of the supervised and unsupervised approaches with the evaluation criteria, dataset, and publication year respectively. Fig. 10 illustrate the chronological summary of the recent exudates segmentation methods.

7.3.1. Unsupervised methods

The unsupervised techniques are further grouped into thresholding-based techniques and other techniques.

Thresholding-based techniques. Almotiri et al. [335], proposed an automated image segmentation system consisting of three subsystems of segmentation following the same core algorithm. Each sub-system extracts retinal blood vessels, optic disks and lesions without the need for texture analysis or synthesis, despite the broad diversity in features and characteristics. The proposed method can identify these anatomical structures even in pathologically affected retina images in one session, in order to ensure a compact diagnosis and a full clinical insight. To integrate adaptive fuzzy thresholding with mathematical morphology, a robust hybrid segmentation approach was used. The suggested approach was then tested against four publicly available datasets: the DRIVE and the STARE for vasculature, the DRISHTI-GS for the optic disk, and the DIARETDB1 for exudate lesions. The proposed segmentation technique achieves an accuracy, sensitivity, specificity and PPV of 83.40%, 75.80%, 85.70% and 41.67%, respectively for exudates detection on DIARETDB1. Kaur et al. [336], presented a generalized exudates segmentation technique to help ophthalmologists to treat diabetic retinopathy quickly and efficiently. A reliable segmentation of exudates using a dynamic decision threshold irrespective of its associated heterogeneity, faint edges and brightness is the main contribution of the proposed method. The method is robust such that, it selects the threshold value dynamically for different fundus images. Since the standard databases does not provide a comparison of the state of the art methods, this work was carried out on a diversified database with 1307 retinal fundus images that have different characteristics, namely location, shape, color and scale. The database consists of 649 retinal fundus images acquired clinically from the eye hospital and 658 retinal images from public databases such as STARE, DIARETDB1, MESSIDOR and e-Ophtha EX. The segmentation results of the proposed method were validated on two sets

of experiments namely: lesion based evaluation criteria and image based evaluation criteria. The proposed technique achieves an sensitivity/accuracy/specificity of 88.85%/93.46%/96.15% at lesion level and 94.62%/98.64%/96.74% for image-based evaluation, respectively on a composite database. Saeed et al. [337], proposed an algorithm that is capable of detecting pathological changes in diabetic retinopathy (i.e. hard exudates). A total of 100 images (50 sick and 50 normal eyes) were used in the study. The authors employed classical image processing methods during the experiments, such as binarization or media filtration, and the d-Eye sensor were used to read data. 67 patients (39 females and 28 males between 50 and 64 years of age) were examined. The proposed system could automatically diagnose small lesions in retinopathy with an accuracy of 98.00%. Karkuzhal et al. [338], proposed the inverse surface adaptive thresholding method for exudate detection. Localization of OD is an important step in the analysis of the fundus image and the development of Computer Aided Diagnosis tool for DR. Detection of OD centers is necessary to reduce the false positive rate in exudate detection (EX). EXs is the early symptom of a white lesion found in the retina for the diagnosis of DR. OD is detected by the use of the intensity variation algorithm and EX is segmented by using inverse surface adaptive threshold algorithm. The inverse surface adaptive thresholding method was evaluated on DIARETDB0, DIARETDB1, MESSIDOR, DRIVE, STARE and Bejan Singh Eye Hospital databases and achieved an accuracy of 99.34%, 99.67%, 98.34%, 98.87%, 99.13%, 98.34%, a sensitivity of 97.43%, 98.87%, 99.12%, 97.21%, 98.72%, 96.63% and a specificity of 91.56%, 92.31%, 90.21%, 90.14%, 89.58%, 92.56%, respectively.

B. Other techniques. Kusakunniran et al. [339], proposed a three-stage approach for retinal exudate segmentation. Pre-processing is the first stage. The color conversion is used to render all retinal images based on statistical analysis with the same color characteristics. Then, only a yellow channel is used for each image. The second step is the blob initialization. Initial pixels of hard exudates are classified by using blob-detection based on color, thickness, and shape including circularity and convexity. The detected blobs should not be on the optical disk. The segmentation is the third step. The graph cut is applied iteratively to the image partitions. nFine tuning segmentation is required in sub-images because the portion of hard exudates is much lesser than the portion of non hard exudates. For both pixel-level and image-level the proposed approach is evaluated using the two popular datasets, namely eophtha and DIARETDB1. The proposed approach achieves a sensitivity of 96.00%, 96.00% and a specificity of 94.00%, 98.00% for the eophtha and DIARETDB1 datasets, respectively. For exudate detection, Wisaeng et al. [340], employed clustering and image preprocessing algorithms. Histograms, local contrast enhancement, median filtering, color space selection, and optic disk location were all used as pre-processing techniques. The authors used the SVM classification, naive Bayesian, and fuzzy C-mean classification system for categorizing regions of non-exudates and exudates. The final quality score for exudates was then calculated by putting exudates into mathematical morphological pipelines that had previously been categorized. Furthermore, mathematical morphology's ideal parameters increased the precision of fuzzy C mean clustering by 12.05%. On 200 unseen images, the suggested method achieves a sensitivity of 97.12%, specificity of 97.89%,

Table 8

Performance Measures of Unsupervised Methods for Exudates Extraction: Year wise best results on different datasets are highlighted with different colors i.e.(Red color for DRIVE, Green color for STARE, Blue color for E-Ophtha EX, Violet color for DIARETDB1, and Brown color is for MESSIDOR dataset).

Year	Author	Method	Dataset	Performance measures in (%)		
				Accuracy	Sensitivity	Specificity
2017	Kusakunniran et al. [339]	Blob detection based on color, thickness, and shape	DIARETDB1	N.A	84.30	99.90
			e-Ophtha	N.A	96.00	94.00
			200 unseen images	97.45	97.12	97.89
			DIARETDB1	83.40	75.80	85.70
2018	Wisaeng et al. [340], Almotiri et al. [335], Kar et al. [341], Qomariah et al. [342]	Clustering and image preprocessing based algorithm Adaptive Fuzzy Thresholding with Mathematical Morphology Laplacian of Gaussian (LoG) Filtering Renyi Entropy Thresholding and Mathematical Morphology	DIARETDB1	98.32	97.81	98.18
			DIARETDB1	99.54	85.06	99.63
			Clinical	100.00	98.80	100.00
			STARE	100.00	100.00	100.00
	Kaur et al. [336]	Dynamic decision thresholding based techniques	MESSIDOR	93.00	88.00	98.00
			DIARETDB1	89.00	91.00	94.00
			e-Ophtha EX	93.00	91.00	94.00
			DIARETDB1	N.A	96.07	97.36
2019	Punniyamoorthy et al. [343], Nur et al. [344]	Image processing techniques Intensity thresholding based on saliency method	DIARETDB1	99.33	81.65	99.42
			DIARETDB1	97.14	97.05	97.18
			Medical University of Białystok	98.00	100.00	96.00
			DIARETDB1	99.67	98.87	92.31
	Saeed et al. [337], Karkuzhali et al. [338]	A Coarse Segmentation Approach using Mean Shift Algorithm Classical image processing technique	MESSIDOR	98.34	99.12	90.21
			DRIVE	98.87	97.21	90.14
			STARE	99.13	98.72	89.58
			Bejan Singh Eye Hospital	98.34	96.63	92.56

Table 9

Performance Measures of Supervised Methods for Exudates Extraction: Year wise best results on different datasets are highlighted with different colors i.e.(Gray color for HEI-MED, Maroon color for IDRiD, Blue color for E-Ophtha-EX, Violet color for DIARETDB1, and Brown color is for MESSIDOR dataset).

Year	Author	Method	Dataset	Performance measures in (%)				
				Accuracy	Sensitivity	Specificity	AUC	PPV
2017	Zhou et al. [346]	Supervised Multi-variable Classification Method	DIARETDB1	N.A	87.56	94.65	96.03	N.A
			E-Ophtha-EX	N.A	N.A	N.A	96.70	N.A
			DIARETDB1	87.72	N.A	N.A	93.10	N.A
			E-Ophtha-EX	89.25	N.A	N.A	94.30	N.A
	Fraz et al. [347]	Multiscale Contextual Cues and Ensemble Classification	HEI-MD	95.77	N.A	N.A	98.42	N.A
			MESSIDOR	98.36	N.A	N.A	99.61	N.A
			MESSIDOR	N.A	N.A	N.A	90.00	N.A
	Costa et al. [348], Tan et al. [349]	CNN based Bag-of-Visual-Words (BoVW) Method	CLEOPATRA	N.A	87.58	98.73	N.A	N.A
			DIARETDB1	N.A	N.A	N.A	96.50	N.A
			E-Ophtha-EX	N.A	N.A	N.A	99.40	N.A
2018	Sureshjani et al. [350], Amin et al. [351]	ResNet Block CNN	—	98.58	N.A	N.A	98.00	N.A
			E-Ophtha-EX	N.A	N.A	N.A	95.00	N.A
			MESSIDOR	93.46	88.50	96.15	N.A	N.A
			Pujitha et al. [353]	GAN and DNN based model	—	89.70	N.A	95.60
	Guo et al. [354]	Bin Loss for Exudates Segmentation, CNN	E-Ophtha-EX	N.A	86.44	N.A	91.84	87.59
			IDRiD	N.A	91.67	N.A	94.85	88.84
			DIARETDB1	96.00	98.00	97.00	N.A	94.00
	Khojasteh et al. [355], Khojasteh et al. [356]	CNNs, Pre-trained ResNet-50 and Discriminative Restricted Boltzmann Machines	DIARETDB1	98.20	99.00	81.00	N.A	N.A
			E-Ophtha-EX	97.60	98.00	95.00	N.A	N.A
			MESSIDOR	93.00	N.A	N.A	N.A	N.A
			HEI-MED	94.00	N.A	N.A	N.A	N.A
2019	Guo et al. [357]	Enhanced Multi-feature Fusion Network (EMFN)	E-Ophtha-EX	92.00	N.A	N.A	N.A	N.A
			E-Ophtha-EX	98.67	72.26	98.76	97.29	N.A
			E-Ophtha-EX	N.A	89.90	N.A	N.A	88.68
			HEI-MED	N.A	94.77	N.A	N.A	91.79
			IDRiD	99.83	85.90	99.95	N.A	N.A
2020	Prabhu et al. [358]	DCNN based model	E-Ophtha-EX	98.67	72.26	98.76	97.29	N.A
2020	Wang et al. [359]	DCNN based model	E-Ophtha-EX	N.A	89.90	N.A	N.A	88.68
2022	Jaspreet Kaur et al. [360]	Modified U-Net Based on Pre-trained InceptionV3 Model	IDRiD	99.83	85.90	99.95	N.A	N.A

and accuracy of 97.45%. Kar et al. [341], proposed an automated lesion detection system for DR screening by using Laplacian of Gaussian (LoG) filtering and matched filtering for detection of bright lesion. For OD segmenting of the retinal image, a Fuzzy c mean kernel was employed. Exudates were enhanced through an optimal band pass filter. Differential evolution based contrast enhancement was used to detect the lesions. The matched filter response was subsequently maximized and the filter response LOG was used to detect exudates. The performance of the proposed algorithm was evaluated on the DIARETDB1 dataset and achieves 97.81%, 96.84%, 98.18%, and 98.32% of sensitivity, AUC, specificity, and accuracy respectively. Qomariah et al. [342], proposed a technique in which exudates were automatically detected

with Renyi entropy threshold and mathematical morphology. A controlling variable has a Renyi entropy threshold to set optimal threshold. The proposed method of Renyi entropy thresholding and mathematical morphology was divided into three stages : (1) contrast enhancement (preprocessing), (2) mathematical morphology based initial exudate detection and (3) Renyi entropy thresholding based exudates detection. The proposed technique achieves a sensitivity, specificity, and accuracy of 85.06%, 99.63% and 99.54%, respectively on DIARETDB1 dataset.

Punniyamoorthy et al. [343] used image processing techniques to detect the optic disk, exudates and macular edema from fundus

images. Their proposed method achieves 96.07%/97.75% sensitivity, 97.36%/100% selectivity, and 96.62%/98.86% accuracy, for exudates/macular edema detection, respectively. The comparison of results with other methods indicates that the proposed system can be used as a diabetic retinopathy screening tool. Nur et al. [344], proposed exudates segmentation using intensity thresholding with region obtained based on saliency method. The work has three main phases, namely the removal of optic disks, detection of exudates location and segmentation of exudates. The midpoint circle algorithm is used to eliminate optical disk. The image was subdivided into small patches at the detection stage of the exudates location and then classified into an exudate patch and exudate free patch based on the threshold for each image. For a subimage which is classified as a patch, it is segmented using the saliency method. The proposed method was evaluated on the diaretDB1 dataset and achieves an accuracy, sensitivity, and specificity of 99.33%, 81.65% and 99.42%, respectively. Wisaeng et al. [345], proposed a method that begin with retinal image normalization, contrast enhancement, noise removal and OD localization. A coarse segmentation approach then provides a set of exudates and non exudates candidates using a mean shift algorithm. Finally, a classification is applied using the mathematical morphology algorithm (MMA), so that only exudates pixels can be kept. The performance of the proposed technique was tested on the DIARETDB1 dataset and achieves sensitivity, specificity, and accuracy of 97.05%, 97.14%, and 97.18%, respectively. The performance of the proposed method is evaluated on DIARETDB1 dataset and achieves an average sensitivity, specificity, and accuracy 97.05%, 97.14% and 97.18%, respectively.

7.3.2. Supervised methods

The unsupervised techniques are further grouped into CNN-based techniques and other techniques.

A. CNN-based techniques. Costa et al. [348], for the identification of DR, a CNN arrangement was transmitted, which is a version of the bag-of-visual-words (BoVW) technique. The method's significance is based on the benefit that, unlike conventional BoVW, the system is capable of jointly performing feature extraction, classification, and feature encoding. The proposed method achieves an AUC of 90.00% on MESSIDOR dataset. Tan et al. [349] used multi class CNNs for the segmentation of Retinal pathologies simultaneously. For the automatic microaneurysms, exudates, and hemorrhages segmentation from retinal fundus images, they devised a ten-layer neural network. The leaky rectified linear unit was employed as an activation function for coevolutionary and fully connected layers, while the softmax function was used for the final fully connected layer. In addition, stochastic gradient descent and backpropagation were used to train the network, as well as regularization to avoid overfitting. Before feeding them to the network, the fundus images were normalized for local contrast and correction of the illumination. This CNN based method is data-dependent because a large number of training samples are required for the deep learning techniques. A local dataset CLEOPATRA was used to evaluate the proposed approach and achieved 98.73% specificity and 87.58% sensitivity. Ota'lora et al. [361] suggested this sort of methodology for exudate classification. In addition to an expected gradient length (EGL) and an active learning technique, they created an effective CNN model. EGL gave the learner some control by allowing them to pick and choose which examples to classify and add to the training set from a pool of unlabeled instances. During earlier CNN training convergence, EGL beat classical stochastic gradient descent in terms of providing the network with the most informative patches from retinal images. The CNN model was built on top of the LeNet network, and it was trained using the transfer learning method. In addition, the method's efficiency was evaluated by using E-Ophtha, a publicly available dataset. Suresh-jani et al. [350], proposed exudates segmentation method by using importance sampling. Importance sampling refers to prioritizing non-exudate data that may cause the network to be misled during training.

The proposed method was based upon a ResNeT. Before feeding them to the network the retinal images were enhanced using a Gaussian filter. Moreover, The stochastic gradient descent was used to optimize network weights. The proposed method was tested on DIARETDB1, DR2, and E-Ophtha-EX datasets and achieves an AUC of 97.2%, 96.5%, and 99.4%, respectively. Amin et al. [351] build an automated framework for differentiating exudates from non-exudates regions. To improve the lesion enhancement, they implemented Gabor filter as a preprocessing step. A combination of statistical and geometrical was then used to create a feature set for each lesion candidate. Finally, using vectors of extracted features, candidate regions were classified as non-exudates or true exudates regions using four classification families: geometric, probabilistic, KNN, and tree-based. The proposed method achieves 98% of an average AUC and 98.58% of accuracy. Lam et al. [352] introduced a segmentation method for exudates based on CNN. In the proposed paper, 243 retinal images were verified by two ophthalmologists, labeling important image subsections to generate 1324 image patches containing hemorrhages, microaneurysms, exudates, retinal vasculature or normal-appearing structures. Using these image patches, one standard convolutional neural network was trained to predict the existence of these five classes. Using a sliding window method, probability maps were generated over the entire image. The proposed method achieves an average AUC of 95.00% on E-Ophtha dataset.

Kaur et al. [336], developed a robust method based on dynamic decision thresholding for exudates segmentation from retinal images. The preprocessing of retinal images was performed using high pass filtering and enhancing local contrast and variance correction for normalizing irregular illumination. To reduce false positives in the exudate segmentation results, other anatomical components such as OD and blood vessels were identified and eliminated from improved retinal images. In addition, Canny edge detection and Hough transformation were used to detect OD and eliminated from image by using morphological operations. On vascular and improved retinal images, adaptive image quantization followed by dynamic decision thresholding was used. The proposed method achieves an average specificity, accuracy, and sensitivity of 96.15%, 93.46%, and 88.85% respectively. Guo et al. [354], developed a top-k loss, which tackles both class and loss unbalance by focusing more on the difficult-to-classify pixels. Furthermore, for efficiency, a fast form of the top-k loss known as bin loss was devised, decreasing the time complexity from $O(n \log n)$ to $O(n)$, where n is the number of background pixels. For the segmentation challenge of hard exudates, the suggested technique was tested on two available datasets, e-ophtha EX and IDRiD. HED, DeepLab v2, and FCRN, three popular image segmentation models, were also employed to test bin loss flexibility. The proposed method achieves a sensitivity, AUC and PPV of 86.44%/91.67%, 91.84%/94.85% and 87.59%/88.84% on e-ophthaEX/IDRiD, respectively. Extensive testing show that each model with the suggested bin loss outperforms one with CBCE loss, demonstrating that bin loss can be used in a variety of performance improvement models. The F-score improves by 5.2 percent for DeepLab over the e-ophtha EX, and the AUC improves by 10.6 percent. Furthermore, the AUC for both DeepLab and FCRN increases by more than 4% when compared to the IDRiD dataset. Khojasteh et al. [355], proposed an alternate strategy that would employ probabilistic output from a Convolution neural network to simultaneously detect hemorrhages, exudates, and microaneurysms. The novelty of the proposed approach is that rather than using the binary output, probability maps produced by the softmax layer score values were used to analyze the images. Patch and image-based analysis were carried out to test the performance of the proposed technique. The proposed method achieves an accuracy of 97.3% for DIARETDB1 and 86.6% for e-Ophtha. Khojasteh et al. [356] explored various techniques of deep learning to improve the sensitivity and specificity. In order to improve the performance of automated exudate detection, several deep learning approaches and both supervised and unsupervised classifiers

were compared, i.e., CNNs, pre-trained Residual Networks (ResNet-50) and Discriminative Restricted Boltzmann Machines. Two publicly accessible databases DIARETDB1 and e-Ophtha were used to perform the experiments. ResNet-50 with SVM outperformed the other networks with accuracy and sensitivity of 98.00% and 99.00%, respectively. This demonstrates that ResNet-50 may be used to detect exudates in fundus images analysis. Islam et al. [362], conducted a systematic literature search on EMBASE, PubMed, Google Scholar, and Scopus between January 1, 2000, and March 31, 2019. The search strategy was based on the Preferred Reporting Items for Systematic Reviews and Meta-Analyses (PRISMA) standards, and a DL-based research design was required for results inclusion. The systematic review included 23 studies; 20 studies met the meta-analysis requirements for inclusion. The pooled area under the receiving operating curve (AUROC) of DR was 97.00%, sensitivity was 83.00%, and specificity was 92.00%. The ratio of positive and negative likelihoods was 14.11 (95% CI: 9.91 to 20.07), and 0.10 (95% CI: 0.07 to 0.16), respectively. In addition, the DL model diagnostic odds ratio was 136.83 (95% CI: 79.03 to 236.93). All of the studies provided a DR-grading scale, a reference standard for a human grader (e.g. trained caregivers, ophthalmologists).

Jaspreet Kaur et al. [360] proposed a modified U-Net model based on the pre-trained CNN network InceptionV3. It employs a periodic shuffling strategy in combination with sub-pixel convolution that is initialized to convolution nearest-neighbor resize. On two standard datasets, IDRiD and DIARETDB1, the model was trained and validated for non-proliferative diabetic retinopathy, microaneurysms, haemorrhages, hard and soft exudates. On the IDRiD dataset, the proposed model achieves an accuracy of 99.82%, sensitivity of 88.39%, and specificity of 99.94% for haemorrhages segmentation, accuracy of 99.95%, sensitivity of 70.76%, and specificity of 99.98% for microaneurysms segmentation, accuracy of 99.83%, sensitivity of 85.9%, and specificity of 99.95% for hard exudates segmentation, and accuracy of 99.62%, sensitivity of 85.38%, and specificity of 99.71% for the segmentation of soft exudates on the IDRiD dataset.

B. Other techniques. Zhou et al. [346], developed a novel super-pixel multi-feature classification-based method for detecting exudates. It started with pre-processing fundus images with local and global methods to remove uneven illumination and contrast. The segregation of a whole image into super-pixels was used to identify candidate exudates. Following that, each potential exudate was assessed using 19 multi-channel intensity features and a unique contextual feature. A supervised multi variable classification method was designed to discriminate between false and true positive candidates. Finally, a novel OD detection technique was introduced as a post-processing step, which improved classification accuracy even more. The DIARETDB1 and E-Ophtha EX datasets were used in the studies, and the proposed technique achieves a sensitivity of 87.56%, an AUC of 96.03%, and a specificity of 94.65% for the DIARETDB1 dataset. Fraz et al. [347], use a multiscale exudate detection technique based on ensemble classification. By applying the Grow cut algorithm and polar transform the OD was localized. Parabola fitting approximated the main vascular arch region and removed the major anatomic structures i.e. the retinal vasculature. On the morphologically closed retinal image produced coarse-grained candidate exudates, adaptive contrast enhancement with Gabor filtering was applied. Using hysteresis thresholding, the Gabor filter response image was then morphologically reconstructed. By taking their supremum, coarse and fine-grained candidate exudates were combined. Using a 9-D feature vector that characterizes each candidate's region, a bagging decision tree classifier was trained to mean bootstrap aggregation to identify candidates as exudate or non-exudate areas. The suggested algorithm's efficacy was tested using the DIARETDB1, the E-Ophtha, the HEI-MD, and the MESSIDOR datasets. For the DIARETDB1, the E-Ophtha, the HEI-MD, and the MESSIDOR datasets, the proposed technique achieved an accuracy of 87.72%, 89.25%, 95.77%, and 98.36%, and an AUC of 93.1%, 94.30%, 98.42%, and

99.61%, respectively. Pujitha et al. [353], suggested a unique augmentation and synthetic image generation method for training deep neural net-based lesion diagnosis. Augmentation annotations are made less noisy by providing a reliability factor to crowd topics based on their results and requiring crowd area markings of interest. To develop digital images with lesions to monitor the disease's overall severity level, a generative, network-based adversarial approach is proposed. By providing a Deep Neural Network (DNN) training solution using data derived from a heterogeneous annotations combination, the reliability of crowdsourced annotations and synthetic images was established. The proposed approach has a sensitivity of 89.70%, an AUC of 95.60%, and a PPV of 93.40%, respectively. Guo et al. [357], Guo et al. [292] presented an Enhanced Multi-feature Fusion Network (EMFN) to reduce ophthalmologists' workload and detect hard exudates more accurately and efficiently, addressing the issue of low accuracy and efficiency in most existing hard exudate detection systems. The suggested approach belongs to the CNN category, which employs numerous input features as input and combines them with upgraded structures and particular information to dramatically improve EMFN performance. The EMFN has the capability to reduce redundancy by incorporating RAM into the proposed network, improve target-related information, and fully utilize the correlation between various channels and their locations. EMFN can skip several processing steps compared to previous methods, and reduce the effect of subjective factors. The proposed EMFN was evaluated on the MESSIDOR, HEI-MED and E-Ophtha EX datasets and achieves an accuracy of 93.00%, 94.00% and 92.00%, respectively. Prabhu et al. [358], proposed a supervised method for exudate classification with deep learning neural network. A large number of sub-images for each image have been trained to work in the network, around 48,000, which are then fed to the deep network as inputs. The original image was pre-processed before extracting the patches. The proposed method achieves an accuracy, specificity, AUC, and sensitivity of 98.67%, 98.76%, 97.29%, and 72.26% respectively on the e-Ophtha EX dataset. Wang et al. [359], presented an optimized new morphological mathematical approach that accurately distinguishes HE applicants in first segments. Then the combined features based on deep features with incorporated HCFs are characterized to each candidate, implemented by a ridge regression-based feature fusion. This method uses a multi-space intensity feature, geometrical features and gray-level texture descriptor based on the co-occurrence matrix (GLCM), gray level size zone matrix (GLSZM) to build HCFs, and a DCNN to learn the HE information automatically. Ultimately a random forest algorithm is used to classify candidates' true HEs. The proposed method achieves a sensitivity of 89.90%/94.77% and PPV 88.68%/91.79% on e-Ophtha/HEI-MED datasets, respectively.

7.4. Hemorrhages

There are various approaches and techniques for Hemorrhage segmentation. These approaches are divided into two types, i.e. unsupervised methods and supervised approaches. In this section, a detailed review of different unsupervised and supervised Hemorrhage approaches is presented. Tables 10 and 11 provide the performance metrics of the supervised and unsupervised approaches with the evaluation criteria, dataset, and publication year respectively. Fig. 11 illustrate the chronological summary of the recent hemorrhages segmentation methods.

7.4.1. Unsupervised methods

Lahmiri et al. [363], developed a fully automated retinal image hemorrhage detection system. Variational mode decomposition (VMD) was employed in the first stage of this procedure to obtain the first variation mode that captures high-frequency images. In the second stage, the first variation mode is employed to extract four texture descriptors. Finally, a trained classifier used all calculated texture descriptors to distinguish between healthy and unhealthy retinas with

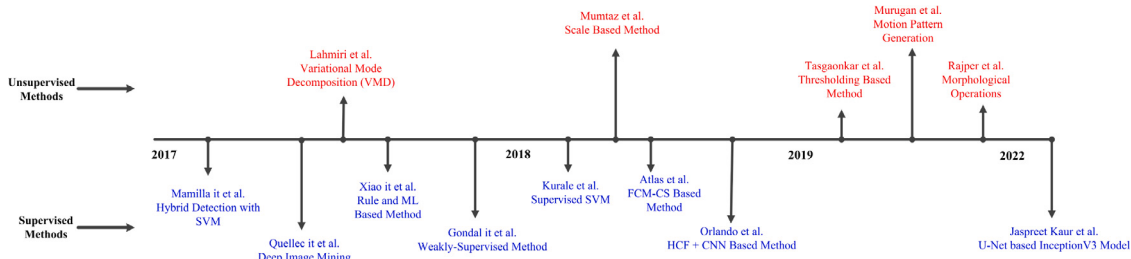


Fig. 11. Chronological summary of the recent hemorrhages segmentation methods.

Table 10

Performance Measures of Unsupervised Methods for Hemorrhage Extraction: Year wise best results on different datasets are highlighted with different colors i.e.(Green color for STARE, Violet color for DIARETDB1, and Brown color is for MESSIDOR dataset).

Year	Author	Method	Dataset	Performance measures in (%)		
				Accuracy	Sensitivity	Specificity
2017	Lahmiri et al. [363]	Variational Mode Decomposition (VMD)	STARE	100.00	100.00	100.00
2018	Mumtaz et al. [364]	Scale based method	DIARETDB1	89.00	87.00	84.00
	Tasgaonkar et al. [365]	Thresholding based method	DIARETDB1	98.09	98.86	99.78
2019	Murugan et al. [366]	Motion Pattern Generation	MESSIDOR	N.A	97.00	98.00
	Rajper et al. [367]	Morphological Operations	DIARTDB1	92.65	96.81	89.77

hemorrhages. The testing findings demonstrated the efficacy of the suggested retinal bleeding detection system, with a flawless detection rate. On the STARE database, the proposed technique achieved 100% accuracy, 100% sensitivity, and 100% specificity. Mumtaz et al. [364], represented the automatic detection of hemorrhage, one of the red lesions. The proposed method begins by improving image quality by reducing background noise and irregular illumination. It is possible to use systems to enhance image contrast and normalize it. The next stage is to use a scale-based method to distinguish blood vessels from hemorrhages, as both have the same hue. The hemorrhages are then delineated using gamma correction and global threshold approaches. On the DIARETDB1 database, the proposed technique achieved an accuracy of 89.00%, a sensitivity of 87.00%, and a specificity of 84.00%.

Tasgaonkar et al. [365], have captured the irregularity as a hemorrhage feature. Authors defined segmented region profile and use its centralized moments as a novel feature. For classification the Support Vector Machine and its variants were explored in the proposed method. The experimental tests showed promising results at R-channel profile moments. The accuracy of 98.09%, 100% was achieved with lesion level and with RBF SVM at image level, respectively. Overall, the proposed method has achieved an accuracy of 98.09%, sensitivity of 98.86% and a specificity of 99.78% on the DIARETDB1 database. Murugan et al. [366], proposed a technique for automatic detection of HE. This proposed technique uses an efficient algorithm for generating motion patterns to detect HE. The method's novelty is to reduce dimensional space based on image resolutions, thereby enhancing HE detection speed. The proposed method was tested on both ordinary and rare retinal images and achieved a sensitivity of 97.00% and a specificity of 98.00% on a publicly accessible MESSIDOR dataset. Rajper et al. [367] used morphological operations to remove blood vessels and detect hemorrhage from retinal fundus images. Statistical features (including standard deviation, energy, entropy and image contrast) were extracted and then segmentation methods are used to find hemorrhage and its severity. After the detection of features, blood vessels and hemorrhage were detected with help of morphological operations based segmentation technique. The proposed method was evaluated on DIARTDB1 dataset and achieved a sensitivity of 96.81%, a specificity of 89.77% and an accuracy of 92.65% respectively.

7.4.2. Supervised methods

Mamilla et al. [368], developed a new hybrid red lesion detection a system that employs both mathematical morphology and methods

based on phase congruency to discover candidate red lesions. The key contribution of this research was the use of an extended 2D log Gabor filter to assess phase congruence. Pre-processing polynomial contrast enhancement, hybrid detection for coarse candidate red lesion extraction, and SVM classifier for fine red lesion segmentation are the three steps of the proposed red lesion detection system. The proposed technique had a 99.69% accuracy, 99.30% sensitivity, and 99.20% specificity on the DIARET1 database.

Quellec et al. [369], suggested a method for generating heatmaps that highlight which pixels in a image are important for image-level predictions. In other words, a ConvNet that has been trained to detect lesions may also be used to detect image-level categorization. To train ConvNets that create high-quality heatmaps, a generalization of the back-propagation method is proposed. The proposed approach is applied to a dataset of over 90,000 fundus photos from the 2015 Kaggle diabetic retinopathy competition, as well as a private dataset of nearly 110,000 images to screen for diabetic retinopathy (e-ophthas). For DR detection task a very good detection performance was achieved on Kaggle and e-ophtha dataset. The proposed method has achieved an area under curve (AUC) of 95.50% and 94.90% on Kaggle and e-ophtha dataset, respectively.

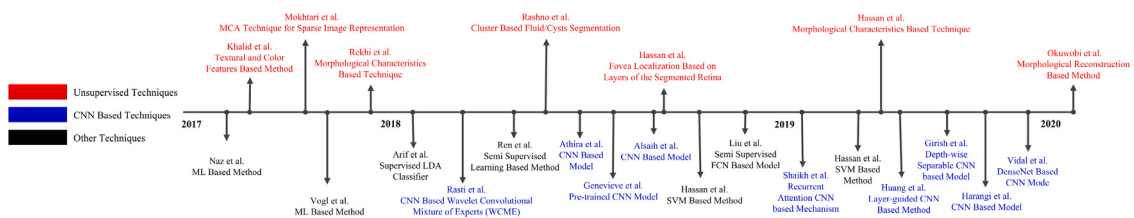
Xiao et al. [370], suggested a novel bleeding detection approach based on rule-based and machine learning. The authors focused on enhancing the identification of hemorrhages that are related or adjacent to retinal blood vessels, in addition to detecting separate hemorrhage regions. The suggested technique was tested on two datasets, and it achieved a sensitivity of 93.30% /91.90% and a specificity of 88.00% /85.60% on DiaRetDB1 and Local DRS camera-based datasets, respectively. To aid in medical diagnosis, Gondal et al. [371] proposed a deep learning strategy that emphasizes regions on retinal images that are indicative of DR. The suggested architecture was inspired by a recent top-performing supervised CNN architecture for DR classification, but it was tweaked to allow for object localization with minimal supervision. The authors exhibited precise localization with good sensitivity while maintaining high classification accuracy. On the DIARETDB1 database, the proposed technique had a sensitivity of 93.60%, a specificity of 97.20%, and an AUC of 95.40%.

Kurale et al. [372], proposed a new algorithm for the effective detection of hemorrhages. First, the important factor is preprocessing for better results, such as removal of edge effects and enhancement of contrasts, etc. This algorithm produces partitions into segments of the retinal image that is called as splats of the same color, intensity and

Table 11

Performance Measures of Supervised Methods for Hemorrhage Extraction: Year wise best results on different datasets are highlighted with different colors i.e.(Blue color for E-Ophtha, Maroon color for IDRiD, Violet color for DIARETDB1, and Brown color is for MESSIDOR dataset).

Year	Paper no.	Method	Dataset	Performance measures in (%)			
				Accuracy	Sensitivity	Specificity	AUC
2017	Mamilla et al. [368]	Hybrid Detection with SVM	DIARETDB1	99.69	99.30	99.20	N.A
	Quellec et al. [369]	Deep Image Mining	Kaggle	N.A	N.A	N.A	95.50
	Xiao et al. [370]	Rule and ML based method	DIARETDB1	N.A	N.A	N.A	94.90
	Gondal et al. [371]	Weakly-Supervised method	Local DRS Camera	93.30	88.00	85.60	N.A
2018	Kurale et al. [372]	Supervised SVM	MESSIDOR	88.00	N.A	N.A	89.00
	Atlas it et al. [373]	FCM-CS Based Method	MESSIDOR	97.50	87.36	91.36	N.A
	Orlando et al. [374]	HCF + CNN based method	E-Ophtha	N.A	97.21	N.A	93.87
2022	Jaspreet Kaur et al. [360]	U-Net based InceptionV3 Model	IDRiD	99.82	88.39	99.94	N.A

**Fig. 12.** Chronological summary of the recent macular edema segmentation methods.

spatial location. Each splat contains different information that allows us to extract different features from. These segments, i.e. splat, establish a set of information that extracts suitable boundaries. From all extracted features, we select some important features such as different filters, area, color, texture and splat related features etc. For the detection of the disease a trained supervised SVM classifier was used. The performance of the proposed method was tested on Messidor dataset and the proposed method achieves an accuracy of 88.00% and AUC of 89.00%.

Atlas et al. [373], proposed to build up the retinal discharge fundus images using the method for pre-processing, extraction of features, classification and segmentation using different strategies and methods. The affected and non-affected images are separated correctly by using ANFIS and the affected images are segmented by FCM-CS method of optimization. The accuracy, sensitivity, specificity, FAR and FRR for that segmented images are broken down. The proposed method has achieved an accuracy of 97.50%, sensitivity of 87.36% and a specificity of 91.36% on the MESSIDOR database. Orlando et al. [374], proposed a novel red lesion detection approach based on integrating both domain knowledge and deeply learned knowledge. Features learned from a CNN are enhanced by the incorporation of hand-crafted features. Such ensemble descriptor vector was then used to classify true candidates for lesions using a Random Forest classifier. Authors also found empirically that the use of both types of knowledge significantly increases the results with respect to the independent use of each method. Furthermore, the proposed method has achieved an area under curve (AUC) of 93.87% and 90.31% on MESSIDOR and e-ophtha dataset, respectively.

7.5. Macular edema

There are various approaches and techniques for Macular Edema segmentation. These approaches are divided into two types, i.e. unsupervised methods and supervised approaches. In this section, a detailed review of different unsupervised and supervised Macular Edema approaches is presented. Tables 12 and 13 provide the performance metrics of the supervised and unsupervised approaches with the evaluation criteria, dataset, and publication year respectively.

Fig. 12 illustrate the chronological summary of the recent macular edema segmentation methods.

7.5.1. Unsupervised methods

Khalid et al. [375], proposed a technique that automatically extracts macular region from input image, and then analyzes macular region texture to recognize irregular macula. A novel hybrid feature set was proposed which consists of different textural and color features. The experiments are performed using publicly accessible STARE and AFIO databases. The proposed method achieved a sensitivity of 97.50% / 98.00%, a specificity of 83.00% / 92.00% and an accuracy of 95.52% / 94.31% on STARE/AFIO datasets, respectively.

By detecting the singularities of the point and curving in each B-scan in their investigation, Mokhtari et al. [376] tied to distinguish HF from other objects. The decomposition approach provided here is based on the MCA technique for sparse image representation of B scans. Two overfitted dictionaries reflecting two different characteristics of the B-scans were produced using the transformed curve and the Daubechies wavelet foundation. The HFs stand out more in re-built images with wavelet dictionaries, and the curvelet dictionary often detects other objects. HFs could therefore be identified using an appropriate threshold criterion with wavelet atoms on the reconstructed image. Eventually, the false positives are reduced by removing the candidate points in RNFL and RPE layers, which are segmented automatically based on ridgelet transformation. The simulation results of the proposed work on 1924 HFs showed a sensitivity and accuracy of 91.00% and 100% to HF detection, respectively.

Rekhi et al. [377], proposed to use a robust method to detect macula using morphological characteristics and to measure segmented exudates against specially developed regions around the macula. The algorithm further grades the image according to the severity of the disease. The performance of the proposed algorithm was tested on DIARETDB1 database and achieves an accuracy of 92.11% in the detection of severe DME case and an accuracy of 90.00% for the same when tested on MESSIDOR database.

Rashno et al. [378], introduced a new method for calculating the indeterminacy set I, and a new operation of λ correction for calculating the set T in neutrosophic domain. Furthermore, a graphical shortest-range approach is used as regions of interest (ROI) and outer plexiform layers (OPL) in neutrosophic domains, and the middle segment myeloid (ISM) in intermediate layers with a new concept of edge weights for retinal images. Thirdly, the new cost function is

Table 12

Performance Measures of Unsupervised Methods for Macular Edema: Year wise best results on different datasets are highlighted with different colors i.e.(Green color for STARE, Pink color for AFIO, Violet color for DIARETDB1, Orange color is for BIOMISA, and Brown color is for MESSIDOR dataset).

Year	Author	Method	Dataset	Image type	Performance measures in (%)		
					Accuracy	Sensitivity	Specificity
2017	Khalid et al. [375],	Textural and color features based method	STARE	–	95.52	97.50	83.00
	Mokhtari et al. [376]	MCA Technique for Sparse Image Representation		AFIO	94.31	98.00	92.00
	Rekhi et al. [377]	Morphological Characteristics Based Technique		–	N.A	91.00	100.00
	DIARETDB1	Normal	DIARETDB1	Normal	95.45	N.A	N.A
		Severe DME		Severe DME	92.11	N.A	N.A
		Moderate DME		Moderate DME	87.50	N.A	N.A
		Normal	MESSIDOR	Normal	92.72	N.A	N.A
		Severe DME		Severe DME	90.00	N.A	N.A
		Moderate DME		Moderate DME	88.89	N.A	N.A
2018	Rashno et al. [378]	Cluster Based Fluid/Cysts Segmentation	Optima	–	N.A	89.34	74.62
2018	Hassan et al. [379]	Fovea Localization Based on Layers of the Segmented Retina		ME	97.50	N.A	N.A
2019	Hassan et al. [380]	Morphological Characteristics Based Technique	BIOMISA	–	95.00	100.00	93.33
2020	Okuwobi et al. [381]	Morphological reconstruction based method	–	–	DSC = 71.30%	Correlation coefficient = 99%	

introduced in the ROI segmentation of cluster-based fluid/cysts, which also involves a new method to automatically estimate the number of clusters. Fourth, by ignoring very small areas and regions between mid-layers, the final fluid regions are achieved. The suggested method was assessed using two publicly available Duke and Optima datasets. The proposed method achieved a sensitivity of 89.34%, a specificity of 74.62% on Optima dataset.

Hassan et al. [379] introduced an automatic fovea localization algorithm in this article. The proposed algorithm was based upon the layers of the segmented retina. After segmenting the retina layers, the thickness profile for foveal localization was determined between NFL and ONL layer. Authors used three different retinal pathologies to test their algorithm and in fovea detection it achieved the overall accuracy of 97.50%. Hassan et al. [380], developed a completely automated approach for classifying macular edema utilizing both retina imaging modalities (fundus and OCT). The proposed method worked by first extracting the thickness of the retina layer and then segmenting the cystic areas using OCT and fundus images as input. The retrieved profiles are then converted into a 5D feature vector, which is fed into the supervised discriminant analysis (DA) classifier. The proposed method was based on 71 OCT and 71 fundus scans of 60 patients, 15 of whom had ME and 45 of whom were healthy. The proposed method correctly identified 100% of ME cases and 93.33% of healthy subjects.

Okuwobi et al. [381], proposed an algorithm that consists of two parallel processes, namely: generation of region of interest (ROI), and estimation of HFs. Authors used morphological reconstruction (MR) to generate the ROI to obtain the reconstructed image and histogram constructed for distribution and clustering of the data. Parallel to this authors estimated the HFs by removing the extreme regions from the related regions obtained from a tree of components. Finally, the segmented HFs are created by combining the ROI and HFs estimation processes. On 40 3D SD-OCT volumes, the proposed technique was validated using data from 40 patients with nonproliferative diabetic retinopathy (NPDR), proliferative diabetic retinopathy (PDR), and diabetic macular edema (DME). The average dice similarity coefficient (DSC) and correlation coefficient (r) for NPDR 70.31%, 99.00% for PDR 71.30%, 99.00% for DME are 69.70% and 99.00%, respectively.

7.5.2. Supervised methods

The unsupervised techniques are further grouped into CNN-based techniques and other techniques.

A. CNN-based techniques. Rasti et al. [382], presented a new fully automatic algorithm for classifying 3D OCT images as Age-related macular degeneration (AMD), diabetic macular edema (DME), and healthy people. No retinal layer alignment or segmentation (for example, segmentation of in-retinal layers and lesion structures) was needed for the

proposed algorithm. As an adaptive method of extraction and classification, this algorithm uses a new Wavelet-based Convolutional Mixture of Experts (WCME). The WCME profits from the decomposition of spatial frequency and also a series of CNNs to provide a high degree of OCT data representation. A retinal OCT dataset consisting of 148 cases was used for evaluation of the proposed method. The dataset consists of 50 DME, 50 normal, and 48 Heidelberg-device AMD OCT acquisitions. The proposed method achieves a sensitivity, specificity, AUC and F1 Score of 94.63%, 95.21%, 98.60% and 94.58%, respectively. Athira et al. [383] primarily focused on creating a computerized system for detecting and diagnosing ME at its earlier stages. For ME detection and classification the proposed system uses graph-based segmentation, SFTA, and QDA algorithms. The database was compiled by Heidelberg Engineering Inc. From this 100 regular and 100 macular edema images are taken for classification and detection. The ophthalmologist can easily identify the ME and treat patients with a high degree of accuracy of 97.50% at their earlier stages. Genevieve et al. [384], demonstrated the application of a pre-trained CNN model for the categorization of Diabetic Macular Edema (DME) images using Spectral Domain Optical Coherence Tomography (SD-OCT) with feature reduction using Principal Component Analysis (PCA) and Bag of Words (BoW). The network was trained using the Singapore Eye Research Institute (SERI) SD-OCT dataset and tested using an 8-fold slide-level cross-validation with two patients omitted at the volume level. The volume point had a precision of 96.88% when preprocessed data was used. Alsaih et al. [385], proposed an automated technique for detecting retinal cysts on volumes in the Spectral Domain OCT (SD-OCT). The suggested approach takes into account a standardized classification pipeline that extracts the stable regions and then compares the stable regions with the ideal ground truth to mark the possible regions. After that the possible regions were resized and sent to the auto encoder in an unsupervised fashion to extract the features. Finally, the trained data was classified in a supervised fashion using the softmax layer, and the test data is passed over the network to validate the results. The suggested pipeline has obtained a specificity of 82.0% and sensitivity of 93.0%.

Shaikh et al. [393], represented a minuscule proportion of pixels that presents the lesions, and resizing may result in information loss. Recurrent attention mechanism based network aid to reduce overhead processing when conducting convolutional operations on high resolution images. The proposed technique was tested on two distinct classification tasks, i.e., classifying brain tumors from magnetic resonance images and predicting the severity of macular diabetic edema from fundus images. The proposed methodology achieved 97.00% accuracy for the former task ($n = 300$). Due to a large number of parameters, deep CNN models have high computational complexity, Girish et al. [396] suggested an approach of depth-wise separable convolutional filters aids model generalizability and prevents model

Table 13

Performance Measures of Supervised Methods for Macular Edema: Year wise best results on different datasets are highlighted with different colors i.e.(Maroon color for IDRiD, Sea Green color for SERI, Indigo color for DUKE-DME, Orange color is for BIOMISA, and Brown color is for MESSIDOR dataset).

Year	Author	Method	Dataset	Feature	Performance measures in (%)				
					Accuracy	Sensitivity	Specificity	AUC	F1 score
2017	Naz et al. [386]	ML based method	Duke DME	–	79.25	93.30	100.00	N.A	N.A
	Vogl et al. [387]	ML based method		BRVO	N.A	77.00	82.00	83.00	N.A
				CRVO	N.A	67.00	84.00	79.00	N.A
2018	Arif et al. [388]	Supervised LDA Classifier	MESSIDOR	–	95.93	100.00	91.86	N.A	N.A
	Ren et al. [389]	Semi Supervised Learning based method		–	97.50	94.60	98.20	N.A	94.20
	Rasti et al. [382]	CNN Based Wavelet Convolutional Mixture of Experts (WCME)		–	–	N.A	94.63	95.21	98.60
	Athira et al. [383]	CNN based model	Heidelberg Engineering Inc.	–	97.50	98.90	98.05	N.A	N.A
	Genevieve et al. [384]	Pre-trained CNN Model	SERI	–	96.88	93.75	100.00	N.A	N.A
2019	Alsaikh et al. [385]	CNN based model	–	–	0.00	93.00	82.00	N.A	N.A
	Hassan et al. [390]	SVM based method	–	–	97.78	96.77	100.00	N.A	N.A
	Syed et al. [391]	SVM based method	MESSIDOR	–	94.13	96.23	95.04	N.A	N.A
	Liu et al. [392]	Semi Supervised FCN based model	Duke DME	–	N.A	N.A	N.A	N.A	95.20
	Shaikh et al. [393]	Recurrent Attention CNN based Mechanism	IDRiD	–	97.00	N.A	N.A	N.A	N.A
	Hassan et al. [394]	SVM based method	BIOMISA	–	97.78	96.77	100.00	N.A	N.A
	Huang et al. [395]	layer-guided cnn based method	UCSD	–	95.40	85.70	96.80	N.A	N.A
2020	Girish et al. [396]	Depth-wise separable CNN based model	OCSC	–	N.A	65.00	86.00	Dice coefficient = 72.00%	
	Harangi et al. [397]	CNN based model	IDRiD	–	90.07	N.A	N.A	N.A	N.A
	Vidal et al. [398]	DenseNet based CNN model	ISBI challenge	–	96.85	N.A	N.A	N.A	N.A
			CIRRUS	–	97.48	N.A	N.A	99.61	N.A
			HDN.AOCT						

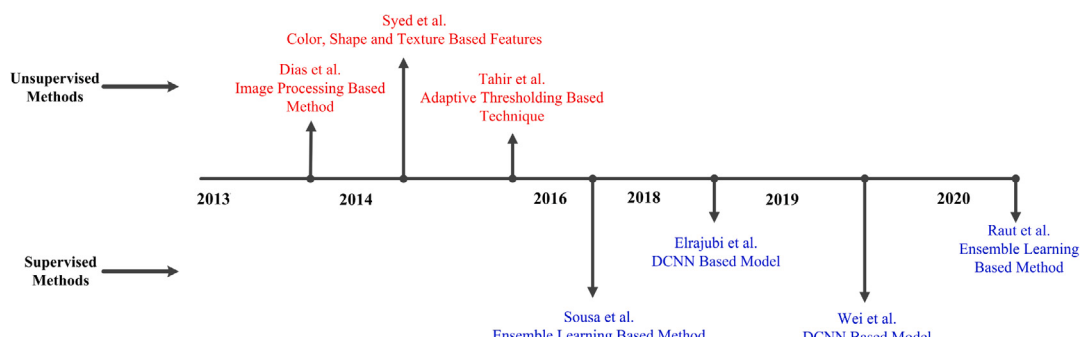


Fig. 13. Chronological summary of the recent laser scars segmentation methods. Red color shows the unsupervised methods and Blue color shows the supervised method.

overfitting. In addition, the swish activation function was used to keep the gradient from disappearing. The suggested model was tested with four different vendor OCT system scans from the optima cyst segmentation challenge (OCSC) dataset. The proposed technique yields 65.00% sensitivity, 86.00% specificity, and 72.00% dice coefficient, respectively. Harangi et al. [397] offered a study that combined a CNN with traditional hand-crafted features to create a single retinal image categorization architecture. This method enables a final prediction to be made by combining CNN training and fine-tuning the weights of hand-crafted features. The proposed solution was dedicated to automatically classifying fundus images according to the DR and DME severity levels. The proposed method was evaluated on IDRiD and ISBI challenge and achieves an accuracy of 90.07% and 96.85%, respectively. Vidal et al. [398], suggested the usage of DenseNet architecture to perform regional analysis instead of classical approaches like machine learning, and use it to depict pathological identifications with an informative color map. The proposed method learned, validated, and checked the DenseNet with a dataset consisting of 3247 samples labeled by a specialist. They were derived from 156 photographs that were taken with two of the domain's key OCT devices. Then, the OCT images used this network to create the color map representations of the cystoid areas. The proposed method has obtained an accuracy and AUC of 97.48% and 99.61%, respectively.

B. Other techniques. Naz et al. [386], proposed a simple and practical technique for using coherent tensors to exploit the information in OCT images for a robust classification of Diabetic Macular Edema (DME). Top and bottom layers are separated from the retinal OCT scan to find thickness profile. Also cyst spaces are segmented out of normal and DME images. The features extracted from the thickness profile and cyst are tested on Duke Dataset with 55 diseased and 53 regular OCT scans. The proposed technique achieves an accuracy, sensitivity and specificity of 79.25%, 93.30% and 100.00%, respectively. Sparse logistic regression and extra trees (ET) based on Random Forests were introduced and analyzed by Vogl et al. [387], as two different data-driven machine learning algorithms working in a high-dimensional feature space. . The author's developed Spatio-temporal signatures based on retinal thickness features recorded in images data for longitudinal spectral-domain optical coherence tomography (OCT) and used these quantitative features to predict individual patient outcomes. On a dataset of monthly SD-OCT scans of 155 patients with central retinal vein occlusion (CRVO) and 92 patients with branch retinal vein occlusion (BRVO) followed for over a year, the proposed method demonstrated that we can predict whether the treated disease will recur during the covered interval based on the first three observations. ET forecasts an AUC of 83.00% and 76.00% for BRVO and CRVO a 5-fold cross-validation result. Arif et al. [388], proposed a fully integrated clinical decision support system for the automatic diagnosis of RE

pathology from OCT images. The proposed system perform classification task by using a supervised LDA classifier. The prosed system used 75 OCT images of 62 patients with 14 individuals having RE and 48 being healthy subjects. 91.86% of healthy and 100% of diseased subjects were classified by the proposed system. Ren et al. [389], proposed a method in which macula is localized first by using its anatomical features and macula-positioning information about the optical disk. Second, a novel approach is proposed for the identification of exudates. Using vector quantization technique the potential exudate regions are segmented and formulated using a set of feature vectors. To define the true exudates a semi-supervised learning with graph-based classifier was used. Third, the severity of the disease is graded into various stages depending on the location of exudates and the coordinates of the macula. The proposed approach was validated on MESSIDOR dataset and has obtained an accuracy, sensitivity, F1 Score, and specificity of 97.50%, 94.60%, 94.20%, and 98.20%, respectively. Hassan et al. [390], presented a novel structure tensor graph searches (ST-GS) based segmentation method incorporating structure tensor and graph theory to extract retinal and choroidal layers along with fluid pores accompanied by automated 3D retinal surface reconstruction. Even from highly degraded OCT scans ST-GS can extract retinal information. The proposed method achieves an accuracy of 97.78%, sensitivity of 96.77% and Specificity of 100.00%. Syed et al. [391], presented an automatic ME detection system from fundus images. Using knowledge of exudates and maculae, an automated system for the detailed grading of disease severity was introduced. A new collection of features were used for accurate location of the fovea along with a minimum distance classifier, which is critical for ME gradation. The proposed system used various hybrid features and supports vector machines for exudate segmentation. The comprehensive classification of ME as both clinically important ME and non-clinically meaningful ME is performed using located foveae and segmented exudates. The algorithm proposed is validated using both public and local datasets. The proposed method achieved an average 94.13% of accuracy, 96.23% of sensitivity and 95.04% of specificity in the detection and grading of ME. Liu et al. [392], proposed a new fully convolutional semi-supervised deep learning method for segmenting retinal layers and fluid area in retinal OCT B -scans. The semi-supervised approach being proposed leverages unlabeled data through an adversarial learning strategy. The segmentation system involves a segment network and a discriminating network, all networks being u-net like architecture that is fully convolutional. The segment network's objective function is a combined loss function that involves multi-class cross entropy loss, adversarial loss, and semi-supervisory loss. The proposed method achieves a F1 score of 95.20% on DUKE dataset. Hassan et al. [394], proposed a novel method that first measures coherent OCT volume tensors were generated, and a 7D feature vector is created, with three features extracted from the profile of retinal thickness and four features extracted from the retinal fluids. SVM was trained on 30 OCT volumes (ten ME, ten CSR, and ten normal). Validation was based on a total of ninety OCT volumes from seventy-three patients (thirty normal, thirty CSR, and thirty ME). The proposed method achieved an accuracy, sensitivity and specificity of 97.78%, 96.77% and 100.00%, respectively. Huang et al. [395], presented the retinal OCT image classification with a layer-guided convolutional neural network named LGCNN. LGCNN used the correlation between macular pathologies and the specific retinal layers as compared to several typical methods. Specifically, ReLayNet first developed the maps for layer segmentation and extracted two probability maps related to lesion layer. The LGCNN was then employed to integrate the classification information related to lesion layers. Two subnetworks in LGCNN were explicitly designed for lesion related layers, taking into account the characteristics of different layers, which were very effective for the final classification. The proposed method achieves an accuracy, sensitivity and Specificity of 95.40%, 85.70% and 96.80% for UCSD dataset and 94.30%, 95.30% and 93.20% for HUCM dataset respectively.

7.6. Laser scars

There are various approaches and techniques for laser scars segmentation. These approaches are divided into two types, i.e. un-supervised methods and supervised approaches. In this section, a detailed review of different unsupervised and supervised laser scars approaches is presented. Tables 14 and 15 provide the performance metrics of the supervised and unsupervised approaches with the evaluation criteria, dataset, and publication year respectively. Fig. 13 illustrate the chronological summary of the recent laser scars segmentation methods.

7.6.1. Unsupervised methods

Dias et al. [399] make an initial attempt to create a binary classifier with a collection of features of color, focus, contrast and illumination. On a dataset consisting of 40 fundus images with laser scars and 176 fundus images without laser scars, a 5-fold cross-validation experiment is carried out. The proposed system achieves 63.37%, 99.90% and 96.97%, respectively, sensitivity,specificity and PPV.

Syed et al. [400] manipulated color, shape and texture-based features by performing their experiments on a locally collected dataset of 380 images, 51 of which have laser scars. The proposed system achieved 94.00%, 97.00% and 96.00%, sensitivity, specificity and accuracy, respectively. Tahir et al. [401], presented a simple, straightforward but effective technique for detecting laser scars. The key motivation is to promote automatic diagnostic methods due to these laser marks, and to prevent false detection of irregular regions. The proposed method used contrast enhancement and adaptive thresholding technique to remove all possible regions which could be considered as laser marks. The true regions of the laser label are determined using a minimum distance classifier and a number of features. The proposed system achieves sensitivity, specificity and accuracy of 94.00%, 97.00% and 96.00% respectively.

7.6.2. Supervised methods

Sousa et al. [402], proposed to extract features based on geometry, texture, spatial distribution and intensity, and train a decision tree and a random forest as their laser scar detectors. A common drawback of the above approaches is their reliance on hand-crafted features that are often not well generalized. Extracting hand-crafted features involves specifying a number of ad-hoc (and implicit) parameters, making it extremely difficult, if not impossible, to replicate previous methods. The proposed system achieves sensitivity, specificity and PPV of 88.10%, 98.90% and 86.90% respectively.

Elrajubi et al. [403], proposed a retinal image classifier based on Convolutional Neural Networks, a popular deep learning method. This model uses texture-based features to evaluate whether an input image contains evidence of prior photocoagulation laser treatments. On the other side, this classifier could aid the human expert in examining the case, making the procedure easier and faster. The proposed technique, as well as the datasets used in its preparation and evaluation, are thoroughly addressed. The proposed technique achieves a 90.00% accuracy.

In this modern environment, Wei et al. [404] investigated major design decisions of state-of-the-art CNNs such as Inception-v3, ResNet, and DenseNet. Transfer learning, in which trained weights of ImageNet models are passed on to their counterparts with laser-scars for more successful training, was used by the authors. Experiments on the new dataset show that best proposed model detects laser-scar images with 96.20% sensitivity, 99.90% specificity, 97.40% precision and 98.80% AP accuracy and 99.90% AUC. On the public LMD-BAPT dataset, the same model was evaluated, achieved sensitivity of 76.50%, specificity of 100%, precision of 100%, AP of 97.50% and AUC of 99.10%, outperformed the state-of-the-art by a great margin. Raut et al. [405], proposed a novel retinal history characterization technique that examines the potential of discrete wavelet transformation and

Table 14

Performance Measures of Unsupervised Methods for Laser Scars Extraction: Year wise best results are marked as bold.

Year	Authors	Method	Dataset	Performance measures in (%)			
				Accuracy	Sensitivity	Specificity	PPV
2013	Dias et al. [399]	Image processing based method	Local	N.A	63.37	99.90	96.97
2014	Syed et al. [400]	Color, Shape and Texture Based Features	Local	96.00	94.00	98.00	N.A
	Tahir et al. [401]	Adaptive Thresholding Based Technique	Local	96.50	95.00	97.00	N.A

Table 15

Performance Measures of Supervised Methods for Laser Scars Extraction: Year wise best results on different datasets are highlighted with different colors i.e.(Olive color for LMD dataset).

Year	Authors	Method	Dataset	Performance measures in (%)				
				Accuracy	Sensitivity	Specificity	AUC	PPV
2016	Sousa et al. [402]	Ensemble learning based method	LMD (DSR+BAPT)	N.A	88.1	98.9	N.A	86.9
2018	Elrajubi et al. [403]	DCNN based model	AIBILI	91.65	N.A	N.A	N.A	N.A
2019	Wei et al. [404]	DCNN based model	LMD-BAPT	N.A	76.5	100	99.1	0
2020	Raut et al. [405]	Ensemble learning based method	LMD	86.7	87.5	89.4	N.A	N.A

Table 16

Performance Measures of Unsupervised Methods for AV Nicking: Year wise best results on different datasets are highlighted with different colors i.e.(Red color for DRIVE, Salmon color for VICAVR, Teal color for INSPIRE-AVR, and Golden color for SiMES dataset).

Year	Authors	Method	Dataset	Performance measures in (%)			
				Accuracy	Sensitivity	Specificity	AUC
2013	Bhuiyan et al. [406]	Image processing	SiMES	96.23	N.A	N.A	N.A
	Nguyen et al. [407]	Image processing	SiMES	89.00	N.A	N.A	95.00
2014	Dashtbozorg et al. [408]	Graph based approach	INSPIRE-AVR	88.30	N.A	N.A	N.A
			DRIVE	87.40	N.A	N.A	N.A
	Roy et al. [409]		VICAVR	89.80	N.A	N.A	N.A
2016	Kang et al. [410]	Image processing	SiMES	64.51	N.A	N.A	N.A
	Huang et al. [411]	Feature based approach	Local	87.50	N.A	N.A	N.A
			INSPIRE-AVR	85.10	N.A	N.A	87.00
			VICAVR	90.60	N.A	N.A	95.00
			NIDEK	86.90	N.A	N.A	84.00

rotational-invariant variance features for retinal image texture classification with and without laser marks. Different classifiers are evaluated for this experiment, namely SVM, naive Bayes, neural network, and random forest classifiers. Two publicly available datasets LMD-DRS and LMD-BAPT were used for performance evaluation of the proposed technique. In all situations, the proposed solution obtained values of sensitivity, precision, and accuracy of 68.9%, 70.2%, and 69.4%, respectively. It was found that for the classification task, all performance measurements achieve more than 87.5%, 89.4% and 86.7% using a random forest classifier.

7.7. AV nicking

AV nicking, also known as AV nipping, is an anomaly in the retinal microvascular structure that shows the features of crossing a tiny artery over a vein during ophthalmological imaging. Because of this crossing of the arteries and veins, either side of the artery cross-section point inflates by the vein. In several forms of retinal imaging study, AV nicking has been recognized as an early indicator of eye-related disorders such as diabetes, BRVO, hypertension, and acute stroke. In this section, a detailed review of different unsupervised and supervised AV Nicking approaches is presented. Tables 16 and 17 provide the performance metrics of the supervised and unsupervised approaches with the evaluation criteria, dataset, and publication year respectively. Fig. 14 illustrate the chronological summary of the recent AV nicking segmentation methods.

7.7.1. Unsupervised methods

Bhuiyan et al. [406], proposed a new method for measuring the caliber of the retinal vessel, which is a “edge-based” method of tracking the vessels. Authors calculated CRAE and CRVE for any type of

vessel. The proposed method achieved a very high accuracy (average 96.23%) compared to manually graded width for every cross-sectional width measure. For CRAE and CRVE’s overall vessel caliber measurement accuracy, authors have compared the results with an existing semi-automatic method which showed high correlation of 85.00% and 92.00%, respectively. The proposed method’s intra-grader reproducibility was high, with 88.10% for CRAE and 87.50% for CRVE as the correlation coefficient. Image processing techniques such as image capture, segmentation, and vessel width measurement method, and blood vessel classification method were used by Nguyen et al. [407] to offer a computer-based system for detecting AV nicking severity. The suggested technique was tested on 47 high-resolution fundus images from two distinct population-based investigations. The AV nicking values obtained in the experiments had a strong association with expert grading, and the suggested algorithm’s accuracy ranged from 88% to 89%, which clarifies that more accurate detection of severe and moderate AV nicking is possible.

Dashtbozorg et al. [408], proposed an automated approach to classifying A/V based on the analysis of a graph drawn from the vasculature of the retina. The proposed approach classifies the entire vascular tree defining the category of each point of intersection (graph nodes) and assigning one of two labels to each segment of the vessel (graph links). The final classification of a vessel segment as A/V was obtained by integrating the results of the graph-based labeling with a set of intensity features. The performance of the proposed technique was validated and obtained an accuracy of 88.3%, 87.4%, and 89.8% on publicly available the INSPIRE-AVR, the DRIVE, and the VICAVR databases.

Roy et al. [409], proposed an efficient method for determining the intensity degree of AV nicking by measuring the retinal venular widths. The authors calculated its widths using a combination of intensity and vein edge information. The crossover points are discovered using vessel

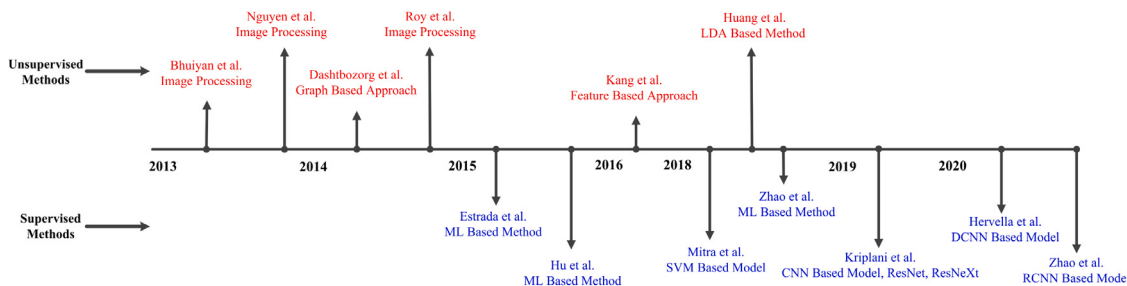


Fig. 14. Chronological summary of the recent AV nicking segmentation methods. Red color shows the unsupervised methods and Blue color shows the supervised method.

Table 17

Performance Measures of Supervised Methods for AV Nicking: Year wise best results on different datasets are highlighted with different colors i.e.(Red color for DRIVE, Green color for STARE, Salmon color for VICAVER, Teal color for INSPIRE-AVR, and Peach color for IOSTAR dataset).

Year	Author	Method	Dataset	Performance measures in (%)				
				Accuracy	Sensitivity	Specificity	Precision	F1 score
2015	Estrada et al. [412]	ML based method	WIDE	91.00	91.00	90.90	N.A	N.A
			AV-DRIVE	93.50	93.00	94.10	N.A	N.A
	Hu et al. [413]	ML based method	CT-DRIVE	91.70	91.70	91.70	N.A	N.A
			AV-INSPIRE	90.90	91.50	90.20	N.A	N.A
2018	Mitra et al. [414]	SVM based model	DRIVE	88.15	N.A	N.A	N.A	N.A
			INSPIRE-AVR	95.10	94.25	95.47	N.A	N.A
			VICAVER	95.64	94.58	95.83	N.A	N.A
	Zhao et al. [415]	ML based method	Local dataset (AVRDB)	98.09	98.34	97.96	N.A	N.A
			INSPIRE	91.00	91.80	90.20	N.A	N.A
2019	Kriplani et al. [416]	CNN based model, ResNet, ResNeXt	DRIVE	N.A	91.90	91.50	N.A	N.A
			VICAVER	91.00	N.A	N.A	N.A	N.A
	Hervella et al. [417]	DCNN based model	STARE	85.71	100.00	N.A	85.29	92.00
			DRIVE	95.93	92.27	97.42	N.A	74.23
2020	Zhao et al. [418]	RCNN Based Model	IOSTAR	95.59	90.57	97.70	N.A	70.90
	Hervella et al. [417]	DCNN based model	DRIVE	N.A	66.00	N.A	73.00	69.00
			IOSTAR	N.A	51.00	N.A	63.00	56.00

segmentation and centerline extraction, and the vessels in the crossing area are categorized into arteries and veins. For quantitative evaluation of the proposed method, 47 color retinal images from two population-based studies were processed in the proposed method, which resulted in a classification accuracy of 64.51%. Kang et al. [410], proposed an automated method for detecting arteriovenous nicking in the retinal images. The crossover points are identified by segmentation of the vessels and centerline extraction, and the vessels are divided into arteries and veins in the crossing area. Measurement of arteries and retrieval of vascular details were accomplished further. To increase the accuracy of the identification, voids, micro-vessels and fake branches were eliminated. The proposed method achieved 87.50% accuracy.

Huang et al. [411] showed that these methods of classification can be improved significantly. The proposed methods was a new standardization strategy to remove four additional features that are synonymous with reflecting vessels' lightness. To validate those features, the accuracy of a linear discriminate analysis classifier was used. Accuracy levels of 85.10%, 86.90% and 90.60% per cent were obtained using only local information on three datasets. The advanced graph-based methods will achieve a better performance on A/V classification based on the introduced features.

Pereira et al. [419], developed Another computerized system to detect the presence of AV nicking. The algorithm uses a line detector with several scales to segment the blood vessels. AV cross points detect the presence or absence of AV nicking and are defined with a support vector machine model. The method was used to differentiate apparent or serious cases from normal cases of AV nicking. The proposed system achieved an accuracy, sensitivity, specificity and AUC of 88.76%, 84.62%, 90.48% and 96.00%, respectively.

7.7.2. Supervised methods

Estrada et al. [412], proposed a graph-theoretical method for distinguishing arteries from veins. The study uses the underlying vascular architecture to better discriminate between small and medium-sized vessels. The authors built a simple but powerful global probability model by iteratively exploring the space of the possible solutions with the anticipated vessels, extending their previously published framework for tree topology estimation by incorporating expert, domain-specific information. The proposed method was evaluated on WIDE, AV-DRIVE, CT-DRIVE and AV-INSPIRE datasets and achieved an accuracy of 91.00%, 93.50%, 91.70%, 90.90%, a sensitivity of 91.00%, 93.00%, 91.70%, 91.50% and a specificity of 90.90%, 94.10%, 91.70%, 90.20%, respectively.

Hu et al. [413] provided a system for automatically generating venous and arterial vascular trees in retinal images. The suggested method restores vascular connectivity by establishing a tightly connected network and using a graph-based algorithm to separate the vessel network into anatomical trees, which were then classified into A/V trees for vessel segmentation. The proposed method restores vessel connectivity by constructing a strongly connected network and separating the vessel network into anatomical trees using a graph-based algorithm, which was then classified into A/V trees. The proposed technique was tested using a ground truth based on a public database, and it achieved an accuracy of 88.15% in pixel-wise classification.

Mitra et al. [414], proposed a framework that uses a collection of hybrid features for the Artery or Vein (A/V) classification using an arteriovenous ratio support vector machine (SVM) along with radial basis function (RBF) kernel. The proposed method achieved a sensitivity, accuracy, and specificity of 94.25%, 95.10%, and 95.47% on INSPIRE-AVR, 94.58%, 95.64%, and 95.83% on VICAVER and 98.34%,

98.09%, and 97.96% on a local dataset (AVRDB), respectively. Zhao et al. [415], presented a novel structure that can separate the vein from color fundus images. The suggested method successfully formalized the topology estimation of retinal vessels and the A/V classification problem as a pairwise clustering problem by using the idea of clustering dominant sets. The graph-theoretical technique of clustering dominating sets has been found to function effectively in data clustering. The proposed method was evaluated on three publicly available databases that include DRIVE, INSPIRE, and VICAVR and obtained high accuracy of 91.2%, 91.0%, and 91.0% respectively.

Kriplani et al. [416] described a deep learning based process to classify arteriovenous nicking using the patient's retinal images. STARE dataset was used as the training data and then classified by using the proposed model in the absence and presence of arteriovenous nicking. The CNN based proposed model achieves an accuracy, sensitivity, precision and F1 score of 85.71% 100.00%, 85.29% and 92.00%. The ResNet achieves 91.42%, 100.00%, 90.62% and 95.07% and ResNeXt achieves 94.28%, 100.00%, 93.54% and 96.66%, respectively.

Hervella et al. [417] formulated the identification of vessel crossings and bifurcations as a multi-instance heatmap regression in eye fundus images. In particular, the prediction of multi-instance heatmaps that model the likelihood of a pixel being a landmark location is trained in a deep neural network. This novel approach allows the use of full images to make predictions and combines the detection and differentiation of vascular landmarks in a single stage. The proposed method achieved an accuracy of 95.93%, 95.59%, a sensitivity of 92.27%, 90.57%, a specificity of 97.42%, 97.70% and a F1 score of 74.23%, 70.90% on two publicly available DRIVE and IOSTAR dataset, respectively.

Zhao et al. [418], proposed a two-stage pipeline for detecting and classifying the junction points. A RCNN-based Junction Proposal Network was used for the detection stage to check for possible bifurcation and crossover locations directly on retinal color fundus images, followed by a Junction Refinement Network to remove false detections. Using the proposed Junction Classification Network which shares the same model structure with the refinement network, the detected junction points are classified as crossover or bifurcation during the classification stage. The proposed approach achieves 66.00% and 51.00% sensitivity, 73.00% and 63.00% precision and 69.00% and 56.00% F1-score on DRIVE and IOSTAR dataset respectively.

8. Network parameters, training, and testing time

It is noted that the classical supervised methods failed because of the complexity of the images, and methods. Supervised methods require high-dimensional pixel-wise feature vectors to train the classifier that discriminates vessels from non-vessel pixels. These methods can fail due to the limited availability of data and unsuitable parameters. The small number of images can be trained and validated and demands special hardware such as high-speed computers or GPUs. Depending upon the complexity of the model, the time grows with an increasing number of dimensions, as more operations need to be performed. The speed is also reduced whenever larger images are processed the more and larger memory needs to be found to store the images. The training time is much greater and is not possible to perform training for larger images. To solve this issue, images are downsampled while compromising on the quality of the images or use high resources for a small increase in the performance of methods. People do not care about hardware resources which is not fair for people with limited resources. To deal with the issue, one solution is that to use small architecture while maintain the performance. A brief comparison of different architecture is presented in Table 18.

9. Discussions and conclusion

This section presents the summary of the foregoing survey and draws important conclusions. Retinal image acquisition is the first stage in analyzing and extracting characteristics from a retinal image. After acquiring the images of the retina, it goes through a number of processes, including image enhancement, image restoration, image construction, and image segmentation. These processes are used to evaluate specific objects of interest to determine more specific features and characteristics. There are a significant number of automatic qualitative and quantitative applications based on identified image processing techniques. These techniques can diagnose defects in the retinal vasculature, including blood vessels, OD/OC, exudates, hemorrhage, macular edema, laser scars, and AV Nicking. This article provides a comprehensive overview of the complete segmentation and classification system for retinal diseases.

9.1. Discussion

The survey conducted has covered all significant existing methods for retinal image analysis. These segmentation techniques have been classified as unsupervised and supervised learning-based methods. Supervised-based methods are those in which input and ground truth images indicate that a pixel is a feature (e.g., vessel, exudate, etc.) or that it is not included in the training set. Unsupervised learning is typically employed for clustering and anomaly detection tasks, since vessel segmentation does not require ground truth data. We have presented existing approaches for segmenting retinal features along with the datasets used, publication year, and evaluation criteria. In addition, we endeavored to develop a professional structure that would familiarize an individual with contemporary retina image feature segmentation techniques.

A practical, cost-effective method for accurate retina screening is essential for facilitating timely referral to an eye specialist in third-world settings where rural residents have limited access to adequate healthcare. Recently, smart phones have become a significant part of the medical field. These enables quick and easy access to digital images mailed electronically, instant messaging and virtual private networks, user-interface services, and mobile computing devices for health care. Statistical analysis revealed that when the image quality of nonmydriatic fundus images displayed on an iPhone was compared to that of a desktop computer, the image quality of the iPhone display was superior. This unexpected occurrence was attributed to the smart phone's advanced display capabilities (i.e., higher dot pitch and brightness). However, in its current form, the smart phone cannot replace the importance of in-person ophthalmic exams, but it remains an extremely promising platform for ophthalmic telemedicine. Due to the variable and low contrast in the digital color fundus image and the presence of noise, it is difficult to analyze the image features of the retina. The noises hinder the contrast enhancement technique and complicate the analysis of the fundus image.

Various pre-processing techniques aimed at correcting uneven illumination and low contrast that appeared in retinal images have been discussed. The dividing method using median filter on R-channel for background estimation showed promising ability in illumination correction with low CV value compared to the original images. The high mean value of CVs for the green component could be due to the high mean value of intensity on the red component of retinal images as compared to the red one. It should be noticed that the CV is equivalent to Standard Deviation divided by the mean intensity value (standard deviation/mean). The techniques consisting of dividing method using a median filter to estimate background, quotient-based and homomorphic filtering were found to be the effective correction techniques among the investigated techniques. They reduced some of the background illumination variation that was indicated by low mean CV value. The resulting images were however categorized as low-grade

Table 18

Comparison of the network parameters, training and testing time.

S no	Paper title	Parameters in millions	Training time	Testing time	Dataset
			in seconds	in seconds	
1	Deep Retinal Image Understanding [420]	7.8600		0.0850	DRIVE
2	M2U-Net: Effective and Efficient Retinal Vessel Segmentation for Real-World Applications [421]	0.5500		0.1040	STARE
3	Artery/vein segmentation using fully convolutional network [422]		35100	0.0650	DRIONS-DB
4	Segmenting Retinal Blood Vessels With Deep Neural Networks [423]	48.0000	28800	0.1100	RIM-ONE
5	Deep vessel segmentation by learning graphical connectivity [424]	7.9100		6.0000	DRIVE
6	Dense Dilated Network With Probability Regularized Walk for Vessel Detection [425]			23.5000	CHASE DB1
7	The Little W-Net that Could: State-of-the-Art Retinal Vessel Segmentation With Minimalistic Models [426]	0.0685	1920		DRIVE
			1800		CHASE DB
			8400		HRF
8	A cross-modality learning approach for vessel segmentation in retinal images [427]		25200	70.0000	
9	Multi-level deep supervised networks for retinal vessel segmentation [428]	7.6366	36000	92.0000	
10	Retinal vessel segmentation of color fundus images using multiscale convolutional neural network with an improved cross-entropy loss function [279]	0.4979		1.1000	
11	CcNet: a cross-connected convolutional network for segmenting retinal vessels using multi-scale features [296]		36000	0.0630	
12	Sine-Net: A fully convolutional deep learning architecture for retinal blood vessel segmentation [429]	0.6927	46800	0.3501	DRIVE
			46800	9.3217	CHASE_DB1
			46800		STARE
13	A Discriminatively Trained Fully Connected Conditional Random Field Model for Blood Vessel Segmentation in Fundus Images [430]			1.0000	DRIVE
14	U-Net: Convolutional Networks for Biomedical Image Segmentation [431]	31.0300		2.7000	CHASE_DB1
15	ERFNet: Efficient Residual Factorized ConvNet for Real-Time Semantic Segmentation [432]	2.0600		1.3000	STARE
16	Deformable convolutional networks [433]	7.8700		5.8000	HRF
17	A supervised blood vessel segmentation technique for digital Fundus images using Zernike Moment based features [434]	0.0014	300	336.0000	
18	VSSC Net: Vessel Specific Skip chain Convolutional Network for blood vessel segmentation [435]	8.0000		180.0000	
				2.29000	DRIVE
				1.6700	STARE
				4.2800	HRF
				2.4800	CHASE_DB1
				1.2600	
				1.7500	DCA1
				5.0000	
19	Retinal Vessel Segmentation using Deep Neural Networks [436]	0.1251	172800		
20	Supervised Segmentation of Un-annotated Retinal Fundus Images by Synthesis [437]		20820	0.4471	
21	SegNet: a deep convolutional encoder-decoder architecture for image segmentation [438]	29.4000	33696		DRIVE
22	DCCMED-Net: Densely connected and concatenated multi Encoder-Decoder CNNs for retinal vessel extraction from fundus images [439]	0.9700	52992		STARE
23	PixelBNN: Augmenting the PixelCNN with Batch Normalization and the Presentation of a Fast Architecture for Retinal Vessel Segmentation [440]		30960		DRIVE
24	Retinal vessel segmentation based on fully convolutional neural networks [278]	0.7939	51372		STARE
25	Scale-space approximated convolutional neural networks for retinal vessel segmentation [441]	27.2804	50400	0.0466	
26	DUNet: a deformable network for retinal vessel segmentation [283]		14400		DRIVE and STARE
			21600		CHASE_DB1
			64800		HRF
27	Segmentation of vessels in angiograms using convolutional neural networks [442]	0.8800		15.3000	
				106.0000	

images by ophthalmologists in subjective visual evaluation. Because with these methods, certain features such as the macula have been eliminated in the corrected images. Consequently, the application of these methods is not recommended in order to isolate the retinal structures based on texture features. The contrast enhancement methods have low performance to produce a suitable retinal image appearance; they may improve vessel extraction sensitivity due to vessel enhancement. Using CLAHE methods, the sensitivity of the segmentation algorithm in the vasculature increased. It is also shown that enhancement in vascular segmentation was achieved by applying a local contrast enhancement based on the adaptive histogram equalization. Nevertheless, it is worth mentioning that different preprocessing techniques were used by this group. It can also be concluded that the local equalization of histogram might be an efficient technique for contrast enhancement.

There are several methods of preprocessing that have been implemented on STARE database. Combinations of homomorphic filtering for illumination correction, along with morphologic filtering for contrast enhancement, obtained substantial results. The results of homomorphic filtering as its application effectively corrected the illumination.

Currently most publicly accessible databases are generated to evaluate the particular symptom (lesions) with less number of images, in addition there should be a common database for evaluating all forms of retina image analysis algorithms. The authors urge all medical image research groups to create a common database with a large number of images to evaluate screening algorithms for all steps of eye disease diagnoses, so that medical sciences have ultimate, high-performance, and globally accepted integrated diagnostic system. Automatic retinal image analysis methods aim to aid clinical decision-making, so it

is important to evaluate their performance, i.e., the level of agreement between their outputs and a reference standard (ground truth), which is typically a set of expert ophthalmologists' manual annotations. Sensitivity, specificity, precision, accuracy, and the F1-score are the most popular metrics for evaluating the effectiveness of retinal image segmentation methods. Performance measures are not always directly comparable between image analysis methods because they are evaluated using different (often non-public) datasets. For this reason, it is also challenging to select a single best method for a specific task based solely on its recorded performance measures. It is often unclear, for example, whether a method's sensitivity and specificity will change depending on the ratio of diseased and non-diseased images in the dataset. As a result, we recommend testing methods on a subset of images that represent the desired data to be analyzed to select the best methods for image analysis.

This paper examined the state-of-the-art methods for extracting and segmenting features from retina images, as well as the most popular datasets for this task. Comprehensive research has been conducted on 161 retina image analysis algorithms. The articles reviewed are grouped into 7 parts based on the features of the retina image: blood vessels, optical disk/ optical cup, exudates, hemorrhage, macular edema, laser scars and AV nicking segmentation. The articles reviewed are divided into two methods: unsupervised methods and supervised techniques for every feature of the retina image. Table 19 gives the complete overview of retina image analysis review. Furthermore, a comparison of quantitative performance measures is illustrated. Fig. 15 presents the best results of common performance measures on commonly used publicly available datasets for each feature. In Fig. 15 (a), best results of vessels segmentation on DRIVE and STARE datasets are presented. Best results of Optical Disk/Optical Cup segmentation on DRISHTI_GS and RIM-ONE dataset are shown in Fig. 15 (b). Best results of exudates segmentation on IDRiD, DIARET_DB1, E-Ophtha, and MESSIDOR dataset are shown in Fig. 15 (c). In Fig. 15(d), best results of hemorrhages segmentation on IDRiD, MESSIDOR, and DIARET_DB1 datasets are presented. Similarly, best results of macular edema on MESSIDOR and BIOMISA, laser scars on LMD, and AV nicking on DRIVE, IOSTAR, and INSPIRE datasets are illustrated in Fig. 15 (e), (f), (g), respectively.

For the segmentation of the retinal blood vessels, 52 algorithms were exhaustively covered, of which 22 were discussed under unsupervised techniques and 30 were discussed under supervised techniques. Sensitivity, specificity, accuracy and AUC are used as quantitative performance measure. Automatic vessel extraction and segmentation is crucial for early disease detection in the retina. Many researchers have used different algorithms for the task of segmenting the retinal vessels. While such algorithms are sufficiently effective to diagnose retinal disease, they are not meant to be an alternative for retinal experts. They are designed to reduce the workload on human experts. Despite of advancements in technology, collecting retinal imaging is getting better and better using high-resolution fundus cameras. The segmentation of these high-quality images will lower the likelihood of pixel identification (marked or not as a vessel). Deep learning approaches have an average accuracy of 98% approximately, strongly indicating that these algorithms can be used in early-stage retinal vascular segmentation tasks to prevent victims. Every approach to introducing a segmentation of vessels has its own advantages and disadvantages. As a result, selecting a specific approach for retinal vascular segmentation is extremely difficult.

A total of 23 algorithms have been comprehensively covered for optical disk/optical cup segmentation in this survey, from which 11 algorithms have been discussed under unsupervised techniques and 12 algorithms are discussed under supervised optical disk/optical cup segmentation techniques. Sensitivity, specificity, accuracy, precision, CDR, F1 Score and AUC are used as quantitative performance measure. Although, there are many promising approaches, the segmentation

techniques still have room for improvement. Only a few current techniques can be applied to glaucomatous retinal images, whether for segmentation of the optic disk or the optic cup. Due to low contrast and invisible boundaries between disk and cup, under segmentation or over-segmentation of disk and cups with large or small sizes is considered as a challenge. Classification accuracy decreases with an increase in image numbers. Therefore an improved approach to classification is required to precisely classify normal and abnormal cases. Segmentation efficiency is reduced by the presence of retinal blood vessels and peripapillary atrophy. For the removal of vessels and the avoidance of the peripapillary area as a disk area, an improved pre-processing approach is therefore required. It is also noted that fewer works have been reported for optic cup segmentation. The diagnosis of glaucoma necessitates an improved method for segmenting the optic cup. Due to increased complexity and reduced accuracy, not all of the diagnostic parameters were taken into account at the same time. Because of increased complexity, limited approaches were used in fusion for the segmentation of disk and cup. In addition, the images with relatively low resolution (varying from 0.4 to 0.3 megapixels) has made segmentation much more challenging. Segmentation would be aided by an improved camera capable of taking large quantities of high-resolution retinal images.

A total number of 28 algorithms have been comprehensively covered for exudate segmentation, from which 11 algorithms were discussed under unsupervised techniques and 17 algorithms are discussed under supervised exudate segmentation techniques. Sensitivity, specificity, accuracy, PPV, and AUC are used in quantitative performance measures. A wide range of methods have been proposed for automated detection of exudates but do not provide a strong distinction between types of exudates. It is difficult to generalize individual results, as these reported systems are highly optimized with the respective retinal images analyzed. In general, the majority of retinal images are characterized by low contrast and are infested with image artifacts that prevent further analysis of automatic exudate detection and segmentation. The features suggested in different approaches have required exploitation in eliminating the false positive region in the detection of exudates. Overall, most of the exudate extraction methods have been based on thresholding techniques and a combination of classifier. Applying easy thresholding directly to color fundus images is a major challenge because of variation factors in spatial illumination. To overcome this problem most techniques need contrast enhancement or shade correction on the images before thresholding is applied. The training and classification of exudates requires intensive computing power. Some researchers have tried to detect exudates using region growing techniques that are likely to result in segmentation or over segmentation and time consuming.

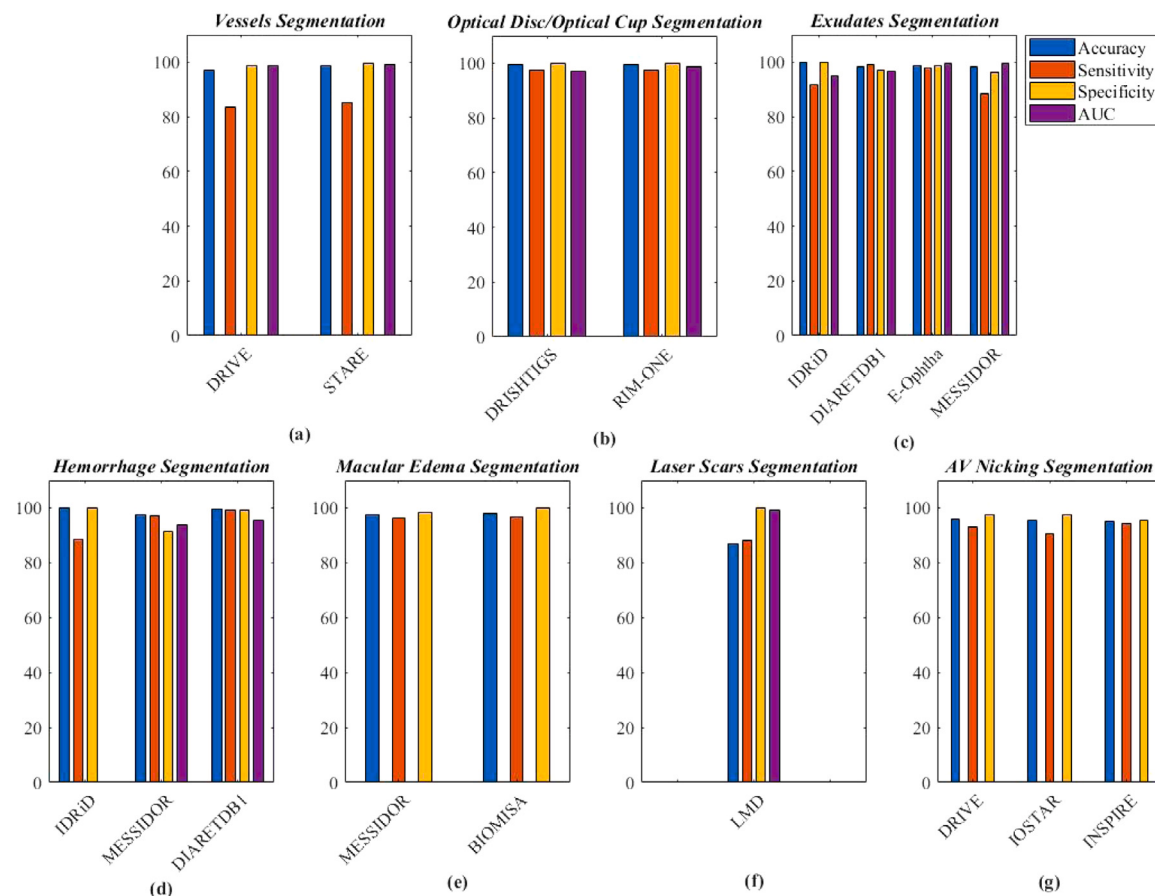
A total of 13 algorithms were comprehensively covered for hemorrhage segmentation, from which 5 algorithms were discussed under unsupervised techniques and 8 algorithms are discussed under supervised techniques for segmentation of hemorrhages. Sensitivity, specificity, accuracy, and AUC are used as quantitative performance measurements. Automatic hemorrhage detection poses complex challenges. Hemorrhages are difficult to distinguish from background variations, since they are typically low in contrast. Multiple dark areas in the image, such as the blood vessels, fovea, and microaneurysms, may complicate automatic detection of hemorrhage. Hemorrhages have a variable size and are often so small that they can easily be confused with noise or microaneurysms of the images and no standard database that classifies hemorrhage by shape. The most false detection is the case when the blood vessels are adjacent to, or hemorrhages overlap. So effective methodology for detecting hemorrhages is needed.

A total number of 24 algorithms is comprehensively covered for macular edema segmentation, from which 7 algorithms are discussed under unsupervised techniques and 17 algorithms are discussed under supervised macular edema segmentation techniques. Accuracy, sensitivity, specificity, AUC and F1 Score are used as quantitative

Table 19

Overview of Retina Features Segmentation review.

S no	Features	Unsupervised methods	Supervised methods	Total	Performance measures						
					Acc	Sen	Spe	Pre	AUC	PPV	F1 score
1	Blood vessels	22	30	52	✓	✓	✓		✓		
2	OD/OC	11	12	23	✓	✓	✓	✓	✓	✓	✓
3	Exudates	11	17	28	✓	✓	✓		✓	✓	
4	Hemorrhage	5	8	13	✓	✓	✓		✓		
5	Macular edema	7	17	24	✓	✓	✓		✓		
6	Laser scars	3	4	7	✓	✓	✓		✓	✓	✓
7	AV nicking	6	8	14	✓	✓	✓	✓			
	Total	65	96	161							

**Fig. 15.** Best performance for different features segmentation on different datasets: (a) Blood Vessels, (b) Optical Disk/Optical Cup, (c) Exudates, (d) Hemorrhages, (e) Macular Edema, (f) Laser Scars, and (g) AV Nicking.

performance measures. Macular edema is characterized by exudates occurring within the macular region's little section. The number of exudates in the component, their symmetry, and the frequency with which they occur within the macular region determine the severity of macular edema. An appealing number of techniques used supervised pattern recognition algorithms for macular edema segmentation or detection among all the methodologies studied. Despite the success that supervised algorithms have achieved in this area, a significant requirement for this strategy is the availability of ground truths as well as fundus datasets. In terms of both the requisite medical professionals and the time required, establishing ground truth with fundus datasets is time-consuming and resource-intensive. While deep learning for this problem domain is still in its infancy, the results gained utilizing these techniques are impressive, commendable, deep learning also implies the availability of a large number of annotated data instances.

A total of 7 algorithms have been comprehensively covered for laser scar segmentation, from which 3 algorithms are discussed under

unsupervised techniques and 4 algorithms are discussed under supervised techniques for segmentation of laser scars. Sensitivity, specificity, accuracy, PPV, and AUC are used in quantitative performance measures. The automatic laser scars detection algorithms mentioned in this paper focus on alternative solutions which allow less detection of false positives to detect laser scars from images of retina. It is hard to diagnose laser scars in "Laser" retinal images where they have not been detected, but it is more important to reduce the number of candidate regions in retinal images without treatment, so the specificity is closer to 100% and therefore applicable in clinical context. For example, regions detected nearby the OD and the blood vessels are removed, so it would be one of the valid approaches to identify other characteristics that would indicate that the region detected is not a laser scar. In addition, despite the fact that the vessel extractor is very effective, it would be crucial to improve it so as to avoid detection in blood vessels that are not segmented. To add more relevant features to the classifier, it is essential to find more features to improve performance.

A total number of 14 algorithms were comprehensively covered for AV nicking segmentation, from which 6 algorithms were discussed under unsupervised techniques and 8 algorithms are discussed under supervised AV nicking segmentation techniques. Sensitivity, specificity, accuracy, precision and F1 score are used in quantitative performance evaluation. Expert ophthalmologists can see the segmented retinal vessels to diagnose different retinal disorders, which are very useful for inspecting the AV nicking. Although AV detection methods generally produce good results, their performance is not optimal because human graders are better able to estimate AV nicking detection vascular labels.

9.2. Research gaps of the existing features segmentation methods

The performance of feature segmentation is directly associated with the quality of the images. Unfortunately, due to non-invasive acquisition and environmental conditions, retinal fundus images used to diagnose ophthalmological disorders are frequently visually and subjectively damaged. These complexity impair proper feature representation learning and lower the models accuracy. The review of features segmentation reveals that retinal disease diagnosis is still an open problem, and it requires more research to be done. Deep learning method are the advanced methods for features segmentation from the retinal images. There are few deep learning-based methods, and advanced deep learning methods must be designed to address these issues. The acquisition of large amounts of annotated fundus images with image-level and pixel-level annotations is one of the most difficult problems in developing robust deep-learning algorithms. The key challenge is not the availability of large datasets, but rather the annotation of these images, which is complex and requires the services of professional ophthalmologists. Traditional supervised learning algorithms rely significantly on the amount of labeled training data available. Even though there is a plenty of data available, the lack of annotations has compelled academics to seek out alternate techniques that can make use of it. This is where self-supervised algorithms come into play, propelling deep learning forward without the need for costly annotations and develop feature representations where data provides supervision. Supervised learning is not only costly in terms of annotations, but it also suffers from problems such as generalization error, spurious correlations, and adversarial attacks [443]. Recently, self-supervised learning techniques that can use unlabeled data to learn the underlying representations have combined generative and contrastive approaches. A common strategy is to suggest numerous pretext tasks that aid in learning features using pseudo labels. The ability to learn accurate representations has been demonstrated using tasks like image-inpainting, colorizing grayscale images, jigsaw puzzles, super-resolution, video frame prediction, audio-visual correlation, etc. After the advent of Generative Adversarial Networks (GANs) [444] in 2014, generative models gained prominence. The technique was then used to build numerous successful architectures, including CycleGAN [445], StyleGAN [446], PixelRNN [447], Text2Image [448], DiscoGAN [449], and others. More researchers were inspired by these strategies to train deep learning models with unlabeled data in a self-supervised setting. Despite their effectiveness, researchers began to recognize a few drawbacks of GAN-based methods. They are more difficult to train for two primary reasons: (a) non-convergence—the model parameters oscillate frequently and seldom converge; and (b) the discriminator becomes too successful, preventing the generator network from producing fakes that are realistic enough to allow for further learning. In order to prevent the generator from diverging and the discriminator from converge, adequate synchronization between the two is also necessary. In contrast to generative models, contrastive learning (CL) is a discriminative strategy that seeks to group similar data together and diverse ones apart. The majority of previous publications in this domain successfully coupled some form of instance-level classification approach [450] with contrastive learning. Recent methods, such as SwAV [451], MoCo [452], and SimCLR [453], with updated

approaches, have obtained results comparable to the state-of-the-art supervised method on the ImageNet [454] dataset. Similarly, PIRL [455], Selfie [456], and the work in [457] are examples of publications that demonstrate the efficacy of the pretext tasks utilized and how they improve the performance of their models. Uncertainties in Automatic disease diagnostic system is another area of research. Uncertainty is defined as a model's ability to express decision ambiguity [458]. Deep learning-based classifiers often return the class with the greatest softmax output, even if the margin is small. End-users must be notified when a model is uncertain in order to avoid making incorrect judgments. There are two types of uncertainty in a system: aleatoric and epistemic [458,459]. The intrinsic uncertainty in the system resulting from the modeling process, such as stochastic behavior, is referred to as aleatoric uncertainty or doubt. On the other side, epistemic uncertainty or ambiguity emerges as a result of inadequate data, resulting in less knowledge about the system. The former is inherent in the model and cannot be modified. The latter can be effectively minimized by using larger training data and ensuring that new types of data (or adversaries) are detected. The Bayesian theory is used to explain network uncertainty, but the computational complexity makes it impractical for high-dimensional issues such as image classification. Existing deep learning models, on the other hand, can be cast as Bayesian models without modifying the models [460]. When testing, the dropout layer, which is only used during training, is turned on, and the model is iterated over numerous times for each test sample. For each image, this yields an approximate posterior probability distribution. According to a study for the diagnosis of diabetic retinopathy using retinal fundus image [461], this uncertainty information can enhance diagnostic performance. Instead of making an uncertain decision, it assisted in identifying unexpected visuals that should be reported to a clinician. A doctor is able to recognize when they are unsure about a case and can consult additional sources of information (e.g. additional tests, medical history, etc.). Deep learning methods, on the other hand, have been proposed without any explicit measures to assess their uncertainty. Due to this, user trust in the system must be calibrated, which results in lower acceptance. To reduce mistakes, samples with significant uncertainty can be forwarded to a human expert. Previous research has found that ambiguous situations are highly associated with errors, and that recognizing them improves model performance. Another issue with medical imaging datasets is class imbalance. The number of normal patients are substantially higher than the number of patients with disease in fundus images. The number of images with various disease complications and lesions varies. Large-scale fundus screening methods around the globe generate massive datasets of retina images, however the vast majority of the images contain no suspicious symptoms or lesions. It is also observed from the literature review that heavy network are used for binary class segmentation as evident from Table 18. Although these networks work well, but it is totally a waste of resources. Feature loss due to down sampling is another major challenge in the medical imaging datasets. To train heavy networks, the spatial dimensions of the images are reduced by performing down sampling blindly, which is not preferred in medical imaging because features are lost due to down sampling.

9.3. Future directions

A considerable population of the world is suffering from different vision-threatening retinal diseases such as diabetic retinopathy, glaucoma, amblyopia, strabismus, and age-related macular degeneration. This critical concern has partly emerged due to the expensive nature of necessary equipment required for ophthalmological disease diagnosis and partly due to the lack of availability of ophthalmological experts. Timely diagnosis of these retinal diseases is crucial in preventing vision loss and blindness, where affordable computer-aided tools can potentially play a vital role. Over the last decade, technology has rapidly changed, including 5G, smart phones, machine

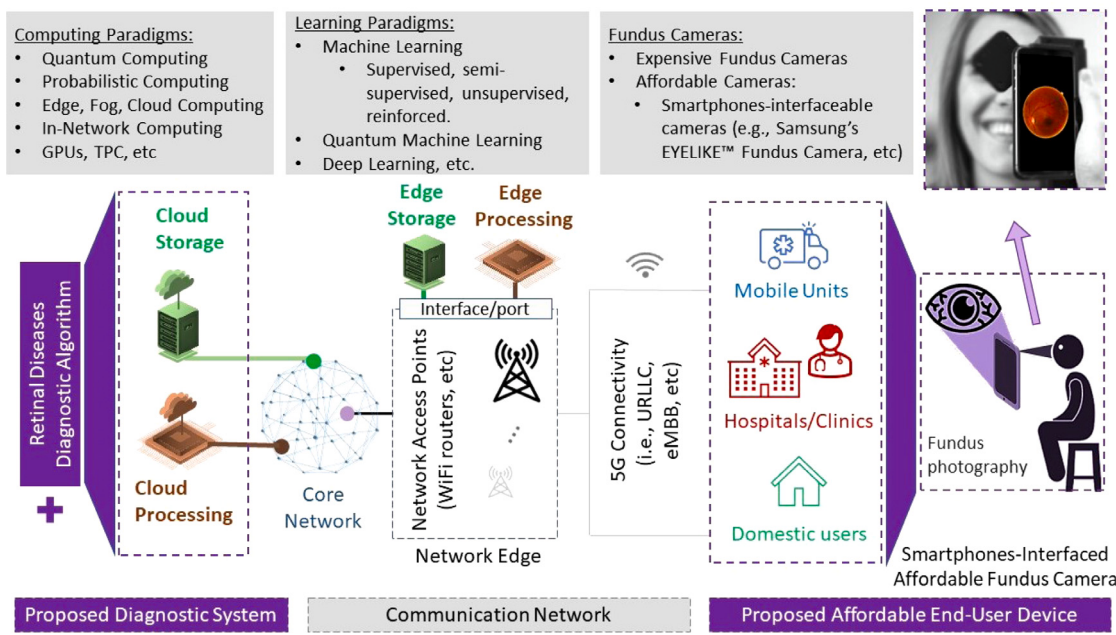


Fig. 16. Retinal imaging-based system model for ophthalmic healthcare and monitoring system.

learning, artificial intelligence, cloud computing, big data, and so on. Bringing these technologies together on a single platform has the potential to significantly enhance the future diagnosis of diseases using retinal imaging and artificial intelligence. The fundamental concept of a possible future retinal imaging-based system model is illustrated in Fig. 16. The idea is to utilize smartphones to enable widespread access of cloud ophthalmic healthcare facilities in the developing countries, especially in underserved remote regions. The retinal images collected at the cloud- and edge-processing servers through wireless network connectivity (5G URLLC) of user-end smartphone-interfaceable fundus cameras will be utilized for employing advanced Artificial Intelligence (AI) methods for analyzing and diagnosing ophthalmic diseases. The developed users-end application will exploit the heaving computational capabilities of cloud-processing and storage facilities to record the data and accurately suggest any treatment regimen. This proposed data flow and diagnosis process will only impose a minor fraction of the cost of commercial instruments on the users/clinics/remote units. The affordable diagnosis camera can screen for conditions that may lead to blindness, including diabetic retinopathy, glaucoma, and age-related macular degeneration.

There are numerous potential and unexplored areas that could be investigated to improve the efficiency of the proposed system. We have identified the following research possibilities:

1. The simultaneous detection of multiple retinal diseases using DL is an interesting and potentially fruitful area of study. Clinicians may find this helpful in identifying patients who have more than one retinal disease. Despite the fact that research has been conducted in this field, such as simultaneous “DME and DR diagnosis”, this is still a relatively under-researched area.
2. Obtaining professional doctors' approval for the AI-based model is one of the primary concerns of DL implementation for the diagnosis of retinal diseases. Very little research has been conducted to improve the interpretability of the predictions. Creating evidence maps for the predictions made by the DL model and highlighting the crucial regions of the fundus image used by the deep network to reach a conclusion could be one potential solution.
3. Most hospitals and other research institutions are hesitant to share fundus images due to various data privacy laws. This

exacerbates the data scarcity issue and restricts model training to only available public datasets, depriving them of training on the hospitals' rich and diverse private fundus data. Schemes such as federated learning, in which models can be trained on private data locally and then the learned weights transferred to a global model, can be investigated.

4. Due to the differences in image acquisition settings between datasets, it is observed that the performance of DL models varied across datasets, i.e., some models performed well on specific datasets but poorly on others. Researchers can concentrate on enhancing the performance of model generalization by exploring various domain adaptation techniques. In light of the complexities involved in acquiring retinal fundus images, the area of domain adaptation offers researchers ample future opportunities for improving model generalization.
5. The majority of DL models developed for the diagnosis of retinal diseases perform well at the expense of a high demand for computational resources. This is a significant barrier to the implementation of such models on portable edge devices. Another open area of research in this field is the development of novel lightweight models that reduce computational parameters without sacrificing performance.
6. Fundus images captured by high-resolution fundoscopy are used in the majority of current research in this field. There is ample opportunity for researchers to create models that can learn from fundus images captured on smartphones. This will aid the development of proposed system.
7. Recent advancements in Generative Adversarial Networks (GAN) have demonstrated the ability to generate synthetic fundus images that can be used to supplement the training dataset. This can effectively eliminate the lack of high-quality labeled data and improve the performance of prediction. Recent research has demonstrated the synthesis of images for diabetic retinopathy, glaucoma, and age-related macular degeneration, but the field is still in its early stages, so there is plenty of room for future research.

9.4. Conclusion

This survey thoroughly reviews various articles in the literature for the analysis of various aspects of retinal images. Unlike previous review

articles, this one takes a comprehensive look at the entire retinal image processing theory, including retinopathy, computer-aided tools, ML/DL methods, computing platforms, and other important aspects. This paper discusses recent trends and advances in retinal image analysis, as well as a thorough review of retinal image segmentation and detection methods. A comprehensive survey of the state-of-the-art of the detection and segmentation methods for retinal features, an exhaustive coverage of all the important retinal image features and noticeable databases of the fundus images. The characterization of the existing notable literature into different key categories/classes, and a thorough comparative analysis of the noteworthy existing retinal image analysis schemes in terms of the identified key performance indicators are also the major contributions of this survey. Following the conclusion of this survey, the future research directions for the analysis of retinal images are also discussed.

CRediT authorship contribution statement

Shahzaib Iqbal: Conception and design of study, Analysis and/or interpretation of data, Writing – original draft, Writing – review & editing. **Tariq M. Khan:** Conception and design of study, Analysis and/or interpretation of data, Writing – original draft, Writing – review & editing. **Khuram Naveed:** Conception and design of study, Analysis and/or interpretation of data, Writing – original draft, Writing – review & editing. **Syed S. Naqvi:** Conception and design of study, Analysis and/or interpretation of data, Writing – original draft, Writing – review & editing. **Syed Junaid Nawaz:** Conception and design of study, Analysis and/or interpretation of data, Writing – original draft, Writing – review & editing.

Declaration of competing interest

The authors declare that they have no known competing financial interests or personal relationships that could have appeared to influence the work reported in this paper.

Acknowledgment

All authors approved the version of the manuscript to be published.

References

- [1] T.M. Khan, A. Robles-Kelly, S.S. Naqvi, A semantically flexible feature fusion network for retinal vessel segmentation, in: International Conference on Neural Information Processing, Springer, Cham, 2020, pp. 159–167.
- [2] B. Caridi, D. Doncheva, S. Sivaprasad, P. Turowski, Galectins in the pathogenesis of common retinal disease, *Front. Pharmacol.* (2021) 1173.
- [3] I. Razzak, G. Shoukat, S. Naz, T.M. Khan, Skin lesion analysis toward accurate detection of melanoma using multistage fully connected residual network, in: 2020 International Joint Conference on Neural Networks, IJCNN, IEEE, 2020, pp. 1–8.
- [4] K. Minhas, T.M. Khan, M. Arsalan, S.S. Naqvi, M. Ahmed, H.A. Khan, M.A. Haider, A. Haseeb, Accurate pixel-wise skin segmentation using shallow fully convolutional neural network, *IEEE Access* 8 (2020) 156314–156327.
- [5] T.M. Khan, S.S. Naqvi, M. Arsalan, M.A. Khan, H.A. Khan, A. Haider, Exploiting residual edge information in deep fully convolutional neural networks for retinal vessel segmentation, in: 2020 International Joint Conference on Neural Networks, IJCNN, IEEE, 2020, pp. 1–8.
- [6] T.M. Khan, F. Abdullah, S.S. Naqvi, M. Arsalan, M.A. Khan, Shallow vessel segmentation network for automatic retinal vessel segmentation, in: 2020 International Joint Conference on Neural Networks, IJCNN, IEEE, 2020, pp. 1–7.
- [7] E.S. Shin, C.M. Sorenson, N. Sheibani, Diabetes and retinal vascular dysfunction, *J. Ophthalmic Vis. Res.* 9 (3) (2014) 362.
- [8] M.A. Khan, T.M. Khan, K.I. Aziz, S.S. Ahmad, N. Mir, E. Elbakush, The use of fourier phase symmetry for thin vessel detection in retinal fundus images, in: 2019 IEEE International Symposium on Signal Processing and Information Technology, ISSPIT, IEEE, 2019, pp. 1–6.
- [9] M. Mehmood, T.M. Khan, M.A. Khan, S.S. Naqvi, W. Alhalabi, Vessel intensity profile uniformity improvement for retinal vessel segmentation, *Procedia Comput. Sci.* 163 (2019) 370–380.
- [10] T.B. Sekou, M. Hidane, J. Olivier, H. Cardot, From patch to image segmentation using fully convolutional networks - application to retinal images, 2019, CoRR abs/1904.03892, arXiv:1904.03892, URL <http://arxiv.org/abs/1904.03892>.
- [11] S. Iqbal, S. Naqvi, H. Ahmed, A. Saadat, T.M. Khan, G-net light: a lightweight modified google net for retinal vessel segmentation, 2022.
- [12] M. Arsalan, T.M. Khan, S.S. Naqvi, M. Nawaz, I. Razzak, Prompt deep lightweight vessel segmentation network (PLVS-net), *IEEE/ACM Trans. Comput. Biol. Bioinform.* (2022).
- [13] M.A. Khan, T.M. Khan, T.A. Soomro, N. Mir, J. Gao, Boosting sensitivity of a retinal vessel segmentation algorithm, *Pattern Anal. Appl.* 22 (2) (2019) 583–599.
- [14] M.A. Ahamed, A.A.Z. Imran, Joint learning with local and global consistency for improved medical image segmentation, in: G. Yang, A. Aviles-Rivero, M. Roberts, C.-B. Schönlieb (Eds.), *Medical Image Understanding and Analysis*, Springer International Publishing, Cham, 2022, pp. 298–312.
- [15] A. Bilal, G. Sun, S. Mazhar, Survey on recent developments in automatic detection of diabetic retinopathy, *J. Français d'Ophtalmol.* 44 (3) (2021) 420–440.
- [16] M.E. Martinez-Perez, A.D. Hughes, S.A. Thom, A.A. Bharath, K.H. Parker, Segmentation of blood vessels from red-free and fluorescein retinal images, *Med. Image Anal.* 11 (1) (2007) 47–61.
- [17] Y. Hou, Automatic segmentation of retinal blood vessels based on improved multiscale line detection, *J. Comput. Sci. Eng.* 8 (2) (2014) 119–128.
- [18] B. Yin, H. Li, B. Sheng, X. Hou, Y. Chen, W. Wu, P. Li, R. Shen, Y. Bao, W. Jia, Vessel extraction from non-fluorescein fundus images using orientation-aware detector, *Med. Image Anal.* 26 (1) (2015) 232–242.
- [19] H.A. Nugroho, T. Lestari, R.A. Aras, I. Ardijanto, Segmentation of retinal blood vessels using gabor wavelet and morphological reconstruction, in: Proc. of Intl. Conf. on Sci. in Info. Technol., IEEE, 2017, pp. 513–516.
- [20] W.S. Oliveira, J.V. Teixeira, T.I. Ren, G.D. Cavalcanti, J. Sijbers, Unsupervised retinal vessel segmentation using combined filters, *PLoS One* 11 (2) (2016) e0149943.
- [21] H. Aguirre-Ramos, J.G. Avina-Cervantes, I. Cruz-Aceves, J. Ruiz-Pinales, S. Ledesma, Blood vessel segmentation in retinal fundus images using Gabor filters, fractional derivatives, and Expectation Maximization, *Appl. Math. Comput.* 339 (2018) 568–587.
- [22] M.A. Khan, T.A. Soomro, T.M. Khan, D.G. Bailey, J. Gao, N. Mir, Automatic retinal vessel extraction algorithm based on contrast-sensitive schemes, in: Proc. of Intl. Conf. on Image and Vision Comput., IEEE, 2016, pp. 1–5.
- [23] D.A. Da Rocha, A.B.L. Barbosa, D.S. Guimarães, L.M. Gregório, L.H.N. Gomes, L. da Silva Amorim, Z.M.A. Peixoto, An unsupervised approach to improve contrast and segmentation of blood vessels in retinal images using CLAHE, 2D Gabor wavelet, and morphological operations, *Research on Biomed. Eng.* 36 (1) (2020) 67–75.
- [24] P. Bankhead, C.N. Scholfield, J.G. McGeown, T.M. Curtis, Fast retinal vessel detection and measurement using wavelets and edge location refinement, *PLoS One* 7 (3) (2012) e32435.
- [25] A.F. Frangi, W.J. Niessen, K.L. Vincken, M.A. Viergever, Multiscale vessel enhancement filtering, in: Proc. of Intl. Conf. on Med. Image Comput. and Computer-Assisted Intervention, Springer, 1998, pp. 130–137.
- [26] N.P. Singh, R. Srivastava, Retinal blood vessels segmentation by using gumbel probability distribution function based matched filter, *Comput. Methods Progr. Biomed.* 129 (2016) 40–50.
- [27] J. Zhang, B. Dashtbozorg, E. Bekkers, J.P. Pluim, R. Duits, B.M. Ter Haar Romeny, Robust Retinal Vessel Segmentation via Locally Adaptive Derivative Frames in Orientation Scores, *IEEE Trans. Med. Imag.* 35 (12) (2016) 2631–2644.
- [28] S.A.A. Shah, T.B. Tang, I. Faye, A. Laude, Blood vessel segmentation in color fundus images based on regional and hessian features, *Graefe's Arch. Clin. Exp. Ophthalmol.* 255 (8) (2017) 1525–1533.
- [29] T. Jerman, F. Pernuš, B. Likar, Ž. Špiclin, Beyond Frangi: an improved multiscale vesselness filter, in: Proc. of Med. Imaging 2015: Image Process., Vol. 9413, International Society for Optics and Photonics, 2015, p. 94132A.
- [30] M. Shahid, I.A. Taj, Robust retinal vessel segmentation using vessel's location map and frangi enhancement filter, *IET Image Process.* 12 (4) (2018) 494–501.
- [31] K. Naveed, F. Abdullah, H.A. Madni, M.A. Khan, T.M. Khan, S.S. Naqvi, Towards automated eye diagnosis: an improved retinal vessel segmentation framework using ensemble block matching 3D filter, *Diagnostics* 11 (1) (2021) 114.
- [32] L.C. Neto, G.L. Ramalho, J.F.R. Neto, R.M. Veras, F.N. Medeiros, An unsupervised coarse-to-fine algorithm for blood vessel segmentation in fundus images, *Expert Syst. Appl.* 78 (2017) 182–192.
- [33] R. Sundaram, K.S. Ravichandran, P. Jayaraman, et al., Extraction of blood vessels in fundus images of retina through hybrid segmentation approach, *Mathematics* 7 (2) (2019) 169.
- [34] B. Al-Diri, A. Hunter, D. Steel, An active contour model for segmenting and measuring retinal vessels, *Trans. Med. Imag.* 28 (9) (2009) 1488–1497.
- [35] R.S. Michalski, J.G. Carbonell, T.M. Mitchell, *Machine Learning: An Artificial Intelligence Approach*, Springer Sci. & Business Media, 2013.
- [36] P. Burlina, A. Galdran, P. Costa, A. Cohen, A. Campilho, Artificial intelligence and deep learning in retinal image analysis, in: *Computat. Retinal Image Anal.*, Elsevier, 2019, pp. 379–404.

- [37] W.L. Alyoubi, W.M. Shalash, M.F. Abulkhair, Diabetic retinopathy detection through deep learning techniques: A review, *Inf. Med. Unlocked* (2020) 100377.
- [38] S. Sengupta, A. Singh, H.A. Leopold, T. Gulati, V. Lakshminarayanan, Ophthalmic diagnosis using deep learning with fundus images—A critical review, *Artif. Intell. Med.* 102 (2020) 101758.
- [39] S. Stolte, R. Fang, A survey on medical image analysis in diabetic retinopathy, *Med. Image Anal.* 64 (2020) 101742.
- [40] M.H. Sarhan, M.A. Nasseri, D. Zapp, M. Maier, C.P. Lohmann, N. Navab, A. Eslami, Machine learning techniques for ophthalmic data processing: a review, *IEEE J. Biomed. Health Inf.* 24 (12) (2020) 3338–3350.
- [41] T.A. Soomro, A.J. Afifi, L. Zheng, S. Soomro, J. Gao, O. Hellwich, M. Paul, Deep learning models for retinal blood vessels segmentation: a review, *IEEE Access* 7 (2019) 71696–71717, <http://dx.doi.org/10.1109/ACCESS.2019.2920616>.
- [42] A. Imran, J. Li, Y. Pei, J. Yang, Q. Wang, Comparative analysis of vessel segmentation techniques in retinal images, *IEEE Access* 7 (2019) 114862–114887, <http://dx.doi.org/10.1109/ACCESS.2019.2935912>.
- [43] M.V. Maheswari, G. Murugeswari, A survey on computer algorithms for retinal image preprocessing and vessel segmentation, in: *Proc. of Intl. Conf. on Inventive Computat. Technol., IEEE, 2020*, pp. 403–408.
- [44] J. Cohen, T. Cao, J. Viviano, C.-W. Huang, M. Fralick, M. Ghassemi, M. Mamdani, R. Greiner, Y. Bengio, Problems in the deployment of machine-learned models in health care, *Canad. Med. Assoc. J.* 193 (2021) <http://dx.doi.org/10.1503/cmaj.202066>, cmaj.202066.
- [45] T.M. Khan, A. Robles-Kelly, S.S. Naqvi, T-Net: A resource-constrained tiny convolutional neural network for medical image segmentation, in: *Proceedings of the IEEE/CVF Winter Conference on Applications of Computer Vision, 2022*, pp. 644–653.
- [46] T.M. Khan, S.S. Naqvi, E. Meijering, Leveraging image complexity in macro-level neural network design for medical image segmentation, 2021, arXiv preprint [arXiv:2112.11065](https://arxiv.org/abs/2112.11065).
- [47] T.M. Khan, S.S. Naqvi, A. Robles-Kelly, E. Meijering, Neural network compression by joint sparsity promotion and redundancy reduction, 2022, [arXiv:2210.07451](https://arxiv.org/abs/2210.07451).
- [48] T.M. Khan, M. Arsalan, A. Robles-Kelly, E. Meijering, MKIS-net: a light-weight multi-kernel network for medical image segmentation, 2022, [arXiv:2210.08168](https://arxiv.org/abs/2210.08168).
- [49] S.R. Upadhyaya, Parallel approaches to machine learning—A comprehensive survey, *J. Parallel Distrib. Comput.* 73 (3) (2013) 284–292.
- [50] A. Behamida, M. Kozolvszky, S. Senasi, GPU usage trends in medical image processing, in: *Proc. of IEEE Intl. Symposium on Applied Computat. Intell. and Informatics, 2019*, pp. 320–325, <http://dx.doi.org/10.1109/SAC46893.2019.9111626>.
- [51] D. Demirović, E. Skejčić, A. Šerifović-Trbalić, Performance of some image processing algorithms in Tensorflow, in: *Proc. of Intl. Conf. on Syst. Signals and Image Process., 2018*, pp. 1–4.
- [52] T.M. Khan, A. Robles-Kelly, Machine learning: quantum vs classical, *IEEE Access* 8 (2020) 219275–219294, <http://dx.doi.org/10.1109/ACCESS.2020.3041719>.
- [53] S.J. Nawaz, S.K. Sharma, S. Wyne, M.N. Patwary, M. Asaduzzaman, Quantum machine learning for 6G communication networks: state-of-the-art and vision for the future, *IEEE Access* 7 (2019) 46317–46350, <http://dx.doi.org/10.1109/ACCESS.2019.2909490>.
- [54] T.M. Khan, A. Robles-Kelly, A derivative-free method for quantum perceptron training in multi-layered neural networks, in: *Intl. Conf. on Neural Inf. Process., Springer, Cham, 2020*, pp. 241–250.
- [55] F. Yin, D.W.K. Wong, Y. Quan, A.P. Yow, N.M. Tan, K. Gopalakrishnan, B.H. Lee, Y. Xu, Z. Zhang, J. Cheng, J. Liu, A cloud-based system for automatic glaucoma screening, in: *Proc. of Annual Intl. Conf. of the IEEE Eng. in Medicine and Biology Society, 2015*, pp. 1596–1599, <http://dx.doi.org/10.1109/EMBC.2015.7318679>.
- [56] S.J. Nawaz, S.K. Sharma, M.N. Patwary, M. Asaduzzaman, Enhanced URLLC-Enabled Edge Computing Framework for Device-Level Innovation in 6G, 2021, <http://dx.doi.org/10.36227/techrxiv.13325336.v2>, Techrxiv.
- [57] S. Sekhar, W. Al-Nuaimy, A.K. Nandi, Automated localisation of optic disk and fovea in retinal fundus images, in: *Proc. of European Signal Process. Conf., IEEE, 2008*, pp. 1–5.
- [58] C.G. Owen, A.R. Rudnicka, R.A. Welikala, M.M. Fraz, S.A. Barman, R. Luben, S.A. Hayat, K.-T. Khaw, D.P. Strachan, P.H. Whincup, et al., Retinal vasculometry associations with cardiometabolic risk factors in the european prospective investigation of cancer—norfolk study, *Ophthalmology* 126 (1) (2019) 96–106.
- [59] T.Y. Wong, P. Mitchell, Hypertensive retinopathy, *New England J. Med.* 351 (22) (2004) 2310–2317.
- [60] T. Wong, P. Mitchell, The eye in hypertension, *Lancet* 369 (9559) (2007) 425–435.
- [61] N. Patton, T.M. Aslam, T. MacGillivray, I.J. Deary, B. Dhillon, R.H. Eikelboom, K. Yugesan, I.J. Constable, Retinal image analysis: concepts, applications and potential, *Prog. Retin. Eye Res.* 25 (1) (2006) 99–127.
- [62] M.D. Abràmoff, M.K. Garvin, M. Sonka, Retinal imaging and image analysis, *IEEE Rev. Biomed. Eng.* 3 (2010) 169–208.
- [63] M.M. Fraz, P. Remagnino, A. Hoppe, B. Uyyanonvara, A.R. Rudnicka, C.G. Owen, S.A. Barman, Blood vessel segmentation methodologies in retinal images—a survey, *Comput. Methods Progr. Biomed.* 108 (1) (2012) 407–433.
- [64] O. Faust, R. Acharya, E.Y.-K. Ng, K.-H. Ng, J.S. Suri, Algorithms for the automated detection of diabetic retinopathy using digital fundus images: a review, *J. Med. Syst.* 36 (1) (2012) 145–157.
- [65] R.J. Winder, P.J. Morrow, I.N. McRitchie, J. Bailie, P.M. Hart, Algorithms for digital image processing in diabetic retinopathy, *Comput. Med. Imaging Graph.* 33 (8) (2009) 608–622.
- [66] Y. Kanagasingam, A. Bhuiyan, M.D. Abramoff, R.T. Smith, L. Goldschmidt, T.Y. Wong, Progress on retinal image analysis for age related macular degeneration, *Prog. Retin. Eye Res.* 38 (2014) 20–42.
- [67] W.M.D.W. Zaki, M.A. Zulkifley, A. Hussain, W.H.W. Halim, N.B.A. Mustafa, L.S. Ting, Diabetic retinopathy assessment: Towards an automated system, *Biomed. Signal Process. Control* 24 (2016) 72–82.
- [68] M. Fraz, M. Badar, A. Malik, S. Barman, Computational methods for exudates detection and macular edema estimation in retinal images: a survey, *Arch. Comput. Methods Eng.* 26 (4) (2019) 1193–1220.
- [69] S. Joshi, P. Karule, A review on exudates detection methods for diabetic retinopathy, *Biomed. Pharmacother.* 97 (2018) 1454–1460.
- [70] M.R.K. Mookiah, U.R. Acharya, C.K. Chua, C.M. Lim, E. Ng, A. Laude, Computer-aided diagnosis of diabetic retinopathy: A review, *Comput. Biol. Med.* 43 (12) (2013) 2136–2155.
- [71] R.F. Mansour, Evolutionary computing enriched computer-aided diagnosis system for diabetic retinopathy: a survey, *IEEE Rev. Biomed. Eng.* 10 (2017) 334–349.
- [72] J. Almotiri, K. Elleithy, A. Elleithy, Retinal vessels segmentation techniques and algorithms: a survey, *Appl. Sci.* 8 (2) (2018) 155.
- [73] A. Almazroa, R. Burman, K. Raahemifar, V. Lakshminarayanan, Optic disc and optic cup segmentation methodologies for glaucoma image detection: a survey, *J. Ophthalmol.* (2015).
- [74] N. Thakur, M. Juneja, Survey on segmentation and classification approaches of optic cup and optic disc for diagnosis of glaucoma, *Biomed. Signal Process. Control* 42 (2018) 162–189.
- [75] T. Teng, M. Lefley, D. Claremont, Progress towards automated diabetic ocular screening: a review of image analysis and intelligent systems for diabetic retinopathy, *Med. Biol. Eng. Comput.* 40 (1) (2002) 2–13.
- [76] A. Grossi, F. Veglio, M. Porta, F. Grignolo, T. Wong, Hypertensive retinopathy revisited: some answers, more questions, *Br. J. Ophthalmol.* 89 (12) (2005) 1646–1654.
- [77] S. Chatterjee, S. Chattopadhyay, M. Hope-Ross, P. Lip, Hypertension and the eye: changing perspectives, *J. Hum. Hypertens.* 16 (10) (2002) 667–675.
- [78] R. Marcucci, F. Sofi, E. Grifoni, A. Sodi, D. Prisco, Retinal vein occlusions: a review for the internist, *Internal Emerg. Med.* 6 (4) (2011) 307–314.
- [79] D.H. Lee, S.J. Lee, I.N. Yoon, Clinical progress in impending central retinal vein occlusion, *Korean J. Ophthalmol.* 24 (2) (2010) 83.
- [80] H.A. Quigley, A.T. Broman, The number of people with glaucoma worldwide in 2010 and 2020, *Br. J. Ophthalmol.* 90 (3) (2006) 262–267.
- [81] F. Abdullah, R. Imtiaz, H.A. Madni, H.A. Khan, T.M. Khan, M.A. Khan, S.S. Naqvi, A review on glaucoma disease detection using computerized techniques, *IEEE Access* 9 (2021) 37311–37333.
- [82] R. Imtiaz, T.M. Khan, S.S. Naqvi, M. Arsalan, S.J. Nawaz, Screening of Glaucoma disease from retinal vessel images using semantic segmentation, *Comput. Electr. Eng.* 91 (2021) 107036.
- [83] R. Thomas, R.S. Parikh, How to assess a patient for glaucoma, *Commun. Eye Health* 19 (59) (2006) 36.
- [84] D. Varma, S. Cugati, A. Lee, C. Chen, A review of central retinal artery occlusion: clinical presentation and management, *Eye* 27 (6) (2013) 688–697.
- [85] R. Lee, T.Y. Wong, C. Sabanayagam, Epidemiology of diabetic retinopathy, diabetic macular edema and related vision loss, *Eye Vis.* 2 (1) (2015) 1–25.
- [86] L. Claesson-Welsh, Vascular permeability—the essentials, *Upsala J. Med. Sci.* 120 (3) (2015) 135–143.
- [87] E.J. Duh, J.K. Sun, A.W. Stitt, Diabetic retinopathy: current understanding, mechanisms, and treatment strategies, *JCI Insight* 2 (14) (2017).
- [88] T.M. Khan, A. Robles-Kelly, S.S. Naqvi, A. Muhammad, Residual multiscale full convolutional network (RM-FCN) for high resolution semantic segmentation of retinal vasculature, in: *Structural, Syntactic, and Statistical Pattern Recognition: Joint IAPR International Workshops, S+ SSPR 2020, Padua, Italy, January 21–22, 2021, Proceedings*, Springer Nature, 2021, p. 324.
- [89] T.M. Khan, A. Robles-Kelly, S.S. Naqvi, RC-net: a convolutional neural network for retinal vessel segmentation, in: *2021 Digital Image Computing: Techniques and Applications, DICTA, IEEE, 2021*, pp. 01–07.
- [90] E. Korot, N. Pontikos, X. Liu, S.K. Wagner, L. Faes, J. Huemer, K. Balaskas, A.K. Denniston, A. Khawaja, P.A. Keane, Predicting sex from retinal fundus photographs using automated deep learning, *Sci. Rep.* 11 (1) (2021) 1–8.
- [91] Y.D. Kim, K.J. Noh, S.J. Byun, S. Lee, T. Kim, L. Sunwoo, K.J. Lee, S.-H. Kang, K.H. Park, S.J. Park, Effects of hypertension, diabetes, and smoking on age and sex prediction from retinal fundus images, *Sci. Rep.* 10 (1) (2020) 1–14.
- [92] M.R. Munk, T. Kurmann, P. Márquez-Neila, M.S. Zinkernagel, S. Wolf, R. Sznitman, Assessment of patient specific information in the wild on fundus photography and optical coherence tomography, *Sci. Rep.* 11 (1) (2021) 1–10.
- [93] R. Poplin, A.V. Varadarajan, K. Blumer, Y. Liu, M.V. McConnell, G.S. Corrado, L. Peng, D.R. Webster, Prediction of cardiovascular risk factors from retinal fundus photographs via deep learning, *Nat. Biomed. Eng.* 2 (3) (2018) 158–164.

- [94] T.H. Rim, G. Lee, Y. Kim, Y.-C. Tham, C.J. Lee, S.J. Baik, Y.A. Kim, M. Yu, M. Deshmukh, B.K. Lee, et al., Prediction of systemic biomarkers from retinal photographs: development and validation of deep-learning algorithms, *Lancet Digit. Health* 2 (10) (2020) e526–e536.
- [95] T. Yamashita, R. Asaoka, H. Terasaki, H. Murata, M. Tanaka, K. Nakao, T. Sakamoto, Factors in color fundus photographs that can be used by humans to determine sex of individuals, *Transl. Vis. Sci. Technol.* 9 (2) (2020) 4.
- [96] L. Zhang, M. Yuan, Z. An, X. Zhao, H. Wu, H. Li, Y. Wang, B. Sun, H. Li, S. Ding, et al., Prediction of hypertension, hyperglycemia and dyslipidemia from retinal fundus photographs via deep learning: A cross-sectional study of chronic diseases in central China, *PLoS One* 15 (5) (2020) e0233166.
- [97] N. Gerrits, B. Elen, T.V. Craenendonck, D. Triantafyllidou, I.N. Petropoulos, R.A. Malik, P. De Boever, Age and sex affect deep learning prediction of cardiometabolic risk factors from retinal images, *Sci. Rep.* 10 (1) (2020) 1–9.
- [98] B.K. Betzler, H.H.S. Yang, S. Thakur, M. Yu, Z. Da Soh, G. Lee, Y.-C. Tham, T.Y. Wong, T.H. Rim, C.-Y. Cheng, et al., Gender prediction for a multiethnic population via deep learning across different retinal fundus photograph fields: retrospective cross-sectional study, *JMIR Med. Inform.* 9 (8) (2021) e25165.
- [99] E. Vaghefi, S. Yang, S. Hill, G. Humphrey, N. Walker, D. Squirrell, Detection of smoking status from retinal images; a Convolutional Neural Network study, *Sci. Rep.* 9 (1) (2019) 1–9.
- [100] K.M. Flegal, B.K. Kit, H. Orpana, B.I. Graubard, Association of all-cause mortality with overweight and obesity using standard body mass index categories: a systematic review and meta-analysis, *JAMA* 309 (1) (2013) 71–82.
- [101] K. Bhaskaran, I. dos Santos-Silva, D.A. Leon, I.J. Douglas, L. Smeeth, Association of BMI with overall and cause-specific mortality: a population-based cohort study of 3–6 million adults in the UK, *Lancet Diabetes Endocrinol.* 6 (12) (2018) 944–953.
- [102] Q. Cao, S. Yu, W. Xiong, Y. Li, H. Li, J. Li, F. Li, Waist-hip ratio as a predictor of myocardial infarction risk: A systematic review and meta-analysis, *Medicine* 97 (30) (2018).
- [103] G. Vazquez, S. Duval, D.R. Jacobs Jr., K. Silventoinen, Comparison of body mass index, waist circumference, and waist/hip ratio in predicting incident diabetes: a meta-analysis, *Epidemiol. Rev.* 29 (1) (2007) 115–128.
- [104] J. Chang, A. Ko, S.M. Park, S. Choi, K. Kim, S.M. Kim, J.M. Yun, U. Kang, I.H. Shin, J.Y. Shin, et al., Association of cardiovascular mortality and deep learning-funduscopic atherosclerosis score derived from retinal fundus images, *Am. J. Ophthalmol.* 217 (2020) 121–130.
- [105] C.Y. Cheung, D. Xu, C.-Y. Cheng, C. Sabanayagam, Y.-C. Tham, M. Yu, T.H. Rim, C.Y. Chai, B. Gopinath, P. Mitchell, et al., A deep-learning system for the assessment of cardiovascular disease risk via the measurement of retinal-vessel calibre, *Nat. Biomed. Eng.* 5 (6) (2021) 498–508.
- [106] T.H. Rim, C.J. Lee, Y.-C. Tham, N. Cheung, M. Yu, G. Lee, Y. Kim, D.S. Ting, C.C.Y. Chong, Y.S. Choi, et al., Deep-learning-based cardiovascular risk stratification using coronary artery calcium scores predicted from retinal photographs, *Lancet Digit. Health* 3 (5) (2021) e306–e316.
- [107] H. Dai, T.A. Alsalhe, N. Chalghaf, M. Ricciò, N.L. Bragazzi, J. Wu, The global burden of disease attributable to high body mass index in 195 countries and territories, 1990–2017: An analysis of the Global Burden of Disease Study, *PLoS Med.* 17 (7) (2020) e1003198.
- [108] T.Y. Wong, A. Kamineni, R. Klein, A.R. Sharrett, B.E. Klein, D.S. Siscovich, M. Cushman, B.B. Duncan, Quantitative retinal venular caliber and risk of cardiovascular disease in older persons: the cardiovascular health study, *Arch. Internal Med.* 166 (21) (2006) 2388–2394.
- [109] S.B. Seidelmann, B. Claggett, P.E. Bravo, A. Gupta, H. Farhad, B.E. Klein, R. Klein, M. Di Carli, S.D. Solomon, Retinal vessel calibers in predicting long-term cardiovascular outcomes: the atherosclerosis risk in communities study, *Circulation* 134 (18) (2016) 1328–1338.
- [110] R. Detrano, A.D. Guerci, J.J. Carr, D.E. Bild, G. Burke, A.R. Folsom, K. Liu, S. Shea, M. Szkoł, D.A. Bluemke, et al., Coronary calcium as a predictor of coronary events in four racial or ethnic groups, *N. Engl. J. Med.* 358 (13) (2008) 1336–1345.
- [111] A. Mitani, A. Huang, S. Venugopalan, G.S. Corrado, L. Peng, D.R. Webster, N. Hammel, Y. Liu, A.V. Varadarajan, Detection of anaemia from retinal fundus images via deep learning, *Nat. Biomed. Eng.* 4 (1) (2020) 18–27.
- [112] J. Tian, G. Smith, H. Guo, B. Liu, Z. Pan, Z. Wang, S. Xiong, R. Fang, Modular machine learning for Alzheimer's disease classification from retinal vasculature, *Sci. Rep.* 11 (1) (2021) 1–11.
- [113] K. Kisler, A.R. Nelson, A. Montagne, B.V. Zlokovic, Cerebral blood flow regulation and neurovascular dysfunction in Alzheimer disease, *Nat. Rev. Neurosci.* 18 (7) (2017) 419–434.
- [114] J. Benson, T. Estrada, M. Burge, P. Soliz, Diabetic peripheral neuropathy risk assessment using digital fundus photographs and machine learning, in: 2020 42nd Annual International Conference of the IEEE Engineering in Medicine & Biology Society, EMBC, IEEE, 2020, pp. 1988–1991.
- [115] D.R. Cervera, L. Smith, L. Diaz-Santana, M. Kumar, R. Raman, S. Sivaprasad, Identifying peripheral neuropathy in colour fundus photographs based on deep learning, *Diagnostics* 11 (11) (2021) 1943.
- [116] C. Sabanayagam, D. Xu, D.S. Ting, S. Nusinovici, R. Banu, H. Hamzah, C. Lim, Y.-C. Tham, C.Y. Cheung, E.S. Tai, et al., A deep learning algorithm to detect chronic kidney disease from retinal photographs in community-based populations, *Lancet Digit. Health* 2 (6) (2020) e295–e302.
- [117] K. Zhang, X. Liu, J. Xu, J. Yuan, W. Cai, T. Chen, K. Wang, Y. Gao, S. Nie, X. Xu, et al., Deep-learning models for the detection and incidence prediction of chronic kidney disease and type 2 diabetes from retinal fundus images, *Nat. Biomed. Eng.* 5 (6) (2021) 533–545.
- [118] W. Xiao, X. Huang, J.H. Wang, D.R. Lin, Y. Zhu, C. Chen, Y.H. Yang, J. Xiao, L.Q. Zhao, J.-P.O. Li, et al., Screening and identifying hepatobiliary diseases through deep learning using ocular images: a prospective, multicentre study, *Lancet Digit. Health* 3 (2) (2021) e88–e97.
- [119] P.J. Saine, M.E. Tyler, *Ophthalmic Photography: Retinal Photography, Angiography, and Electronic Imaging*, Vol. 132, Butterworth-Heinemann Boston, 2002.
- [120] A.G. Marrugo, M.S. Millan, Retinal image analysis: Image processing and feature extraction oriented to the clinical task, *Opt. Pura Apl.* 50 (1) (2017) 49–62.
- [121] N. Panwar, P. Huang, J. Lee, P.A. Keane, T.S. Chuan, A. Richhariya, S. Teoh, T.H. Lim, R. Agrawal, Fundus photography in the 21st century—a review of recent technological advances and their implications for worldwide healthcare, *Telemed. E-Health* 22 (3) (2016) 198–208.
- [122] M.E. Tyler, L. Hubbard, K. Boydston, A. Pugliese, Characteristics of digital fundus camera systems affecting tonal resolution in color retinal images, *J. Ophthalmic Photogr.* 31 (1) (2009) 1–9.
- [123] J.S. Wolffsohn, *Ophthalmic Imaging*, Vol. 186, Elsevier Ltd., 2008.
- [124] W. Jackman, J. Webster, On photographing the eye of the living human retina, *Phil. Photogr.* 23 (1886) 340–341.
- [125] L.A. Yannuzzi, *The Retinal Atlas*, Elsevier Health Sci., 2010.
- [126] D.D. Donaldson, A new camera for stereoscopic fundus photography, *Trans. Amer. Ophthalmol. Soc.* 62 (1964) 429.
- [127] P. Hansell, E.J.G. Beeson, Retinal photography in colour, *Br. J. Ophthalmol.* 37 (2) (1953) 65.
- [128] T. Behrendt, L.A. Wilson, Spectral reflectance photography of the retina, *Amer. J. Ophthalmol.* 59 (6) (1965) 1079–1088.
- [129] B. Dobbin, Kodak engineer had revolutionary idea: The first digital camera, 2005, Seattlepi. com.
- [130] F. LaRocca, D. Nankivil, S. Farsiu, J.A. Izatt, Handheld simultaneous scanning laser ophthalmoscopy and optical coherence tomography system, *Biomed. Opt. Express* 4 (11) (2013) 2307–2321.
- [131] R. Kingslake, *Applied Optics and Optical Eng.*, Vol. 6, Elsevier, 2012.
- [132] T.M. Shibata N, Fundus camera, 2002, U.S. Patent Application 20020067919.
- [133] K. Tran, T.A. Mendel, K.L. Holbrook, P.A. Yates, Construction of an inexpensive, hand-held fundus camera through modification of a consumer “point-and-shoot” camera, *Investig. Ophthalmol. Vis. Sci.* 53 (12) (2012) 7600–7607.
- [134] T. Hellmuth, J. Wei, Method and apparatus for optical coherence tomographic fundus imaging without vignetting, 1996, uS Patent 5, 537, 162.
- [135] L.J. Haddock, D.Y. Kim, S. Mukai, Simple, inexpensive technique for high-quality smartphone fundus photography in human and animal eyes, *J. Ophthalmol.* 2013 (2013).
- [136] Optovue, iCam, 2020, URL <http://optovue.com/icam/>. (Accessed 10 February 2020).
- [137] Forus, 3Nethra, 2020, URL <http://forushealth.com/3nethra-classic.html>. (Accessed 10 February 2020).
- [138] CenterVue, Digital retinography system, 2020, URL https://www.centervue.com/wp-content/uploads/2020/01/CenterVue_DRSPlus_depliantA4_2019_low.pdf. (Accessed 10 February 2020).
- [139] i-Optics, EasyScan, 2020, URL <https://easyscan-test.com/>. (Accessed 08 June 2020).
- [140] Non-mydiatic retinal camera TRC-NW400, 2020, URL https://www.topcon.co.jp/en/eyecare/products/product/diagnostic/trc/TRC-NW400_E.html. (Accessed 08 June 2020).
- [141] zeiss cirrus 6000, 2020, URL https://www.zeiss.com/meditec/int/product-portfolio/optical-coherence-tomography-devices/cirrus-6000-performance-oct.html?home-pers=unpers-home_product_2. (Accessed 08 June 2020).
- [142] non-mydiatic fundus camera nonmyd w3d, 2020, URL <https://www.kowamedical.com/nonmydwx3d.html>. (Accessed 08 June 2020).
- [143] the multifaceted cx-1, 2020, URL <https://eu.medical.canon/eye-care-cx-1/>. (Accessed 08 June 2020).
- [144] california ultra-widefield retinal imaging, 2020, URL <http://www.optos.com/products/california-icg/>. (Accessed 08 June 2020).
- [145] welch allyn panoptic™ ophthalmoscope, 2020, URL <http://intl.welchallyn.com/apps/products/product.jsp?id=11-ac-100-0000000001138>. (Accessed 10 December 2020).
- [146] volk optical inc. volk pictor, 2020, URL <https://www.volks.com/collections/diagnostic-imaging/products/pictor-prestige>. (Accessed 08 June 2020).
- [147] digital medical scope versacam, 2020, URL https://www.nidek-intl.com/product/ophthalmost/versacam/dia_retina/ds-10.html. (Accessed 08 June 2020).
- [148] horus scope portable fundus camera, 2020, URL <https://www.jedmed.com/products/portable-fundus-camera>. (Accessed 08 June 2020).

- [149] optomed aurora, 2020, URL <https://www.optomed.com/wp-content/uploads/2019/10/Aurora-A4-WEB-31102019.pdf>. (Accessed 08 June 2020).
- [150] kowa. genesis-d, 2020, URL <https://ophthalmic.kowa-usa.com/products/retinal-cameras/genesis-d-handheld-retinal-camera-features/>. (Accessed 08 June 2020).
- [151] R.N. Maamari, J.D. Keenan, D.A. Fletcher, T.P. Margolis, A mobile phone-based retinal camera for portable wide field imaging, *Br. J. Ophthalmol.* 98 (4) (2014) 438–441.
- [152] Navitsky C. The portable eye examination kit. *Retina Today*, 2020, URL <http://retinatoday.com/2013/12/the-portable-eye-examination-kit>. (Accessed 08 June 2020).
- [153] Welch allyn. iExaminer, 2020, URL <https://www.welchallyn.com/en/microsites/iexaminer.html>. (Accessed 08 June 2020).
- [154] F.C. Delori, R.H. Webb, D.H. Sliney, Maximum permissible exposures for ocular safety (ANSI 2000), with emphasis on ophthalmic devices, *J. Opt. Soc. Amer. A* 24 (5) (2007) 1250–1265.
- [155] A. McAndrew, An Introduction to Digital Image Processing with Matlab Notes for scm2511 Image Processing, Vol. 264 (1), School of Comput. Sci. and Mathematics, Victoria University of Technol., 2004, pp. 1–264.
- [156] T.J. Bennett, J. Strong, The effects of gain and noise in fundus autofluorescence imaging, *J. Ophthalmic Photogr.* 27 (2007) 87–92.
- [157] A.J. Theuwissen, CMOS image sensors: State-of-the-art, *Solid-State Electron.* 52 (9) (2008) 1401–1406.
- [158] R.D. Gow, D. Renshaw, K. Findlater, L. Grant, S.J. McLeod, J. Hart, R.L. Nicola, A comprehensive tool for modeling CMOS image-sensor-noise performance, *IEEE Trans. Electron Devices* 54 (6) (2007) 1321–1329.
- [159] K. Naveed, S. Ehsan, K.D. McDonald-Maier, N. Ur Rehman, A multiscale denoising framework using detection theory with application to images from CMOS/CCD sensors, *Sensors* 19 (1) (2019) 206.
- [160] A.S. Ashour, Y. Guo, Advanced optimization-based neutrosophic sets for medical image denoising, in: *Neutrosophic Set in Med. Image Anal.*, Elsevier, 2019, pp. 101–121.
- [161] A. Khawaja, T.M. Khan, K. Naveed, S.S. Naqvi, N.U. Rehman, S.J. Nawaz, An improved retinal vessel segmentation framework using frangi filter coupled with the probabilistic patch based denoiser, *IEEE Access* 7 (2019) 164344–164361.
- [162] A.F.M. Hani, T.A. Soomro, I. Fayee, N. Kamel, N. Yahya, Identification of noise in the fundus images, in: Proc. of IEEE Intl. Conf. on Control Syst., Comput. and Eng., 2013, pp. 191–196.
- [163] A.A.G. Elseid, M.E. Elmanna, A.O. Hamza, Evaluation of spatial filtering techniques in retinal fundus images, *Amer. J. Artif. Intell.* 2 (2) (2018) 16.
- [164] S.V. Vaseghi, *Advanced Digital Signal Processing and Noise Reduction*, John Wiley & Sons, 2008.
- [165] C. Boncelet, Image noise models, in: *The Essential Guide to Image Process.*, Elsevier, 2009, pp. 143–167.
- [166] A.K. Boyat, B.K. Joshi, A review paper: noise models in digital image processing, 2015, arXiv preprint [arXiv:1505.03489](https://arxiv.org/abs/1505.03489).
- [167] N. ur Rehman, K. Naveed, S. Ehsan, K. McDonald-Maier, Multi-scale image denoising based on goodness of fit (GOF) tests, in: European Signal Process. Conf., EUSIPCO, IEEE, 2016, pp. 1548–1552.
- [168] K. Naveed, B. Shaukat, S. Ehsan, K.D. McDonald-Maier, N. Ur Rehman, Multiscale image denoising using goodness-of-fit test based on EDF statistics, *PLoS One* 14 (5) (2019) e0216197.
- [169] A.C. Bovik, *The Essential Guide to Image Processing*, Academic Press, 2009.
- [170] C. Charles, J.-P. Rasson, Wavelet denoising of Poisson-distributed data and applications, *Comput. Stat. Data Anal.* 43 (2) (2003) 139–148.
- [171] F. Luisier, T. Blu, M. Unser, Image denoising in mixed Poisson–Gaussian noise, *IEEE Trans. Image Process.* 20 (3) (2010) 696–708.
- [172] D. Guo, X. Qu, X. Du, K. Wu, X. Chen, Salt and pepper noise removal with noise detection and a patch-based sparse representation, *Adv. Multimedia* 2014 (2014).
- [173] J.C. Dainty, I. The statistics of speckle patterns, in: *Progress in Optics*, Vol. 14, Elsevier, 1977, pp. 1–46.
- [174] A.P. Witkin, Scale-space filtering, in: *Readings in Comput. Vision*, Elsevier, 1987, pp. 329–332.
- [175] D.H. Shin, R.H. Park, S. Yang, J.-H. Jung, Block-based noise estimation using adaptive Gaussian filtering, *IEEE Trans. Consum. Electron.* 51 (1) (2005) 218–226.
- [176] J. Babaud, A.P. Witkin, M. Baudin, R.O. Duda, Uniqueness of the Gaussian kernel for scale-space filtering, *IEEE Trans. Pattern Anal. Mach. Intell.* (1) (1986) 26–33.
- [177] T.M. Khan, D.G. Bailey, M.A. Khan, Y. Kong, Efficient hardware implementation for fingerprint image enhancement using anisotropic Gaussian filter, *IEEE Trans. Image Process.* 26 (5) (2017) 2116–2126.
- [178] G. Deng, L. Cahill, An adaptive Gaussian filter for noise reduction and edge detection, in: Proc. of IEEE Conf. Record Nuclear Sci. Symposium and Med. Imaging, IEEE, 1993, pp. 1615–1619.
- [179] C. Tomasi, R. Manduchi, Bilateral filtering for gray and color images, in: Proc. of Intl. Conf. on Comput. Vision, IEEE, 1998, pp. 839–846.
- [180] P. Perona, J. Malik, Scale-space and edge detection using anisotropic diffusion, *IEEE Trans. Pattern Anal. Mach. Intell.* 12 (7) (1990) 629–639.
- [181] Z. Farbman, R. Fattal, D. Lischinski, R. Szeliski, Edge-preserving decompositions for multi-scale tone and detail manipulation, *ACM Trans. Graph. (TOG)* 27 (3) (2008) 1–10.
- [182] T.M. Khan, M.A. Khan, Y. Kong, Fingerprint image enhancement using multi-scale DDFB based diffusion filters and modified Hong filters, *Optik* 125 (16) (2014) 4206–4214.
- [183] M.A. Khan, T.M. Khan, O. Kittaneh, Y. Kong, Stopping criterion for anisotropic image diffusion, *Optik* 127 (1) (2016) 156–160.
- [184] T.M. Khan, M.A. U Khan, Y. Kong, O. Kittaneh, Stopping criterion for linear anisotropic image diffusion: a fingerprint image enhancement case, *EURASIP J. Image Video Process.* 2016 (1) (2016) 1–20.
- [185] A. Buades, B. Coll, J.-M. Morel, A non-local algorithm for image denoising, in: Proc. of CVPR'05, Vol. 2, IEEE, 2005, pp. 60–65.
- [186] R. Fattal, M. Agrawala, S. Rusinkiewicz, Multiscale shape and detail enhancement from multi-light image collections, *ACM Trans. Graph. (TOG)* 26 (3) (2007) 51.
- [187] H. Kang, S. Lee, C.K. Chui, Flow-based image abstraction, *IEEE Trans. Vis. Comput. Graph.* 15 (1) (2008) 62–76.
- [188] J. Chen, S. Paris, F. Durand, Real-time edge-aware image processing with the bilateral grid, *ACM Trans. Graph. (TOG)* 26 (3) (2007) 103–es.
- [189] G. Lalli, D. Kalamanian, N. Manikandaprabu, S. Brindha, Feature recognition on retinal fundus image—a multi-systemic comparative analysis, *Intl. J. Adv. Res. Comput. Sci. Softw. Eng.* 3 (11) (2013) 427–434.
- [190] J. Xiao, H. Cheng, H. Sawhney, C. Rao, M. Isnardi, Bilateral filtering-based optical flow estimation with occlusion detection, in: Proc. of European Conf. on Comput. Vision, Springer, 2006, pp. 211–224.
- [191] D. Sun, S. Roth, M.J. Black, Secrets of optical flow estimation and their principles, in: Proc. of CVPR'10, IEEE, 2010, pp. 2432–2439.
- [192] A. Manduca, L. Yu, J.D. Trzasko, N. Khaylova, J.M. Kofler, C.M. McCollough, J.G. Fletcher, Projection space denoising with bilateral filtering and CT noise modeling for dose reduction in CT, *Med. Phys.* 36 (11) (2009) 4911–4919.
- [193] C.S. Anand, J. Sahambi, MRI denoising using bilateral filter in redundant wavelet domain, in: Proc. of TENCON, IEEE Region Conf., 2008, pp. 1–6.
- [194] F. Shi, X. Chen, H. Zhao, W. Zhu, D. Xiang, E. Gao, M. Sonka, H. Chen, Automated 3-D retinal layer segmentation of macular optical coherence tomography images with serous pigment epithelial detachments, *IEEE Trans. Med. Imaging* 34 (2) (2014) 441–452.
- [195] N.J. Wade, Image, eye, and retina (invited review), *J. Opt. Soc. Amer. A* 24 (5) (2007) 1229–1249.
- [196] T.A. Soomro, J. Gao, M.A. Khan, T.M. Khan, M. Paul, Role of image contrast enhancement technique for ophthalmologist as diagnostic tool for diabetic retinopathy, in: Proceedings of Intl. Conf. on Digital Image Comput.: Techniques and Appl., IEEE, 2016, pp. 1–8.
- [197] B. Chen, Y. Chen, Z. Shao, T. Tong, L. Luo, Blood vessel enhancement via multi-dictionary and sparse coding: Application to retinal vessel enhancing, *Neurocomputing* 200 (2016) 110–117.
- [198] E. Daniel, J. Anitha, Optimum green plane masking for the contrast enhancement of retinal images using enhanced genetic algorithm, *Optik* 126 (18) (2015) 1726–1730.
- [199] J. Staal, M.D. Abràmoff, M. Niemeijer, M.A. Viergever, B. Van Ginneken, Ridge-based vessel segmentation in color images of the retina, *IEEE Trans. Med. Imaging* 23 (4) (2004) 501–509.
- [200] A. Hoover, V. Kouznetsova, M. Goldbaum, Locating blood vessels in retinal images by piecewise threshold probing of a matched filter response, *IEEE Trans. Med. Imaging* 19 (3) (2000) 203–210.
- [201] J. Odstrcilík, R. Kolar, A. Budai, J. Hornegger, J. Jan, J. Gazarek, T. Kubena, P. Černosek, O. Svoboda, E. Angelopoulou, Retinal vessel segmentation by improved matched filtering: evaluation on a new high-resolution fundus image database, *IET Image Process.* 7 (4) (2013) 373–383.
- [202] The Child Heart and Health Study in England (CHASE), 2020, URL <http://www.chasestudy.ac.uk/>. (Accessed 14 June 2020).
- [203] GlaucomaDB dataset, 2020, URL <http://biomisa.org/index.php/glaucoma-database/>. (Accessed 14 June 2020).
- [204] F. Fumero, S. Alayón, J.L. Sanchez, J. Sigut, M. Gonzalez-Hernandez, RIM-ONE: An open retinal image database for optic nerve evaluation, in: Proceedings of 24th Intl. Symposium on Comput.-Based Med. Syst., IEEE, 2011, pp. 1–6.
- [205] J. Sivaswamy, S. Krishnadas, G.D. Joshi, M. Jain, A.U.S. Tabish, Drishti-gs: Retinal image dataset for optic nerve head (ONH) segmentation, in: Proc. of Intl. Symposium on Biomed. Imaging, IEEE, 2014, pp. 53–56.
- [206] T. Kauppi, V. Kalesnykiene, J.-K. Kamarainen, L. Lensu, I. Sorri, A. Raninen, R. Voutilainen, H. Uusitalo, H. Kälväinen, J. Pietilä, The diaretdb1 diabetic retinopathy database and evaluation protocol, in: BMVC, Vol. 1, 2007, pp. 1–10.
- [207] E. Decencière, X. Zhang, G. Cazuguel, B. Lay, B. Cochener, C. Trone, P. Gain, R. Ordóñez, P. Massin, A. Erginay, et al., Feedback on a publicly distributed image database: the Messidor database, *Image Anal. Stereol.* 33 (3) (2014) 231–234.
- [208] C.C. Sng, L.-L. Foo, C.-Y. Cheng, J.C. Allen Jr., M. He, G. Krishnaswamy, M.E. Nongpiur, D.S. Friedman, T.Y. Wong, T. Aung, Determinants of anterior chamber depth: the Singapore Chinese Eye Study, *Ophthalmology* 119 (6) (2012) 1143–1150.

- [209] Z. Zhang, F.S. Yin, J. Liu, W.K. Wong, N.M. Tan, B.H. Lee, J. Cheng, T.Y. Wong, Orig-a-light: An online retinal fundus image database for glaucoma analysis and research, in: Proc. of Annual Intl. Conf. of the Eng. in Medicine and Biology, IEEE, 2010, pp. 3065–3068.
- [210] F. Huazhu, L. Fei, J.I. Orlando, B. Hrvoje, S. Xu, L. Jingan, X. Yanwu, Z. Shaochong, Z. Xiulan, REFUGE: Retinal Fundus Glaucoma Challenge, IEEE, 2019, <http://dx.doi.org/10.21227/tz6e-r977>.
- [211] E. Decenciere, G. Cazuguel, X. Zhang, G. Thibault, J.-C. Klein, F. Meyer, B. Marcotegui, G. Quellec, M. Lamard, R. Danno, et al., TeleOphtha: Machine learning and image processing methods for teleophthalmology, Irbm 34 (2) (2013) 196–203.
- [212] HEI-MED Dataset, 2020, URL <https://github.com/lgiancaUTH/HEI-MED>. (Accessed 14 June 2020).
- [213] P. Porwal, S. Pachade, R. Kamble, M. Kokare, G. Deshmukh, V. Sahasrabuddhe, F. Meriaudeau, Indian diabetic retinopathy image dataset (IDRID): a database for diabetic retinopathy screening research, Data 3 (3) (2018) 25.
- [214] Kaggle dataset, 2020, URL <https://www.kaggle.com/c/diabetic-retinopathy-detection/data>. (Accessed 14 June 2020).
- [215] VICAVR database, 2020, URL <http://www.varpa.es/research/ophtalmology.html#vicavr>. (Accessed 14 June 2020).
- [216] B. Al-Diri, A. Hunter, D. Steel, M. Habib, T. Hudaib, S. Berry, A reference data set for retinal vessel profiles, in: Proc. of Annual Intl. Conf. of Eng. in Medicine and Biology Society, IEEE, 2008, pp. 2262–2265.
- [217] M. Niemeijer, B. Ginneken, M. Cree, A. Mizutani, G. Quellec, C. Sanchez, B. Zhang, R. Hornero, M. Lamard, C. Muramatsu, X. Wu, G. Cazuguel, J. You, A. Mayo, Q. Li, Y. Hatanaka, B. Cochener, C. Roux, F. Karray, M. Abramoff, Retinopathy Online Challenge: Automatic detection of microaneurysms in digital color fundus photographs, IEEE Trans. Med. Imaging 29 (2010) 185–195.
- [218] ARIA dataset, 2020, URL <https://github.com/petebankhead/ARIA>. (Accessed 14 June 2020).
- [219] LMD dataset, 2020, URL <https://home.deec.uc.pt/~lcruz/lmd/>. (Accessed 14 June 2020).
- [220] NIE AREDS dataset, 2020, URL <https://www.nih.gov/news-events/news-releases/nih-adds-first-images-major-research-database>. (Accessed 14 June 2020).
- [221] J. Feijoo, J. de la Casa, H. Servet, M. Zamorano, M. Mayoral, E. Suárez, DRIONS-DB: Digital Retinal Images for Optic Nerve Segmentation Database, Academic Press, 2014.
- [222] C. Miller, Z. Nagy, A. Schlueter, A seed dataset for a public, temporal data repository for energy informatics research on commercial building performance, in: Proc. of Conf. on Future Energy Business & Energy Informatics, Rotterdam, Netherlands, 2014, pp. 1–2.
- [223] A. Diaz-Pinto, S. Morales, V. Naranco, T. Köhler, J.M. Mossi, A. Navea, CNNs for automatic glaucoma assessment using fundus images: an extensive validation, Biomed. Eng. 18 (1) (2019) 29.
- [224] A.W. Foong, S.M. Saw, J.L. Loo, S. Shen, S.C. Loon, M. Rosman, T. Aung, D.T. Tan, E.S. Tai, T.Y. Wong, Rationale and methodology for a population-based study of eye diseases in Malay people: The Singapore Malay eye study (SiMES), Ophthalmic Epidemiol. 14 (1) (2007) 25–35.
- [225] C.W. Pan, T.Y. Wong, L. Chang, X.Y. Lin, R. Lavanya, Y.-F. Zheng, Y.-O. Kok, R.-Y. Wu, T. Aung, S.-M. Saw, Ocular biometry in an urban Indian population: the Singapore Indian Eye Study (SINDI), Investig. Ophthal. Vis. Sci. 52 (9) (2011) 6636–6642.
- [226] D.F. Shaik, M. Prasad, J. Rao, A. Rahim, A. SomaSekhar, Medical Image Analysis of Electron Micrographs in Diabetic Patients Using Contrast Enhancement, IEEE, 2010, pp. 482–485.
- [227] T.M. Khan, D.G. Bailey, M.A. Khan, Y. Kong, Efficient hardware implementation strategy for local normalization of fingerprint images, J. Real-Time Image Process. (2016) 1–13.
- [228] T. Jintasuttisak, S. Intajag, Color retinal image enhancement by Rayleigh contrast-limited adaptive histogram equalization, in: Proc. of Intl. Conf. on Control, Automation and Syst., IEEE, 2014, pp. 692–697.
- [229] M. Liao, Y.-q. Zhao, X.-h. Wang, P.-s. Dai, Retinal vessel enhancement based on multi-scale top-hat transformation and histogram fitting stretching, Opt. Laser Technol. 58 (2014) 56–62.
- [230] K. Zuiderveld, Contrast limited adaptive histogram equalization, Graph. Gems (1994) 474–485.
- [231] A.W. Setiawan, T.R. Mengko, O.S. Santoso, A.B. Suksmono, Color retinal image enhancement using CLAHE, in: Proc. of Intl. Conf. on ICT for Smart Society, IEEE, 2013, pp. 1–3.
- [232] T. Walter, P. Massin, A. Erginay, R. Ordóñez, C. Jeulin, J.-C. Klein, Automatic detection of microaneurysms in color fundus images, Med. Image Anal. 11 (6) (2007) 555–566.
- [233] G.D. Joshi, J. Sivaswamy, Colour retinal image enhancement based on domain knowledge, in: Proc. of Indian Conf. on Comput. Vision, Graphics & Image Process., IEEE, 2008, pp. 591–598.
- [234] J.C. Russ, J.R. Matey, A.J. Mallinckrodt, S. McKay, The image processing handbook, Comput. Phys. 8 (2) (1994) 177–178.
- [235] R. Guillemaud, Uniformity correction with homomorphic filtering on region of interest, in: Proc. of Intl. Conf. on Image Process., Vol. 2, IEEE, 1998, pp. 872–875.
- [236] D.L. Pham, J.L. Prince, Adaptive fuzzy segmentation of magnetic resonance images, IEEE Trans. Med. Imaging 18 (9) (1999) 737–752.
- [237] K. Skifstad, R. Jain, Illumination independent change detection for real world image sequences, Comput. Vis. Graph. Image Process. 46 (3) (1989) 387–399.
- [238] M.D. Vlachos, E.S. Dermatas, Non-uniform illumination correction in infrared images based on a modified fuzzy c-means algorithm, J. Biomed. Graph. Comput. 3 (1) (2013) 6.
- [239] R.C. Gonzales, R.E. Woods, Digital Image Processing, Prentice hall New Jersey, 2002.
- [240] G. Finlayson, S. Hordley, Improving gamut mapping color constancy, IEEE Trans. Image Process. 9 (10) (2000) 1774–1783.
- [241] D.J. Jobson, Z.-u. Rahman, G.A. Woodell, Properties and performance of a center/surround retinex, IEEE Trans. Image Process. 6 (3) (1997) 451–462.
- [242] B. Li, S. Wang, Y. Geng, Image enhancement based on Retinex and lightness decomposition, in: Proc. of Intl. Conf. on Image Process., IEEE, 2011, pp. 3417–3420.
- [243] E. Grisan, A. Giani, E. Ceseracciu, A. Ruggeri, Model-based illumination correction in retinal images, in: Proc. of Intl. Symposium on Biomed. Imaging, IEEE, 2006, pp. 984–987.
- [244] R. Kolar, J. Odstrcilik, J. Jan, V. Harabis, Illumination correction and contrast equalization in colour fundus images, in: Proc. of European Signal Process. Conf., IEEE, 2011, pp. 298–302.
- [245] H. Niemann, R. Chrastek, B. Lausen, L. Kubacka, J. Jan, C.Y. Mardin, G. Michelson, Towards automated diagnostic evaluation of retina images, Pattern Recog. Image Anal. 16 (4) (2006) 671–676.
- [246] H. Narasimha-Iyer, A. Can, B. Roysam, V. Stewart, H.L. Tanenbaum, A. Majerovics, H. Singh, Robust detection and classification of longitudinal changes in color retinal fundus images for monitoring diabetic retinopathy, IEEE Trans. Biomed. Eng. 53 (6) (2006) 1084–1098.
- [247] M. Foracchia, E. Grisan, A. Ruggeri, Luminosity and contrast normalization in retinal images, Med. Image Anal. 9 (3) (2005) 179–190.
- [248] C. Leahy, A. O'Brien, C. Dainty, Illumination correction of retinal images using Laplace interpolation, Appl. Opt. 51 (35) (2012) 8383–8389.
- [249] Y. Zheng, B. Vanderbeek, R. Xiao, E. Daniel, D. Stambolian, M. Maguire, J. O'Brien, J. Gee, Retrospective illumination correction of retinal fundus images from gradient distribution sparsity, in: Proc. of Intl. Symposium on Biomed. Imaging, IEEE, 2012, pp. 972–975.
- [250] E.S. Varnousfaderani, S. Yousefi, A. Belghith, M.H. Goldbaum, Luminosity and contrast normalization in color retinal images based on standard reference image, in: Med. Imaging: Image Process., 9784, Intl. Society for Optics and Photonics, 2016, p. 97843N.
- [251] E. Decencière, X. Zhang, G. Cazuguel, B. Lay, B. Cochener, C. Trone, P. Gain, R. Ordóñez, P. Massin, A. Erginay, et al., Feedback on a publicly distributed image database: the Messidor database, Image Anal. Stereol. 33 (3) (2014) 231–234.
- [252] D. Kumar, A. Pramanik, S.S. Kar, S.P. Maity, Retinal blood vessel segmentation using matched filter and Laplacian of Gaussian, in: Proc. of Intl. Conf. on Signal Process. and Commu., IEEE, 2016, pp. 1–5.
- [253] J. Rodrigues, N. Bezerra, Retinal vessel segmentation using parallel grayscale skeletonization algorithm and mathematical morphology, in: Proc. of SIBGRAPI Conf. on Graphics, Patterns and Images, IEEE, 2016, pp. 17–24.
- [254] T.A. Soomro, M.A. Khan, J. Gao, T.M. Khan, M. Paul, N. Mir, Automatic retinal vessel extraction algorithm, in: Proc. of Intl. Conf. on Digital Image Comput.: Techniques and Appl., IEEE, 2016, pp. 1–8.
- [255] D.A. Dharmawan, B.P. Ng, A new two-dimensional matched filter based on the modified Chebyshev type I function for retinal vessels detection, in: Proc. of Annual Intl. Conf. of the Eng. in Medicine and Biology Society, IEEE, 2017, pp. 369–372.
- [256] X. Gao, Y. Cai, C. Qiu, Y. Cui, Retinal blood vessel segmentation based on the Gaussian matched filter and U-net, in: Proc. of Intl. Congress on Image, Signal Process., Biomed. Eng. and Informatics, IEEE, 2017, pp. 1–5.
- [257] J. Elson, J. Precilla, P. Reshma, N.S. Madhavaraja, Automated extraction and analysis of retinal blood vessels with multi scale matched filter, in: Proc. of Intl. Conf. on Intell. Comput., Instrumentation and Control Technol., IEEE, 2017, pp. 775–779.
- [258] L.C. Rodrigues, M. Marengoni, Segmentation of optic disc and blood vessels in retinal images using wavelets, mathematical morphology and Hessian-based multi-scale filtering, Biomed. Signal Process. Control 36 (2017) 39–49.
- [259] T.A. Soomro, M.A. Khan, J. Gao, T.M. Khan, M. Paul, Contrast normalization steps for increased sensitivity of a retinal image segmentation method, Signal Image Video Process. 11 (8) (2017) 1509–1517.
- [260] T.A. Soomro, A.J. Afifi, J. Gao, O. Hellwich, M.A. Khan, M. Paul, L. Zheng, Boosting sensitivity of a retinal vessel segmentation algorithm with convolutional neural network, in: Proc. of Intl. Conf. on Digital Image Comput.: Techniques and Appl., IEEE, 2017, pp. 1–8.
- [261] P.K. Karn, B. Biswal, S.R. Samantaray, Robust retinal blood vessel segmentation using hybrid active contour model, IET Image Process. 13 (3) (2018) 440–450.
- [262] K.B. Khan, A.A. Khaliq, A. Jalil, M. Shahid, A robust technique based on VLM and frangi filter for retinal vessel extraction and denoising, PLoS One 13 (2) (2018) e0192203.

- [263] T.A. Soomro, T.M. Khan, M.A. Khan, J. Gao, M. Paul, L. Zheng, Impact of ICA-based image enhancement technique on retinal blood vessels segmentation, *IEEE Access* 6 (2018) 3524–3538.
- [264] M.A. Khan, T.M. Khan, D.G. Bailey, T.A. Soomro, A generalized multi-scale line-detection method to boost retinal vessel segmentation sensitivity, *Pattern Anal. Appl.* 22 (3) (2019) 1177–1196.
- [265] M. Hashemzadeh, B. Adlpour Azar, Retinal blood vessel extraction employing effective image features and combination of supervised and unsupervised machine learning methods, *Artif. Intell. Med.* 95 (2019) 1–15.
- [266] M. Mehmood, T.M. Khan, M.A. Khan, S.S. Naqvi, W. Alhalabi, Vessel intensity profile uniformity improvement for retinal vessel segmentation, *Procedia Comput. Sci.* 163 (2019) 370–380.
- [267] A. Khawaja, T.M. Khan, M.A. Khan, S.J. Nawaz, A multi-scale directional line detector for retinal vessel segmentation, *Sensors (Switzerland)* 19 (22) (2019) 1–22.
- [268] T.M. Khan, M.A. Khan, N.U. Rehman, K. Naveed, I.U. Afridi, S.S. Naqvi, I. Raazak, Width-wise vessel bifurcation for improved retinal vessel segmentation, *Biomed. Signal Process. Control* 71 (2022) 103169.
- [269] N. Muzammil, S.A.A. Shah, A. Shahzad, M.A. Khan, R.M. Ghoniem, Multifilters-based unsupervised method for retinal blood vessel segmentation, *Appl. Sci.* 12 (13) (2022) 6393.
- [270] S. Mahapatra, S. Agrawal, P.K. Mishro, R.B. Pachori, A novel framework for retinal vessel segmentation using optimal improved frangi filter and adaptive weighted spatial FCM, *Comput. Biol. Med.* (2022) 105770.
- [271] L. Ngo, J.-H. Han, Multi-level deep neural network for efficient segmentation of blood vessels in fundus images, *Electron. Lett.* 53 (16) (2017) 1096–1098.
- [272] Y. Guo, Ü. Budak, L.J. Vespa, E. Khorasani, A. Şengür, A retinal vessel detection approach using convolution neural network with reinforcement sample learning strategy, *Meas.: J. Intl. Meas. Confed.* 125 (2018) 586–591.
- [273] Y. Lu, Y. Zhou, J. Qin, A convolutional encoder-decoder architecture for retinal blood vessel segmentation in fundus images, in: Proc. of Intl. Conf. on Syst. and Informatics, IEEE, 2018, pp. 1071–1075.
- [274] H. Xia, R. Zhuge, H. Li, Retinal vessel segmentation via a coarse-to-fine convolutional neural network, in: Proc. of Intl. Conf. on Bioinformatics and Biomedicine, IEEE, 2018, pp. 1036–1039.
- [275] R. Xu, G. Jiang, X. Ye, Y.-W. Chen, Retinal vessel segmentation via multiscaled deep-guidance, in: Proc. of Pacific Rim Conf. on Multimedia, Springer, 2018, pp. 158–168.
- [276] Y. Guo, Ü. Budak, A. Şengür, A novel retinal vessel detection approach based on multiple deep convolution neural networks, *Comput. Methods Progr. Biomed.* 167 (2018) 43–48.
- [277] Y. Lin, H. Zhang, G. Hu, Automatic retinal vessel segmentation via deeply supervised and smoothly regularized network, *IEEE Access* 7 (2018) 57717–57724.
- [278] A. Oliveira, S. Pereira, C.A. Silva, Retinal vessel segmentation based on Fully Convolutional Neural Networks, *Expert Syst. Appl.* 112 (2018) 229–242, arXiv: 1812.07110.
- [279] K. Hu, Z. Zhang, X. Niu, Y. Zhang, C. Cao, F. Xiao, X. Gao, Retinal vessel segmentation of color fundus images using multiscale convolutional neural network with an improved cross-entropy loss function, *Neurocomputing* 309 (2018) 179–191.
- [280] S. Guo, K. Wang, H. Kang, Y. Zhang, Y. Gao, T. Li, BTS-DSN: Deeply supervised neural network with short connections for retinal vessel segmentation, *Intl. J. Med. Inform.* 126 (2019) 105–113.
- [281] Z. Yan, X. Yang, K.-T. Cheng, A three-stage deep learning model for accurate retinal vessel segmentation, *IEEE J. Biomed. Health Inform.* 23 (4) (2018) 1427–1436.
- [282] Q. Jin, Q. Chen, Z. Meng, B. Wang, R. Su, Construction of retinal vessel segmentation models based on convolutional neural network, *Neural Process. Lett.* 52 (2) (2020) 1005–1022.
- [283] Q. Jin, Z. Meng, T.D. Pham, Q. Chen, L. Wei, R. Su, DUNet: A deformable network for retinal vessel segmentation, *Knowl.-Based Syst.* 178 (2019) 149–162.
- [284] D. Yang, M. Ren, B. Xu, Retinal blood vessel segmentation with improved convolutional neural networks, *J. Med. Imaging Health Inform.* 9 (6) (2019) 1112–1118.
- [285] J. Son, S.J. Park, K.-H. Jung, Towards accurate segmentation of retinal vessels and the optic disc in fundoscopic images with generative adversarial networks, *J. Digit. Imaging* 32 (3) (2019) 499–512.
- [286] C. Wang, Z. Zhao, Q. Ren, Y. Xu, Y. Yu, Dense U-net based on patch-based learning for retinal vessel segmentation, *Entropy* 21 (2) (2019) 168.
- [287] L. Geng, L. Qiu, J. Wu, Z. Xiao, F. Zhang, Segmentation of retinal image vessels based on fully convolutional network with depthwise separable convolution and channel weighting, *J. Biomed. Eng.* 36 (1) (2019) 107–115.
- [288] D.A. Dharmawan, D. Li, B.P. Ng, S. Rahardja, A new hybrid algorithm for retinal vessels segmentation on fundus images, *IEEE Access* 7 (2019) 41885–41896.
- [289] A. Hatamizadeh, H. Hosseini, Z. Liu, S.D. Schwartz, D. Terzopoulos, Deep dilated convolutional nets for the automatic segmentation of retinal vessels, 2019, arXiv preprint arXiv:1905.12120.
- [290] Z. Fan, J. Mo, B. Qiu, W. Li, G. Zhu, C. Li, J. Hu, Y. Rong, X. Chen, Accurate retinal vessel segmentation via octave convolution neural network, 2019, arXiv preprint arXiv:1906.12193.
- [291] A. Ribeiro, A.P. Lopes, C.A. Silva, Ensemble learning approaches for retinal vessel segmentation, in: Proc. of Portuguese Meeting on Bioengineering, IEEE, 2019, pp. 1–4.
- [292] K.J. Noh, S.J. Park, S. Lee, Scale-space approximated convolutional neural networks for retinal vessel segmentation, *Comput. Methods Progr. Biomed.* 178 (2019) 237–246.
- [293] T.A. Soomro, A.J. Afifi, J. Gao, O. Hellwich, L. Zheng, M. Paul, Strided fully convolutional neural network for boosting the sensitivity of retinal blood vessels segmentation, *Expert Syst. Appl.* 134 (2019) 36–52.
- [294] Y. Jiang, N. Tan, T. Peng, H. Zhang, Retinal vessels segmentation based on dilated multi-scale convolutional neural network, *IEEE Access* 7 (2019) 76342–76352.
- [295] M.A. Khan, T.M. Khan, S.S. Naqvi, M. Aurangzeb Khan, GGM classifier with multi-scale line detectors for retinal vessel segmentation, *Signal Image Video Process.* 13 (8) (2019) 1667–1675.
- [296] S. Feng, Z. Zhuo, D. Pan, Q. Tian, CcNet: A cross-connected convolutional network for segmenting retinal vessels using multi-scale features, *Neurocomputing* 392 (2020) 268–276.
- [297] T.M. Khan, M. Alhussein, K. Aurangzeb, M. Arsalan, S.S. Naqvi, S.J. Nawaz, Residual connection-based encoder decoder network (RCED-net) for retinal vessel segmentation, *IEEE Access* 8 (2020) 131257–131272.
- [298] Y. Jiang, J. Liang, T. Cheng, Y. Zhang, X. Lin, J. Dong, MCPANet: multi-scale cross-position attention network for retinal vessel image segmentation, *Symmetry* 14 (7) (2022) 1357.
- [299] T. Zhang, J. Li, Y. Zhao, N. Chen, H. Zhou, H. Xu, Z. Guan, C. Yang, L. Xue, R. Chen, et al., MC-UNet multi-module concatenation based on U-shape network for retinal blood vessels segmentation, 2022, arXiv preprint arXiv:2204.03213.
- [300] M.A. Khan, N. Mir, A. Sarirete, M.R. Nasir, M.M. Abdelaizim, M.Z. Yasin, Optic disc detection and segmentation with vessel convergence and elliptical symmetry evidences, *Procedia Comput. Sci.* 163 (2019) 609–617.
- [301] T.A. Soomro, J. Gao, T. Khan, A.F.M. Hani, M.A. Khan, M. Paul, Computerised approaches for the detection of diabetic retinopathy using retinal fundus images: a survey, *Pattern Anal. Appl.* 20 (4) (2017) 927–961.
- [302] Z. Fan, J.-J. Mo, Automated blood vessel segmentation based on de-noising auto-encoder and neural network, in: Proc. of Intl. Conf. on Mach. Learning and Cybernetics, Vol. 2, IEEE, 2016, pp. 849–856.
- [303] E. Tuba, L. Mrkela, M. Tuba, Retinal blood vessel segmentation by support vector machine classification, in: Proc. of Intl. Conf. RADIOELEKTRONIKA, IEEE, 2017, pp. 1–6.
- [304] Z. Feng, J. Yang, L. Yao, Patch-based fully convolutional neural network with skip connections for retinal blood vessel segmentation, in: Proc. of Intl. Conf. on Image Process., IEEE, 2017, pp. 1742–1746.
- [305] J. Song, B. Lee, Development of automatic retinal vessel segmentation method in fundus images via convolutional neural networks, in: Proc. of Annual Intl. Conf. of Eng. in Medicine and Biology Society, IEEE, 2017, pp. 681–684.
- [306] A. Dasgupta, S. Singh, A fully convolutional neural network based structured prediction approach towards the retinal vessel segmentation, in: Proc. of Intl. Symposium on Biomed. Imaging, IEEE, 2017, pp. 248–251.
- [307] S. Thangaraj, V. Periyasamy, R. Balaji, Retinal vessel segmentation using neural network, *IET Image Process.* 12 (5) (2017) 669–678.
- [308] K. Aurangzeb, S.I. Haider, M. Alhussein, Retinal vessel segmentation based on the anam-net model, *Elektron. Elektrotech.* 28 (3) (2022) 54–64.
- [309] Y. Jiang, J. Liang, T. Cheng, X. Lin, Y. Zhang, J. Dong, MTPA_Unet: multi-scale transformer-position attention retinal vessel segmentation network joint transformer and CNN, *Sensors* 22 (12) (2022) 4592.
- [310] D. Chen, W. Yang, L. Wang, S. Tan, J. Lin, W. Bu, PCAT-UNet: Unet-like network fused convolution and transformer for retinal vessel segmentation, *PLoS One* 17 (1) (2022) e0262689.
- [311] J. Li, R. Li, R. Han, S. Wang, Self-relabeling for noise-tolerant retina vessel segmentation through label reliability estimation, *BMC Med. Imaging* 22 (1) (2022) 1–12.
- [312] U. Raghavendra, S.V. Bhandary, A. Gudigar, U.R. Acharya, Novel expert system for glaucoma identification using non-parametric spatial envelope energy spectrum with fundus images, *Biocybern. Biomed. Eng.* 38 (1) (2018) 170–180.
- [313] T. Kausu, V.P. Gopi, K.A. Wahid, W. Doma, S.I. Niwas, Combination of clinical and multiresolution features for glaucoma detection and its classification using fundus images, *Biocybern. Biomed. Eng.* 38 (2) (2018) 329–341.
- [314] R. Panda, N. Puhan, G. Panda, Mean curvature and texture constrained composite weighted random walk algorithm for optic disc segmentation towards glaucoma screening, *Healthc. Technol. Lett.* 5 (1) (2018) 31–37.
- [315] Z.U. Rehman, S.S. Naqvi, T.M. Khan, M. Arsalan, M.A. Khan, M.A. Khalil, Multi-parametric optic disc segmentation using superpixel based feature classification, *Expert Syst. Appl.* 120 (2019) 461–473.
- [316] U.R. Acharya, S. Bhat, J.E. Koh, S.V. Bhandary, H. Adeli, A novel algorithm to detect glaucoma risk using texton and local configuration pattern features extracted from fundus images, *Comput. Biol. Med.* 88 (2017) 72–83.

- [317] S. Maheshwari, R.B. Pachori, V. Kanhangad, S.V. Bhandary, U.R. Acharya, Iterative variational mode decomposition based automated detection of glaucoma using fundus images, *Comput. Biol. Med.* 88 (2017) 142–149.
- [318] T. Khalil, M.U. Akram, S. Khalid, A. Jameel, Improved automated detection of glaucoma from fundus image using hybrid structural and textural features, *IET Image Process.* 11 (9) (2017) 693–700.
- [319] M.N. Zahoor, M.M. Fraz, A correction to the article “fast optic disc segmentation in retina using polar transform”, *IEEE Access* 6 (2018) 4845–4849.
- [320] T. Khalil, M.U. Akram, H. Raja, A. Jameel, I. Basit, Detection of glaucoma using cup to disc ratio from spectral domain optical coherence tomography images, *IEEE Access* 6 (2018) 4560–4576.
- [321] S.S. Naqvi, N. Fatima, T.M. Khan, Z.U. Rehman, M.A. Khan, Automatic optic disk detection and segmentation by variational active contour estimation in retinal fundus images, *Signal Image Video Process.* 13 (6) (2019) 1191–1198.
- [322] T.M. Khan, M. Mehmood, S.S. Naqvi, M.F.U. Butt, A region growing and local adaptive thresholding-based optic disc detection, *PLoS One* 15 (1) (2020) 1–16.
- [323] J.I. Orlando, E. Prokofyeva, M. del Fresno, M.B. Blaschko, Convolutional neural network transfer for automated glaucoma identification, in: Proc. of Intl. Symposium on Med. Inf. Process. and Anal., Vol. 10160, Intl. Society for Optics and Photonics, 2017.
- [324] Y. Chai, L. He, Q. Mei, H. Liu, L. Xu, Deep learning through two-branch convolutional neuron network for glaucoma diagnosis, in: Proceedings of Intl. Conf. on Smart Health, Springer, 2017, pp. 191–201.
- [325] J. Zilly, J.M. Buhmann, D. Mahapatra, Glaucoma detection using entropy sampling and ensemble learning for automatic optic cup and disc segmentation, *Comput. Med. Imaging Graph.* 55 (2017) 28–41.
- [326] H. Fu, J. Cheng, Y. Xu, D.W.K. Wong, J. Liu, X. Cao, Joint Optic Disc and Cup Segmentation Based on Multi-Label Deep Network and Polar Transformation, *IEEE Trans. Med. Imaging* 37 (7) (2018) 1597–1605, [arXiv:1801.00926](https://arxiv.org/abs/1801.00926).
- [327] S. Wang, L. Yu, X. Yang, C.-W. Fu, P.-A. Heng, Patch-based output space adversarial learning for joint optic disc and cup segmentation, *IEEE Trans. Med. Imaging* 38 (11) (2019) 2485–2495.
- [328] S.M. Shankaranarayana, K. Ram, K. Mitra, M. Sivaprakasam, Fully Convolutional Networks for Monocular Retinal Depth Estimation and Optic Disc-Cup Segmentation, *IEEE J. Biomed. Health Inform.* 23 (4) (2019) 1417–1426, [arXiv:1902.01040](https://arxiv.org/abs/1902.01040).
- [329] Y. Jiang, N. Tan, T. Peng, Optic disc and cup segmentation based on deep convolutional generative adversarial networks, *IEEE Access* 7 (2019) 64483–64493.
- [330] Y. Gao, X. Yu, C. Wu, W. Zhou, X. Wang, H. Chu, Accurate and efficient segmentation of optic disc and optic cup in retinal images integrating multi-view information, *IEEE Access* 7 (2019) 148183–148197.
- [331] X. Zhao, F. Guo, Y. Mai, J. Tang, X. Duan, B. Zou, L. Jiang, Glaucoma screening pipeline based on clinical measurements and hidden features, *IET Image Process.* 13 (12) (2019) 2213–2223.
- [332] Y. Jiang, L. Duan, J. Cheng, Z. Gu, H. Xia, H. Fu, C. Li, J. Liu, JointRCNN: A region-based convolutional neural network for optic disc and cup segmentation, *IEEE Trans. Biomed. Eng.* 67 (2) (2020) 335–343.
- [333] M. Tabassum, T.M. Khan, M. Arslan, S.S. Naqvi, M. Ahmed, H.A. Madni, J. Mirza, CDED-net: joint segmentation of optic disc and optic cup for glaucoma screening, *IEEE Access* (2020).
- [334] Z. Wang, N. Dong, S.D. Rosario, M. Xu, P. Xie, E.P. Xing, Ellipse detection of optic disc-and-cup boundary in fundus images, in: Proc. of Intl. Symposium on Biomed. Imaging. (Isbi) IEEE, 2019, pp. 601–604.
- [335] J. Almotiri, K. Elleithy, A. Elleithy, A multi-anatomical retinal structure segmentation system for automatic eye screening using morphological adaptive fuzzy thresholding, *J. Transl. Eng. Health Med.* 6 (2018) 1–23.
- [336] J. Kaur, D. Mittal, A generalized method for the segmentation of exudates from pathological retinal fundus images, *Biocybern. Biomed. Eng.* 38 (1) (2018) 27–53.
- [337] E. Saeed, M. Szymkowski, K. Saeed, Z. Mariak, An approach to automatic hard exudate detection in retina color images by a telemedicine system based on the d-eye sensor and image processing algorithms, *Sensors* 19 (3) (2019) 695.
- [338] S. Karkuzhali, D. Manimegalai, Robust intensity variation and inverse surface adaptive thresholding techniques for detection of optic disc and exudates in retinal fundus images, *Biocybern. Biomed. Eng.* 39 (3) (2019) 753–764.
- [339] W. Kusakunniran, Q. Wu, P. Rithipravat, J. Zhang, Three-stages hard exudates segmentation in retinal images, in: Proc. of Intl. Conf. on Inf. Technol. and Electrical Eng., IEEE, 2017, pp. 1–6.
- [340] K. Wisaeng, W. Sa-Ngiamvibool, Improved fuzzy C-means clustering in the process of exudates detection using mathematical morphology, *Soft Comput.* 22 (8) (2018) 2753–2764.
- [341] S.S. Kar, S.P. Maity, Automatic detection of retinal lesions for screening of diabetic retinopathy, *IEEE Trans. Biomed. Eng.* 65 (3) (2017) 608–618.
- [342] D.U.N. Qomariah, H. Tjandrasa, Exudate detection in retinal fundus images using combination of mathematical morphology and Renyi entropy thresholding, in: Proc. of Intl. Conf. on ICTS, 2018, pp. 31–36.
- [343] U. Punniyamoorthy, I. Pushpam, Remote examination of exudates-impact of macular oedema, *Healthc. Technol. Lett.* 5 (4) (2018) 118–123.
- [344] N. Nur, H. Tjandrasa, Exudate Segmentation in Retinal Images of Diabetic Retinopathy Using Saliency Method Based on Region, *J. Phys.: Conf. Ser.* 1108 (1) (2018).
- [345] K. Wisaeng, W. Sa-Ngiamvibool, Exudates detection using morphology mean shift algorithm in retinal images, *IEEE Access* 7 (2019) 11946–11958.
- [346] W. Zhou, C. Wu, Y. Yi, W. Du, Automatic Detection of Exudates in Digital Color Fundus Images Using Superpixel Multi-Feature Classification, *IEEE Access* 5 (1) (2017) 17077–17088.
- [347] M.M. Fraz, W. Jahangir, S. Zahid, M.M. Hamayun, S.A. Barman, Multiscale segmentation of exudates in retinal images using contextual cues and ensemble classification, *Biomed. Signal Process. Control* 35 (2017) 50–62.
- [348] P. Costa, A. Campilho, Convolutional bag of words for diabetic retinopathy detection from eye fundus images, *IPSJ Trans. Comput. Vis. Appl.* 9 (1) (2017) 1–6.
- [349] J.H. Tan, H. Fujita, S. Sivaprasad, S.V. Bhandary, A.K. Rao, K.C. Chua, U.R. Acharya, Automated segmentation of exudates, haemorrhages, microaneurysms using single convolutional neural network, *Inform. Sci.* 420 (2017) 66–76.
- [350] S. Abbasi-Sureshani, B. Dashtbozorg, B.M. ter Haar Romeny, F. Fleuret, Boosted exudate segmentation in retinal images using residual nets, in: *Fetal, Infant and Ophthalmic Med. Image Anal.*, Springer, 2017, pp. 210–218.
- [351] J. Amin, M. Sharif, M. Yasmin, H. Ali, S.L. Fernandes, A method for the detection and classification of diabetic retinopathy using structural predictors of bright lesions, *J. Comput. Sci.* 19 (2017) 153–164.
- [352] C. Lam, C. Yu, L. Huang, D. Rubin, Retinal lesion detection with deep learning using image patches, *Investig. Ophthalmol. Vis. Sci.* 59 (1) (2018) 590–596.
- [353] A.K. Pujitha, J. Sivaswamy, Solution to overcome the sparsity issue of annotated data in medical domain, *Trans. Intell. Technol.* 3 (3) (2018) 153–160.
- [354] S. Guo, K. Wang, H. Kang, T. Liu, Y. Gao, T. Li, Bin loss for hard exudates segmentation in fundus images, *Neurocomputing* 392 (2020) 314–324.
- [355] P. Khojasteh, B. Aliahmad, D.K. Kumar, Fundus images analysis using deep features for detection of exudates, hemorrhages and microaneurysms, *BMC Ophthalmol.* 18 (1) (2018) 1–13.
- [356] P. Khojasteh, L.A. Passos Júnior, T. Carvalho, E. Rezende, B. Aliahmad, J.P. Papa, D.K. Kumar, Exudate detection in fundus images using deeply-learnable features, *Comput. Biol. Med.* 104 (2019) 62–69.
- [357] X. Guo, X. Lu, Q. Liu, X. Che, EMFN: Enhanced Multi-Feature Fusion Network for Hard Exudate Detection in Fundus Images, *IEEE Access* 7 (2019) 176912–176920.
- [358] N. Prabhu, D. Bhoir, U. Rao, Performance analysis of convolutional neural networks for exudate detection in fundus images, in: Proceedings of Intl. Conf. on Intell. Comput. and Commu., Springer, 2019, pp. 371–380.
- [359] H. Wang, G. Yuan, X. Zhao, L. Peng, Z. Wang, Y. He, C. Qu, Z. Peng, Hard exudate detection based on deep model learned information and multi-feature joint representation for diabetic retinopathy screening, *Comput. Methods Progr. Biomed.* 191 (2020) 105398.
- [360] J. Kaur, P. Kaur, UNICConv: An enhanced U-Net based InceptionV3 convolutional model for DR semantic segmentation in retinal fundus images, *Concurr. Comput.: Pract. Exper.* e7138.
- [361] S. Otálora, O. Perdomo, F. González, H. Müller, Training Deep Convolutional Neural Networks with Active Learning for Exudate Classification in Eye Fundus Images BT - Intravascular Imaging and Computer Assisted Stenting, and Large-Scale Annotation of Biomed. Data and Expert Label Synthesis, Springer, 2017, pp. 146–154.
- [362] M.M. Islam, H.C. Yang, T.N. Poly, W.S. Jian, Y.C. (Jack) Li, Deep learning algorithms for detection of diabetic retinopathy in retinal fundus photographs: A systematic review and meta-analysis, *Comput. Methods Progr. Biomed.* 191 (2020) 105320.
- [363] S. Lahmiri, A. Shmuel, Variational mode decomposition based approach for accurate classification of color fundus images with hemorrhages, *Opt. Laser Technol.* 96 (2017) 243–248.
- [364] R. Mumtaz, M. Hussain, S. Sarwar, K. Khan, S. Mumtaz, M. Mumtaz, Automatic detection of retinal hemorrhages by exploiting image processing techniques for screening retinal diseases in diabetic patients, *Intl. J. Diabet. Dev. Countries* 38 (1) (2018) 80–87.
- [365] M. Targaonkar, M. Khambete, Red profile moments for hemorrhage classification in diabetic retinal fundus images, *Pattern Recog. Image Anal.* 29 (2) (2019) 224–229.
- [366] R. Murugan, An automatic detection of hemorrhages in retinal fundus images by motion pattern generation, *J. Biomed. Pharmacol.* 12 (3) (2019) 1433–1440.
- [367] S. Rajper, A. Ahmed, S. Moorat, Automatic Diagnosis of Diabetic Retinopathy Using Morphological Operations, *Intl. J. Sci.* 48 (3) (2019) 213–223.
- [368] R.T. Mamilla, V.K.R. Ede, P.R. Bhima, Extraction of microaneurysms and hemorrhages from digital retinal images, *J. Med. Biol. Eng.* 37 (3) (2017) 395–408.
- [369] G. Quellec, K. Charrière, Y. Boudi, B. Cochener, M. Lamard, Deep image mining for diabetic retinopathy screening, *Med. Image Anal.* 39 (2017) 178–193.
- [370] D. Xiao, S. Yu, J. Vignarajan, D. An, M.L. Tay-Kearney, Y. Kanagasingam, Retinal hemorrhage detection by rule-based and machine learning approach, in: Proc. of the Annual Intl. Conf. of the IEEE EMBS, 2017, pp. 660–663.

- [371] W.M. Gondal, M.K. Jan, Weakly-Supervised Localization of Diabetic Retinopathy Lesions in Retinal Fundus Images, Tech. Rep., Dept. of Comp. Sci., TU Dortmund University, Germany, 2017, pp. 2069–2073.
- [372] N.G. Kurale, M.V. Vaidya, Retinal Hemorrhage Detection Using Splat Segmentation of Retinal Fundus Images, in: Proc. of Intl. Conf. on CUBEIA, IEEE, 2018, pp. 1–6.
- [373] L.G. Atlas, K. Parasuraman, Detection of retinal hemorrhage in fundus images using ANFIS classification and FCM with cuckoo search optimization algorithm, in: Proc. of Intl. Conf. on Commu. and Electron. Syst., IEEE, 2017, pp. 35–39.
- [374] J.L. Orlando, E. Prokofyeva, M. del Fresno, M.B. Blaschko, An ensemble deep learning based approach for red lesion detection in fundus images, Comput. Methods Progr. Biomed. 153 (2018) 115–127.
- [375] S. Khalid, M.U. Akram, T. Khalil, Hybrid textural feature set based automated diagnosis system for Age Related Macular Degeneration using fundus images, in: Proc. of Intl. Conf. on C-CODE, IEEE, 2017, pp. 390–395.
- [376] M. Mokhtari, Z.G. Kamasi, H. Rabbani, Automatic detection of hyperreflective foci in optical coherence tomography b-scans using morphological component analysis, in: Proc. of Annual Intl. Conf. of EMBC, IEEE, 2017, pp. 1497–1500.
- [377] R.S. Rekhi, A. Issac, M.K. Dutta, Automated detection and grading of diabetic macular edema from digital colour fundus images, in: Proc. of UPCON, IEEE, 2017, pp. 482–486.
- [378] A. Rashno, D.D. Koozekanani, P.M. Drayna, B. Nazari, S. Sadri, H. Rabbani, K.K. Parhi, Fully automated segmentation of fluid/cyst regions in optical coherence tomography images with diabetic macular edema using neutrosophic sets and graph algorithms, IEEE Trans. Biomed. Eng. 65 (5) (2017) 989–1001.
- [379] B. Hassan, R. Ahmed, B. Li, Automated foveal detection in OCT scans, in: Proc. of Intl. Symposium on Signal Process. and Inf. Technol., IEEE, 2018, pp. 419–422.
- [380] B. Hassan, R. Ahmed, B. Li, O. Hassan, T. Hassan, Automated retinal edema detection from fundus and optical coherence tomography scans, in: Proc. of Intl. Conf. on Control, Automation and Robotics, IEEE, 2019, pp. 325–330.
- [381] I.P. Okuwobi, Z. Ji, W. Fan, S. Yuan, L. Bekalo, Q. Chen, Automated quantification of hyperreflective foci in SD-OCT with diabetic retinopathy, J. Biomed. Health Inform. 24 (4) (2019) 1125–1136.
- [382] R. Rasti, A. Mehridehnavi, H. Rabbani, F. Hajizadeh, Wavelet-based Convolutional Mixture of Experts model: An application to automatic diagnosis of abnormal macula in retinal optical coherence tomography images, in: Proc. of Iranian Conf. on Mach. Vision and Image Process., IEEE, 2017, pp. 192–196.
- [383] S.C. Athira, R.M. Roy, R.P. Aneesh, Computerized Detection of Macular Edema Using OCT Images Based on Fractal Texture Analysis, in: Proc. of Intl. CET Conf. on Control, Commu., and Comput., IEEE, 2018, pp. 326–330.
- [384] G.C. Chan, S.A. Shah, T. Tang, C.-K. Lu, H. Muller, F. Meriaudeau, Deep features and data reduction for classification of SD-OCT images: Application to diabetic macular edema, in: Proc. of Intl. Conf. on Intell. and Advan. Syst., IEEE, 2018, pp. 1–4.
- [385] K. Alsaih, T. Tang, F. Meriaudeau, G. Lemaitre, M. Rastgoo, D. Sidibe, Classification of Retinal Cysts on SD-OCT Images Using Stacked Auto-Encoder, in: Proc. of Intl. Conf. on Intell. and Advan. Syst., 2018.
- [386] S. Naz, T. Hassan, M.U. Akram, S.A. Khan, A practical approach to OCT based classification of Diabetic Macular Edema, in: Proc. of ICSigSys, 2017, pp. 217–220.
- [387] W.-D. Vogl, S.M. Waldstein, B.S. Gerendas, U. Schmidt-Erfurth, G. Langs, Predicting macular edema recurrence from spatio-temporal signatures in optical coherence tomography images, IEEE Trans. Med. Imaging 36 (9) (2017) 1773–1783.
- [388] A.W. Arif, A. Nasim, A.M. Syed, T. Hassan, Automated Diagnosis of Retinal Edema from Optical Coherence Tomography Images, in: Proc. of Intl. Conf. on CSCI, IEEE, 2018, pp. 554–557.
- [389] F. Ren, P. Cao, D. Zhao, C. Wan, Diabetic macular edema grading in retinal images using vector quantization and semi-supervised learning, Technol. and Health Care 26 (S1) (2018) 389–397.
- [390] T. Hassan, M.U. Akram, A. Shaukat, S. Gul Khawaja, B. Hassan, Structure tensor graph searches based fully automated grading and 3D profiling of maculopathy from retinal OCT images, IEEE Access 6 (2018) 44644–44658.
- [391] A.M. Syed, M.U. Akram, T. Akram, M. Muzammal, S. Khalid, M.A. Khan, Fundus images-based detection and grading of macular edema using robust macula localization, IEEE Access 6 (2018) 58784–58793.
- [392] X. Liu, T. Fu, Z. Pan, D. Liu, W. Hu, B. Li, Semi-Supervised Automatic Layer and Fluid Region Segmentation of Retinal Optical Coherence Tomography Images Using Adversarial Learning, Proc. ICIP (2018) 2780–2784.
- [393] M. Shaikh, V.A. Kollerathu, G. Krishnamurthi, Recurrent attention mechanism networks for enhanced classification of biomedical images, in: Proc. of Intl. Symposium on Biomed. Imaging, IEEE, 2019, pp. 1260–1264.
- [394] B. Hassan, T. Hassan, Fully automated detection, grading and 3D modeling of maculopathy from OCT volumes, in: Proc. of Intl. Conf. on Commu., Comput. and Digital Syst., IEEE, 2019, pp. 252–257.
- [395] L. Huang, X. He, L. Fang, H. Rabbani, X. Chen, Automatic classification of retinal optical coherence tomography images with layer guided convolutional neural network, IEEE Signal Process. Lett. 26 (7) (2019) 1026–1030.
- [396] G. Girish, B. Saikumar, S. Roychowdhury, A.R. Kothari, J. Rajan, Depthwise separable convolutional neural network model for intra-retinal cyst segmentation, in: Proc. of Annual Intl. Conf. of Eng. in Medicine and Biology Society, IEEE, 2019, pp. 2027–2031.
- [397] B. Harangi, J. Toth, A. Baran, A. Hajdu, Automatic screening of fundus images using a combination of convolutional neural network and hand-crafted features, in: Proc. of the Annual Intl. Conf. of EMBS, IEEE, 2019, pp. 2699–2702.
- [398] P.L. Vidal, J. De Moura, J. Novo, M. Ortega, Cystoid Fluid Color Map Generation in Optical Coherence Tomography Images Using a Densely Connected Convolutional Neural Network, in: Proc. of the Intl. Joint Conf. on Neural Networks, IEEE, 2019, pp. 1–8.
- [399] J.M.P. Dias, C.M. Oliveira, L.A. da Silva Cruz, Detection of laser marks in retinal images, in: Proc. of the Intl. Symposium on Computer-Based Med. Syst., IEEE, 2013, pp. 532–533.
- [400] A.M. Syed, M.U. Akbar, M.U. Akram, J. Fatima, Automated laser mark segmentation from colored retinal images, in: Proc. of IEEE INMIC, 2014, pp. 282–286.
- [401] F. Tahir, M.U. Akram, M. Abbass, A.A. Khan, Laser marks detection from fundus images, in: Proc. of Intl. Conf. on HIS, 2003, pp. 147–151.
- [402] J.G. Almeida Sousa, C.M. Oliveira, L.A. Da Silva Cruz, Automatic detection of laser marks in retinal digital fundus images, in: Proc. of European Signal Process. Conf., 2016, pp. 1313–1317.
- [403] O.M. Elrajubi, M.A. Abuzaraida, A.M. Zeki, Retinal image laser marks detection using a convolutional neural network, in: Proc. of Intl. Conf. on 3ICT, IEEE, 2018, pp. 1–5.
- [404] Q. Wei, X. Li, H. Wang, D. Ding, W. Yu, Y. Chen, Laser Scar Detection in Fundus Images Using Convolutional Neural Networks, Springer Int'l. Publishing, 2019, pp. 191–206.
- [405] R. Raut, V. Sapate, A. Rokde, S. Pachade, P. Porwal, M. Kokare, Laser scar classification in retinal fundus images using wavelet transform and local variance, in: Computer Vision and Mach. Intell. in Med. Image Anal., Springer, 2020, pp. 81–90.
- [406] A. Bhuiyan, R. Kawasaki, E. Lamoureux, K. Ramamohanarao, T.Y. Wong, Retinal artery-vein caliber grading using color fundus imaging, Comput. Methods Prog. Biomed. 111 (1) (2013) 104–114.
- [407] U.T. Nguyen, A. Bhuiyan, L.A. Park, R. Kawasaki, T.Y. Wong, J.J. Wang, P. Mitchell, K. Ramamohanarao, Automated quantification of retinal arteriovenous nicking from colour fundus images, in: Proc. of the Annual Intl. Conf. of the IEEE EMBS, 2013, pp. 5865–5868.
- [408] B. Dashtbozorg, A.M. Mendonça, A. Campilho, An automatic graph-based approach for artery/vein classification in retinal images, IEEE Trans. Image Process. 23 (3) (2013) 1073–1083.
- [409] P.K. Roy, U.T. Nguyen, A. Bhuiyan, K. Ramamohanarao, An effective automated system for grading severity of retinal arteriovenous nicking in colour retinal images, in: Proc. of Annual Intl. Conf. of the IEEE EMBC, 2014, pp. 6324–6327.
- [410] J. Kang, Z. Ma, H. Li, L. Xu, L. Zhang, Automatic detection of arteriovenous nicking in retinal images, in: Proc. of Conf. on Industrial Electron. and Appl., 2016, pp. 795–800.
- [411] Artery/vein classification using reflection features in retina fundus images, Mach. Vis. Appl. 29 (1) (2018) 23–34.
- [412] R. Estrada, M.J. Allingham, P.S. Mettu, S.W. Cousins, C. Tomasi, S. Farsiu, Retinal Artery-Vein Classification via Topology Estimation, IEEE Trans. Med. Imaging 34 (12) (2015) 2518–2534.
- [413] Q. Hu, M.D. Abràmoff, M.K. Garvin, Automated construction of arterial and venous trees in retinal images, J. Med. Imaging 2 (4) (2015) 044001.
- [414] A. Mitra, S. Roy, S. Roy, S.K. Setua, Enhancement and restoration of non-uniform illuminated fundus image of retina obtained through thin layer of cataract, Comput. Methods Progr. Biomed. 156 (2018) 169–178.
- [415] Y. Zhao, J. Xie, P. Su, Y. Zheng, Y. Liu, J. Cheng, J. Liu, Retinal artery and vein classification via dominant sets clustering-based vascular topology estimation, in: Proc. of Intl. Conf. on Med. Image Comput. and Computer-Assisted Intervention, Springer, 2018, pp. 56–64.
- [416] H. Kriplani, M. Patel, S. Roy, Prediction of arteriovenous nicking for hypertensive retinopathy using deep learning, in: Computat. Intell. in Data Mining, Springer, 2020, pp. 141–149.

- [417] Á.S. Hervella, J. Rouco, J. Novo, M.G. Penedo, M. Ortega, Deep multi-instance heatmap regression for the detection of retinal vessel crossings and bifurcations in eye fundus images, *Comput. Methods Progr. Biomed.* 186 (2020) 105201.
- [418] H. Zhao, Y. Sun, H. Li, Retinal vascular junction detection and classification via deep neural networks, *Comput. Methods Progr. Biomed.* 183 (2020) 105096.
- [419] C. Pereira, D. Veiga, L. Gonçalves, M. Ferreira, Automatic arteriovenous nicking identification by color fundus images analysis, in: Proc. of Intl. Conf. Image Anal. and Recog., Springer, 2014, pp. 321–328.
- [420] K.-K. Maninis, J. Pont-Tuset, P. Arbeláez, L. Van Gool, Deep retinal image understanding, in: Proc. of Intl. Conf. on Med. Image Comput. and Comput.-Assisted Intervention, Springer, 2016, pp. 140–148.
- [421] T. Laibacher, T. Weyde, S. Jalali, M2u-net: Effective and efficient retinal vessel segmentation for real-world applications, in: Proc. of the IEEE/CVF Conf. on CVPR Workshops, 2019.
- [422] R. Hemelings, B. Elen, I. Stalmans, K. Van Keer, P. De Boever, M.B. Blaschko, Artery-vein segmentation in fundus images using a fully convolutional network, *Comput. Med. Imaging Graph.* 76 (2019) 101636.
- [423] P. Liskowski, K. Krawiec, Segmenting retinal blood vessels with deep neural networks, *IEEE Trans. Med. Imaging* 35 (11) (2016) 2369–2380.
- [424] S.Y. Shin, S. Lee, I.D. Yun, K.M. Lee, Deep vessel segmentation by learning graphical connectivity, *Med. Image Anal.* 58 (2019) 101556.
- [425] L. Mou, L. Chen, J. Cheng, Z. Gu, Y. Zhao, J. Liu, Dense dilated network with probability regularized walk for vessel detection, *IEEE Trans. Med. Imag.* 39 (5) (2019) 1392–1403.
- [426] A. Galdran, A. Anjos, J. Dolz, H. Chakor, H. Lombaert, I.B. Ayed, The little W-net that could: state-of-the-art retinal vessel segmentation with minimalist models, 2020, arXiv preprint [arXiv:2009.01907](https://arxiv.org/abs/2009.01907).
- [427] Q. Li, B. Feng, L. Xie, P. Liang, H. Zhang, T. Wang, A cross-modality learning approach for vessel segmentation in retinal images, *IEEE Trans. Med. Imaging* 35 (1) (2015) 109–118.
- [428] J. Mo, L. Zhang, Multi-level deep supervised networks for retinal vessel segmentation, *Intl. J. Comput. Assist. Radiol. Surg.* 12 (12) (2017) 2181–2193.
- [429] İ. Atli, O.S. Gedik, Sime-Net: A fully convolutional deep learning architecture for retinal blood vessel segmentation, *Intl. J. Eng. Sci. Technol.* (2020).
- [430] J.I. Orlando, E. Prokofyeva, M.B. Blaschko, A discriminatively trained fully connected conditional random field model for blood vessel segmentation in fundus images, *IEEE Trans. Biomed. Eng.* 64 (1) (2016) 16–27.
- [431] O. Ronneberger, P. Fischer, T. Brox, U-net: Convolutional networks for biomedical image segmentation, in: Intl. Conf. on Med. Image Comput. and Comput.-Assisted Intervention, Springer, 2015, pp. 234–241.
- [432] E. Romera, J.M. Alvarez, L.M. Bergasa, R. Arroyo, ERFnet: Efficient residual factorized convnet for real-time semantic segmentation, *IEEE Trans. Intell. Transp. Syst.* 19 (1) (2017) 263–272.
- [433] J. Dai, H. Qi, Y. Xiong, Y. Li, G. Zhang, H. Hu, Y. Wei, Deformable convolutional networks, in: Proc. of Intl. Conf. on Comput. Vision, IEEE, 2017, pp. 764–773.
- [434] D. Adapa, A.N. Joseph Raj, S.N. Alisetti, Z. Zhuang, G. Naik, A supervised blood vessel segmentation technique for digital fundus images using Zernike Moment based features, *PLoS One* 15 (3) (2020) e0229831.
- [435] P.M. Samuel, T. Veeramalai, VSSC net: vessel specific skip chain convolutional network for blood vessel segmentation, *Comput. Methods Progr. Biomed.* 198 (2021) 105769.
- [436] M. Melinscak, P. Prentasic, S. Loncaric, Retinal vessel segmentation using deep neural networks, in: VISAPP (1), 2015, pp. 577–582.
- [437] H. Zhao, H. Li, S. Maurer-Stroh, Y. Guo, Q. Deng, L. Cheng, Supervised segmentation of un-annotated retinal fundus images by synthesis, *IEEE Trans. Med. Imag.* 38 (1) (2018) 46–56.
- [438] V. Badrinarayanan, A. Kendall, R. Cipolla, Segnet: A deep convolutional encoder-decoder architecture for image segmentation, *IEEE Trans. Pattern Anal. Mach. Intell.* 39 (12) (2017) 2481–2495.
- [439] Ü. Budak, Z. Cömert, M. Çibuk, A. Şengür, DCCMED-Net: Densely connected and concatenated multi Encoder-Decoder CNNs for retinal vessel extraction from fundus images, *Med. Hypotheses* 134 (2020) 109426.
- [440] H.A. Leopold, J. Orchard, J.S. Zelek, V. Lakshminarayanan, PixelBNN: Augmenting the PixelCNN with batch normalization and the presentation of a fast architecture for retinal vessel segmentation, *J. Imaging* 5 (2) (2019) 26.
- [441] K.J. Noh, S.J. Park, S. Lee, Scale-space approximated convolutional neural networks for retinal vessel segmentation, *Comput. Methods Progr. Biomed.* 178 (2019) 237–246.
- [442] E. Nasr-Esfahani, N. Karimi, M.H. Jafari, S.M.R. Soroushmehr, S. Samavi, B. Nallamothu, K. Najarian, Segmentation of vessels in angiograms using convolutional neural networks, *Biomed. Signal Process. Control* 40 (2018) 240–251.
- [443] X. Liu, F. Zhang, Z. Hou, L. Mian, Z. Wang, J. Zhang, J. Tang, Self-supervised learning: Generative or contrastive, *IEEE Trans. Knowl. Data Eng.* (2021).
- [444] I. Goodfellow, J. Pouget-Abadie, M. Mirza, B. Xu, D. Warde-Farley, S. Ozair, A. Courville, Y. Bengio, Generative adversarial networks, *Commun. ACM* 63 (11) (2014) 139–144.
- [445] J.-Y. Zhu, T. Park, P. Isola, A.A. Efros, Unpaired image-to-image translation using cycle-consistent adversarial networks, in: Proceedings of the IEEE International Conference on Computer Vision, 2017, pp. 2223–2232.
- [446] T. Karras, S. Laine, T. Aila, A style-based generator architecture for generative adversarial networks, in: Proceedings of the IEEE/CVF Conference on Computer Vision and Pattern Recognition, 2019, pp. 4401–4410.
- [447] A. Van Oord, N. Kalchbrenner, K. Kavukcuoglu, Pixel recurrent neural networks, in: International Conference on Machine Learning, PMLR, 2016, pp. 1747–1756.
- [448] S. Reed, Z. Akata, X. Yan, L. Logeswaran, B. Schiele, H. Lee, Generative adversarial text to image synthesis, in: International Conference on Machine Learning, PMLR, 2016, pp. 1060–1069.
- [449] T. Kim, M. Cha, H. Kim, J.K. Lee, J. Kim, Learning to discover cross-domain relations with generative adversarial networks, in: International Conference on Machine Learning, PMLR, 2017, pp. 1857–1865.
- [450] D. Alexey, P. Fischer, J. Tobias, M.R. Springenberg, T. Brox, Discriminative unsupervised feature learning with exemplar convolutional neural networks, *IEEE Trans. Pattern Anal. Mach. Intell.* 99 (2015).
- [451] M. Caron, I. Misra, J. Mairal, P. Goyal, P. Bojanowski, A. Joulin, Unsupervised learning of visual features by contrasting cluster assignments, *Adv. Neural Inf. Process. Syst.* 33 (2020) 9912–9924.
- [452] K. He, H. Fan, Y. Wu, S. Xie, R. Girshick, Momentum contrast for unsupervised visual representation learning, in: Proceedings of the IEEE/CVF Conference on Computer Vision and Pattern Recognition, 2020, pp. 9729–9738.
- [453] T. Chen, S. Kornblith, M. Norouzi, G. Hinton, A simple framework for contrastive learning of visual representations, in: International Conference on Machine Learning, PMLR, 2020, pp. 1597–1607.
- [454] J. Deng, W. Dong, R. Socher, L.-J. Li, K. Li, L. Fei-Fei, Imagenet: A large-scale hierarchical image database, in: 2009 IEEE Conference on Computer Vision and Pattern Recognition, IEEE, 2009, pp. 248–255.
- [455] I. Misra, L.v.d. Maaten, Self-supervised learning of pretext-invariant representations, in: Proceedings of the IEEE/CVF Conference on Computer Vision and Pattern Recognition, 2020, pp. 6707–6717.
- [456] T.H. Trinh, M.-T. Luong, Q. Le, et al., Self-supervised pretraining for image embedding, 2019, arXiv preprint [arXiv:1906.02940](https://arxiv.org/abs/1906.02940).
- [457] Y. Tian, C. Sun, B. Poole, D. Krishnan, C. Schmid, P. Isola, What makes for good views for contrastive learning? *Adv. Neural Inf. Process. Syst.* 33 (2020) 6827–6839.
- [458] A. Kendall, Y. Gal, What uncertainties do we need in bayesian deep learning for computer vision? *Adv. Neural Inf. Process. Syst.* 30 (2017).
- [459] R. Tomsett, A. Preece, D. Braines, F. Cerutti, S. Chakraborty, M. Srivastava, G. Pearson, L. Kaplan, Rapid trust calibration through interpretable and uncertainty-aware AI, *Patterns* 1 (4) (2020) 100049.
- [460] Y. Gal, Z. Ghahramani, Dropout as a bayesian approximation: Representing model uncertainty in deep learning, in: International Conference on Machine Learning, PMLR, 2016, pp. 1050–1059.
- [461] C. Leibig, V. Allken, M.S. Ayhan, P. Berens, S. Wahl, Leveraging uncertainty information from deep neural networks for disease detection, *Sci. Rep.* 7 (1) (2017) 1–14.



Shahzaib Iqbal received his MS degree in electrical engineering from Abasyn University Peshawar, Pakistan, in 2016. He is currently pursuing Ph.D. degree from COMSATS University Islamabad, Pakistan. He is also working as a Lecturer in Electrical Engineering department, Abasyn University Islamabad Campus. He has more than six years of experience in computer vision and machine learning as a researcher. His research interests includes Medical Image Analysis, Image Segmentation, Deep Neural Networks, and Machine Learning. His current research focuses on the development of lightweight deep neural networks for automated analysis of medical images.



Tariq M. Khan received his Ph.D. degree in electronic engineering from Macquarie University Sydney, Australia, in 2017. He is currently a Senior Research Associate in Computer Vision at the School of Computer Science and Engineering, UNSW. He served as a Research Fellow in Machine Learning at the School of Information Technology, Deakin University. He has more than ten years of experience in computer vision and machine learning as a researcher. His research falls under the broad area of Computer Vision and Machine Learning, including: Image Segmentation, Image Classification, Medical Image Analysis, Resource Constraint Neural Networks, and Deep Neural Networks. His current research focuses on the development of innovative computer vision and machine learning (in particular deep learning) methods for automated quantitative analysis of biomedical imaging data, and other industrial applications.



Khuram Naveed received his PhD degree from Electrical and Computer Engineering Department, COMSATS University Islamabad (CUI), Islamabad, Pakistan, in 2020. He is currently working as a Post-doctoral Researcher at Hydro-Geophysics Group (HGG) that simultaneously operates at the Departments of Geoscience and Electrical and Computer Engineering, Aarhus University Denmark. He is also a permanent faculty (Assistant Professor) at CUI, Islamabad Pakistan. His research explores the use of time-frequency (multiscale and multi-component) decomposition and deep learning methods for signal and image processing with application in denoising, medical diagnosis, machine fault diagnosis and groundwater research.



Syed S. Naqvi received the B.Sc. degree in computer engineering from the COMSATS Institute of Information Technology, Islamabad, Pakistan, in 2005, the M.Sc. degree in electronic engineering from The University of Sheffield, U.K., in 2007, and the Ph.D. degree from the School of Engineering and Computer Science, Victoria University of Wellington, New Zealand, in 2016. He is currently working as an Assistant Professor with the COMSATS Institute of Information Technology. His research interests include saliency modeling, medical image analysis, scene understanding, and deep learning methods for image analysis.



Syed Junaid Nawaz received the Ph.D. degree in electronic engineering from Mohammad Ali Jinnah University, Islamabad, in February 2012. Since September 2005, he has worked on several research and teaching positions with COMSATS University Islamabad (CUI), Pakistan; Staffordshire University, UK; Federal Urdu University, Pakistan; The University of York, UK; and Aristotle University of Thessaloniki, Greece. He is currently working as an Associate Professor with the Department of Electrical and Computer Engineering, COMSATS University Islamabad (CUI), Islamabad, Pakistan. His current research interests include physical channel modeling, channel estimation and characterization, mMIMO systems, adaptive signal processing, machine learning, medical image processing, compressed sensing, mmWave channels, internet-of-things, physical layer security, and localization.